CWhatUC : Software Tools for Predicting, Visualizing and Simulating Corneal Visual Acuity

by

Daniel Dante Garcia

B.S. E.E. (Massachusetts Institute of Technology) 1990
B.S. C.S. (Massachusetts Institute of Technology) 1990
M.S. (University of California, Berkeley) 1995

A dissertation submitted in partial satisfaction of the
requirements for the degree of
Doctor of Philosophy

in

Computer Science

in the

GRADUATE DIVISION
of the
UNIVERSITY of CALIFORNIA at BERKELEY

Committee in charge:

Professor Brian A. Barsky, Chair
Professor Stanley A. Klein
Professor Lawrence W. Stark

2000

The dissertation of Daniel Dante Garcia is approved:

Chair Date

Date

Date

University of California at Berkeley

2000

CWhatUC : Software Tools for Predicting, Visualizing and Simulating Corneal Visual Acuity

Daniel Dante Garcia

Abstract

CWhatUC : Software Tools for Predicting, Visualizing and Simulating Corneal Visual Acuity

by

Daniel Dante Garcia

Doctor of Philosophy in Computer Science

University of California at Berkeley

Professor Brian A. Barsky, Chair

The cornea is the transparent tissue covering the front of the eye, and performs about two-thirds of the refraction, or bending of light into the eye. Thus, subtle variations in its shape significantly affect a patient's visual acuity. Clinicians need to know the shape and refractive contribution of the cornea for several reasons: corneal refractive surgery, contact lens fitting and diagnosis of eye conditions. Instruments that measure the cornea's topography are called *corneal topographers* (CTs), and they have recently become a quite common tool for clinicians. These devices typically shine rings of light onto the cornea and capture the reflection pattern with a video camera. The raw data is extracted from the CT and a spline surface representation is constructed from these reflection patterns. All of our visualization and analysis is performed on these corneal surface representations.

In this work, we present **CWhatUC**, a set of software tools for the prediction,

visualization and simulation of corneal visual acuity.

Prediction We present a new method of representing visual acuity by measuring the *wavefront aberration*, using principles from both ray and wave optics. We measured the topographies and vision of 62 eyes of patients who had undergone the corneal refractive surgery procedures of photorefractive keratectomy (PRK) and photorefractive astigmatic keratectomy (PARK). We found our metric for visual acuity to be better than all other metrics at predicting the acuity of low contrast and low luminance. However, high contrast visual acuity was poorly predicted by all the indices we studied, including our own.

Visualization Our proposed scientific visualizations can be clustered into two classes: *corneal* representations and *retinal* representations. Corneal representations are meant to reveal how well the cornea focuses parallel light onto the fovea of the eye by providing a pseudo-colored display of various error metrics. Retinal representations simulate how parallel incoming rays of light fall onto the retina, revealing aberrations and glare to the clinician.

We generated analytical models of common corneal shapes (with and without degenerative corneal conditions) and gathered a representative set of corneas from patients. We then rendered and analyzed all our visualizations against all of the corneas to illustrate how each representation contributes to the understanding of visual acuity.

Simulation By measuring the light distribution of the cornea to a single point source of light, we capture the "impulse response" (in circuit terms) of the patient's visual system. We then convolve this with a scene to derive a very good first approximation

of what the patient actually sees. We show demonstrations on a standard eye chart as well as a typical outdoor scene.

Only in recent years has the accurate reconstruction of the corneal shape been possible. With over half a million Americans a year choosing to undergo elective laser refractive eye surgery, the availability of accurate and revealing visualizations of corneal shape and acuity is crucial. **CWhatUC** represents a significant contribution to the tools available to clinicians, and to the emerging collaborative fields of computer graphics and vision science.

Professor Brian A. Barsky
Dissertation Committee Chair

Dedication

To Pops, Mom, George, Abuela and Tao.

Contents

List of Figures viii

List of Tables xvii

1 Introduction 1
- 1.1 The Cornea . . . 1
- 1.2 Measurement and Modeling . . . 2
- 1.3 Corneal Shape Visualization . . . 4
- 1.4 Corneal Acuity Visualization . . . 5
- 1.5 Overview . . . 6

2 Background 7
- 2.1 Corneal Shape Visualization . . . 7
  - 2.1.1 Anatomy of the Eye . . . 7
  - 2.1.2 Curvature . . . 11
  - 2.1.3 Axial and Instantaneous Curvature . . . 12
  - 2.1.4 Minimum and Maximum Curvature . . . 14
  - 2.1.5 Gaussian Curvature with a Cylinder Overlay . . . 15
  - 2.1.6 Related Work . . . 17
- 2.2 Geometric and Wave Optics . . . 18
  - 2.2.1 Reflection and Refraction . . . 18
  - 2.2.2 Apertures and Diffraction . . . 21
  - 2.2.3 Light Waves . . . 22
  - 2.2.4 Coddington's Equations . . . 26
- 2.3 Aberrations . . . 26
  - 2.3.1 Spherical Aberration . . . 28
  - 2.3.2 Astigmatism . . . 29
- 2.4 Corneal Acuity Visualization . . . 32
  - 2.4.1 Eye Classifications . . . 32
  - 2.4.2 Corrections . . . 35
  - 2.4.3 Related Work . . . 40

3 Corneas **43**
3.1 Schematic Eye Model . . . 44
3.2 Basic Corneal Models . . . 46
3.2.1 Sphere . . . 47
3.2.2 Ellipsoid Model of "Normal Eye" . . . 48
3.2.3 Ellipsoid Model of Astigmatism . . . 48
3.2.4 Perfect Ellipsoid . . . 49
3.3 Models of "Problem" Corneas . . . 56
3.3.1 PRK . . . 56
3.3.2 Keratoconus . . . 62
3.3.3 Monocular Diplopia . . . 63
3.4 Real Corneal Data . . . 64
3.4.1 "Normal" Cornea . . . 65
3.4.2 Astigmatism . . . 65
3.4.3 PRK . . . 65
3.4.4 Keratoconus . . . 66
3.4.5 Monocular Diplopia . . . 66

4 Visual Acuity Prediction **67**
4.1 Introduction . . . 67
4.2 Methods . . . 68
4.2.1 Measurements from Post-PRK and Post-PARK Eyes . . . 69
4.2.2 Wavefront Coherence Area . . . 69
4.2.3 OPL Refractive Cylinder Correction . . . 72
4.2.4 Other Visual Acuity Metrics . . . 73
4.3 Results . . . 74
4.3.1 Analysis of the Data Fit . . . 74
4.4 Conclusion . . . 78

5 Corneal Representations of Refractive Power **79**
5.1 Introduction . . . 79
5.2 Methods . . . 80
5.2.1 Paraxial Focus vs. "Best" Focus . . . 82
5.2.2 Axial Refractive Power . . . 82
5.2.3 Instantaneous Mean Refractive Power . . . 84
5.2.4 Retinal Distance . . . 85
5.2.5 Focusing Distance . . . 86
5.2.6 Wavefront Representations . . . 87
5.3 Results . . . 91
5.3.1 Simulated Data . . . 91
5.3.2 Real Data . . . 92
5.4 Conclusion . . . 93

6 Retinal Representations of Refractive Power **95**
6.1 Introduction . . . 95
6.2 Methods . . . 96
6.2.1 Point Spread Function . . . 96
6.2.2 Modulation Transfer Function . . . 107
6.2.3 Corneal PSF . . . 107
6.3 Results . . . 108
6.3.1 Effect of Pupil Size . . . 108
6.3.2 Monocular Diplopia . . . 114
6.4 Conclusion . . . 115

7 See What You See : Simulating Corneal Visual Acuity **118**
7.1 Introduction . . . 118
7.2 Methods . . . 119
7.2.1 Normalized Point Spread Function . . . 120
7.2.2 Image Calibration . . . 120
7.2.3 Measuring Visual Acuity . . . 124
7.2.4 Convolution . . . 127
7.3 Results . . . 128
7.3.1 Snellen Eye Chart . . . 129
7.3.2 Outdoor Scene . . . 129
7.4 Conclusion . . . 129

8 Visualizations **131**
8.1 Color Reproduction . . . 133
8.2 Colormaps . . . 133
8.3 Shape Representations . . . 134
8.4 Corneal Representations of Refractive Power . . . 140
8.4.1 Refractive Power . . . 140
8.4.2 Wavefront Angle and Height . . . 143
8.4.3 Wavefront Curvatures . . . 146
8.5 Retinal Representations of Refractive Power . . . 149
8.5.1 2 mm Pupil . . . 151
8.5.2 4 mm Pupil . . . 153
8.5.3 8 mm Pupil . . . 153
8.6 Eye Chart Simulation . . . 159
8.6.1 2 mm Pupil . . . 159
8.6.2 4 mm Pupil . . . 161
8.6.3 8 mm Pupil . . . 164
8.7 Outdoor Scene Simulation . . . 168
8.7.1 2 mm Pupil . . . 168
8.7.2 4 mm Pupil . . . 171
8.7.3 8 mm Pupil . . . 171

9 Conclusion **177**
9.1 Prediction 177
9.2 Visualization 178
9.3 Simulation 178
9.4 Future Directions 179
9.5 Summary 180

Bibliography **181**

List of Figures

1.1 A keratoconic patient having his cornea measured by a corneal topographer. 3
1.2 The reflection pattern for the keratoconic cornea from the patient shown in Figure 1.1. Note how the ring patterns are affected by the bulging of the cornea in the lower-left. 3
1.3 A wireframe rendering of a reconstructed mathematical spline surface. . . . 4
1.4 Three images of a patient's cornea using realistic lighting models as in CAD / CAM applications. In this sequence, the cornea is progressively rotated to face forward, and the light source can be seen as a highlight. Although this cornea may seem smooth and "normal", it is in fact keratoconic, with a large region of high curvature in the lower-left. Traditional computer graphics techniques fail to highlight this anomaly. 5

2.1 A side view of the human eye. 8
2.2 The five layers of the cornea. (Reprinted with permission from [80].) 9
2.3 A curve and its osculating circle. The circle centered at C has the same first and second derivatives as the curve at point P. The radius of curvature of the curve at P is R. The curvature of the curve at P is $\frac{1}{R}$. 11
2.4 The meridional plane is depicted in orange. This plane contains the corneal point of interest (shown as a green dot) and the corneal topographer axis (depicted as a red vector). 12
2.5 The axial distance d_{axial} and instantaneous radius r_{inst} are shown defined in the meridional plane. 13
2.6 The yellow cross-sectional plane contains the normal vector at the corneal point of interest (both shown in green). 15
2.7 The planes corresponding to the minimum and maximum curvature directions are shown in blue and red, respectively. 16
2.8 Snell's law governs the angular relationship of refracted rays as they pass from one medium to another, here shown passing from air ($n_{air} = 1.0$) into the more dense cornea ($n_{cornea} = 1.3375$). The path of the reflected ray is governed by the law of reflection, which states that the angle of reflection is equal to the angle of incidence. 19

2.9 The reason for the refraction of light as it enters a denser medium can often be understood by examining the wavefront and the density of light waves. . 20
2.10 Spherical waves emanating from a point source of light. At great distances, these waves approach the shape of plane waves. 23
2.11 Diverging waves pass through our ideal optical system and converge to a point. The approximate shape of the positive lens that performs this process is sketched in grey. 24
2.12 A prism disperses incoming white light into its spectra [105]. 27
2.13 As the wave approaches its target, it may deviate from an ideal spherical wave; this deviation is called the wavefront aberration. It is measured by calculating the difference between the Optical Path Length (OPL) of the principal ray (whose corresponding perfect spherical wavefront is shown in grey) and the OPL for the other rays, at location (x, y). 27
2.14 A side view of optical system O exhibiting spherical aberration for incoming parallel light from a distant object. The peripheral rays converge faster than the paraxial rays. 29
2.15 Two three-dimensional views of an example of the primary aberration *spherical aberration* viewed as the wave aberration $z = W(x, y) = (x^2 + y^2)^2$. A trimetric projection is on the left and a side view on the right. Spherical aberration is a common problem for lenses; peripheral rays converge more quickly than paraxial rays, resulting in a blur. 30
2.16 Three views of optical system O exhibiting *astigmatism* from a distant point source of light. The top image is a side view showing the vertical paraxial rays converging to point A on plane 2. The middle image is a top view showing the horizontal paraxial rays converging to point B on plane 4. The bottom image is a cross-section through the rays, showing how the blur changes shape as we move from planes 1 through 5. We see the blur as a vertically collapsing oval until plane 2, where it degenerates to a small horizontal line. By plane 3 it is almost circular; this is our *circle of least confusion*. Then the horizontal rays finally converge at point B on plane 4 and the result is a vertical blurred line. Past point B the blur remains a tall and thin oval, shown on plane 5. . 30
2.17 Two three-dimensional views of an example of the primary aberration *astigmatism* viewed as the wave aberration $z = W(x, y) = y^2$. A trimetric projection is on the left and a side view on the right. Astigmatism adds an asymmetry to the wavefront, by contributing refractive power in one direction but not the other. This is known as adding a "cylinder" component, which blurs the image point. 32
2.18 A side-view of an emmetropic, myopic and hyperopic schematic eye shown unaccommodated viewing a distant object. Note the retinal blur in the rightmost two ametropic eyes. 33
2.19 Monocular diplopia is a corneal condition in which a single distant point light appears to the patient as two lights. 36
2.20 A cornea with eight RK incisions. (Reprinted with permission from [53]. ©1996-2000, Internet Media Services, Inc. All rights reserved.) 37

2.21 A graphical representation of the PRK process illustrating the ablation of the front surface of the cornea. (Reprinted with permission from [53]. ©1996-2000, Internet Media Services, Inc. All rights reserved.) 38
2.22 A graphical representation of the LASIK process illustrating the ablation of the front surface of the cornea beneath the flap. (Reprinted with permission from [53]. ©1996-2000, Internet Media Services, Inc. All rights reserved.) . 38
2.23 Intacs are clear, crescent-shaped rings as shown on the right. They are inserted into the stromal layers of the cornea to correct mild myopia, shown on the right. (Reprinted with permission from [53]. ©1996-2000, Internet Media Services, Inc. All rights reserved.) 39

3.1 Our schematic model of the eye. 44
3.2 A Cartesian oval. All the rays from S converge at P with equal optical path length [44]. 49
3.3 A perfect ellipsoid, which focuses all plane waves to a point (F_2) with no aberrations [44]. 51
3.4 A 3-D rendering of our PRK model. The white cornea has a central transition zone (in blue) and an ablation zone (in red). 57
3.5 A diagram indicating the constraint propagation that takes place as we create our PRK model. We progressively determine C_a, C_t, r_t, and finally C_b. . . . 58
3.6 A 2-D plot of $z_{PRK}(r)$ through its three helper functions z_a, z_t, and z_b, representing the active surfaces for the ablation zone, transition zone and base corneal zone. The curves are scaled (and, in the case of C_t, de-centered) circles which meet with positional and tangent continuity at the junctions. Our transitions are at $r_{at} = 2.5$ and $r_{tb} = 3$, since we were given $w = 2.5$ and $t = 0.5$. 59
3.7 This graph illustrates the base corneal model without keratoconus. The model is a simple sphere with constant axial power across its surface. This is represented here as a yellow straight line when plotting axial power vs. distance. The power is denoted P_{sphere} and is labeled on the right. 61
3.8 To model keratoconus, a section of the sphere is removed and replaced with a surface of revolution formed from a hyperbola. The axial power associated with the hyperbola between $-t$ and t is shown as the central curve. The maximum power of the cone is denoted P_{cone}. 61
3.9 A 3-D rendering of the position of the cone (shown in green) on the cornea (in white). The cone is centered at ($\phi = 12°$, $\theta = 215°$), P_{sphere} is 45 D (radius 7.5 mm), P_{cone} is 82 D and t is 2 mm. 63

4.1 The crosshatched sampling technique on the left was used to query the geometry information from our reconstructed corneal models. The cornea on the right is shown sampled by this method to form a triangular mesh. . . . 68
4.2 A simple model of a side view of the eye and the technique used for finding the wavefront coherence area. 71
4.3 A simple model of the front view of the cornea highlighting the method used to calculate the cylinder distance. 72

4.4 Scatter plots of CA, CVP, SAI and SRI versus the three actual acuity indices, SLCT-L, SLCT-D and HCVA. 75
4.5 Comparison of correlation R^2 values for the four visual acuity predictors. . 76
4.6 Predictor SAI versus measured low contrast SLCT-L before and after removing the two circled poor performing eyes. 77
4.7 The correlation comparison after removing two patients' corneas from the sample. 77

5.1 A simple model of the cornea, eye, and the refraction of a ray of incoming light. 81
5.2 Axial refractive power is a function of the distance between the corneal point and the axis intersection. 83
5.3 A comparison between axial refractive power and axial curvature. 84
5.4 Instantaneous mean refractive power is a function of the distance between the corneal point and the focus. 85
5.5 Retinal distance is the distance between the retinal intersection and the PFP. 86
5.6 Focusing distance is the distance between the focus and the PFP. 87
5.7 We begin our wavefront calculation at our best focus (which may be distinct from the PFP), then send out rays of light to the cornea, and refract them into air. They may not all be parallel. 88
5.8 We calculate the position of the wavefront by first determining the reference optical path length (OPL_{ref}). This is the sum of the time spent in the cornea, the time spent in air until it hits the entrance pupil at $z = 3$ mm, and a phase term to account for our cylinder correction. For a particular point P on the cornea, we follow the ray for the same time as the reference ray. This involves tracing the ray to the cornea, refracting it into air, and following that refracted ray until our "time" equals that of the reference ray. This means we follow the normal backwards as shown by the dotted line, until we hit our wavefront point. 89
5.9 A three-dimensional view of our simulated cornea, modeled as an ellipsoid with $A = 8.7$, $B = 9$ and $C = 10$. 92
5.10 Figure 10: A view of our four acuity metrics for ellipsoidal simulated data. . 93
5.11 A view of our four acuity metrics for the real data of a keratoconic cornea. 94

6.1 Light from a point source is refracted to form the PSF. 97
6.2 A height field representation of a sample $\overline{\mathrm{PSF}}$. 98
6.3 The crosshatched sampling pattern used to sample the cornea. Rays from the infinite light source pass through these samples and are refracted into the eye. 99
6.4 A refracted ray lands in one of the sample buckets on our retinal plane. . . 101

6.5 The distribution of an off-center ray contributes energy into several neighboring samples. This top-down view demonstrates what happens when a ray lands in a sample labeled *SW* at the point ($11\frac{3}{4}$, $5\frac{5}{6}$), shown as a cross. One-fourth of the unit cube (representing the unit ray contribution) is east of the line $X = 12$ and one-third is north of the line $Y = 6$, so the neighbors here receive the appropriate number of $\frac{1}{12}ths$ of the cube corresponding to the overlap. Sample *SW* gets 6, *NW* gets 3, *SE* gets 2, and *NE* gets only 1 of the 12 $\frac{1}{12}ths$ contribution. 101
6.6 The $\overline{\text{PSF}}$ for ideal eye A. All light is focused to the center of sample (2,16) as indicated by the cross, so the entire sample receives all the energy from the rays. The Strehl$_g$ ratio for this eye is one, as it should be. 103
6.7 The $\overline{\text{PSF}}$ for ideal eye B. All light is focused to the intersection of four samples, at the lower-right of sample (2,16) as indicated by the cross, so the four neighboring samples share the energy from the rays. All four receive equal one-quarter energy distributions, and the Strehl$_g$ ratio for this eye is one-quarter. 103
6.8 The $\overline{\text{PSF}}$ of an astigmatic cornea before and after our cylinder correction. . 104
6.9 A matrix of $\overline{\text{PSF}}$s for four different pupil diameters (top to bottom): $\frac{1}{2}$, 1, 2, and 4 mm and four different corneas (left to right): perfect ellipsoid, sphere model, normal cornea and one with monocular diplopia. The x- and y-range is the same for every eye and pupil, -20 μm to 20 μm. We allowed the z-height to be auto-ranging. 109
6.10 A plot of Strehl$_g$ ratio vs. pupil size for four different corneas (from best to worse performing): perfect ellipsoid model, sphere model, the normal eye and the monocular diplopia. Note that this last cornea actually performed better than the normal eye with a $\frac{1}{2}$ mm pupil. 110
6.11 Color $\overline{\text{PSF}}$s from 8 mm pupils for four different corneas (clockwise from top left): perfect ellipsoid model, sphere model, monocular diplopia and the normal eye. 111
6.12 MTF curves for five different pupil diameters (in mm): $\frac{1}{2}$, 1, 2, 4 and 8 and four different corneas (clockwise from top left): perfect ellipsoid model, sphere model, monocular diplopia and the normal eye. We plot all five curves at once on each diagram; the $\frac{1}{2}$ mm pupil curve is always closest to unity, the 1 mm pupil curve right below that, and so on. 113
6.13 The $\overline{\text{PSF}}$ for the monocular diplopic eye with an 8 mm pupil. The primary focus is indicated by the energy peak in the center of the figure. The patient's perceived dual image is caused by the second peak approximately 0.2 mm below the first. This maps to the area of reduced curvature in the upper cornea on the corneal PSF image in Figure 6.14. 114
6.14 The corneal PSF for the monocular diplopic eye with an 8 mm pupil. The primary focus is generated by the central oval region. The patient's perceived dual image is created by the area of reduced curvature in the upper central cornea, which causes the second $\overline{\text{PSF}}$ peak in Figure 6.13. 116

7.1 Simulation of an eye viewing an image exactly as it was seen by the camera. The centers of projection are aligned and the image is scaled so that one pixel on the image maps to one sample on the $\overline{\text{PSF}}$. 121
7.2 Simple geometry controls the relationship between an object's distance (d), its image size (h) and the angle it subtends (θ). That relationship is captured by the expression $h = d \tan \theta$. 122
7.3 Simulation of an eye viewing a projected digitized image from afar. The eye's center of projection is placed at a distance d and the image is scaled so that one pixel on the digital image maps to one sample on the $\overline{\text{PSF}}$. 123
7.4 A typical Snellen letter. 124
7.5 A typical acuity chart with tumbling Es used for acuity assessment of pre-literate children. This chart is especially useful for us since rasterization requires no anti-aliasing as would a chart with curved-edge letters. 126
7.6 The image we use for our acuity simulation. The size of the Es ranges from 20/10 on the left to 20/160 on the right. The fan pattern on the far right is used to test for astigmatism. 126
7.7 The image we use for our outdoor scene simulation, a photograph of U. C. Berkeley's Campanile courtesy of Paul Debevec. 127
7.8 Instead of convolving the $\overline{\text{PSF}}$ with our image (shown in grey), we multiply their Fourier transforms and return the inverse Fourier transformation (shown in black). 128

8.1 Our quantized 8-level "hot" colormap: black → red → yellow → off-white. . 133
8.2 Shape representations for the six regular eyes. From left to right we display axial, instantaneous, minimum, and maximum power and mean sphere, all measured in diopters (D). 135
8.3 Shape representations for the six problem eyes. From left to right we display axial, instantaneous, minimum, and maximum power and mean sphere, all measured in diopters (D). 137
8.4 Corneal paraxial focus refractive power representations for our six regular eyes. From left to right is retinal and focusing distance (measured in mm), axial refractive power and instantaneous mean refractive power (measured in diopters). 139
8.5 Corneal paraxial focus refractive power representations for our six problem eyes. From left to right is retinal and focusing distance (measured in mm), axial refractive power and instantaneous mean refractive power (measured in diopters). 141
8.6 Corneal wavefront angle and height representations for our six regular eyes. The wavefront angle is measured in minutes and the height in microns. . . . 144
8.7 Corneal wavefront angle and height representations for our six problem eyes. The wavefront angle is measured in minutes and the height in microns. . . . 145
8.8 Corneal wavefront curvature representations for the six regular eyes. From left to right we display axial, instantaneous, minimum, and maximum power and mean sphere, all measured in diopters (D). 147

8.9 Corneal wavefront curvature representations for the six problem eyes. From left to right we display axial, instantaneous, minimum, and maximum power and mean sphere, all measured in diopters (D). 148
8.10 Retinal representations for the six regular eyes with a 2 mm pupil. The leftmost display is the corneal PSF in which the color represents mean sphere (measured in diopters) and the contour lines represent the 2, 4 and 8 minute distance to the best focus on the retina. The next two visualizations are a three dimensional and overhead view of the $\overline{\text{PSF}}$. The rightmost two representations are views of the MTF, one a three dimensional view and one a radial average about the center. 150
8.11 Retinal representations for the six problem eyes with a 2 mm pupil. The leftmost display is the corneal PSF in which the color represents mean sphere (measured in diopters) and the contour lines represent the 2, 4 and 8 minute distance to the best focus on the retina. The next two visualizations are a three dimensional and overhead view of the $\overline{\text{PSF}}$. The rightmost two representations are views of the MTF, one a three dimensional view and one a radial average about the center. 152
8.12 Retinal representations for the six regular eyes with a 4 mm pupil. The leftmost display is the corneal PSF in which the color represents mean sphere (measured in diopters) and the contour lines represent the 2, 4 and 8 minute distance to the best focus on the retina. The next two visualizations are a three dimensional and overhead view of the $\overline{\text{PSF}}$. The rightmost two representations are views of the MTF, one a three dimensional view and one a radial average about the center. 154
8.13 Retinal representations for the six problem eyes with a 4 mm pupil. The leftmost display is the corneal PSF in which the color represents mean sphere (measured in diopters) and the contour lines represent the 2, 4 and 8 minute distance to the best focus on the retina. The next two visualizations are a three dimensional and overhead view of the $\overline{\text{PSF}}$. The rightmost two representations are views of the MTF, one a three dimensional view and one a radial average about the center. 155
8.14 Retinal representations for the six regular eyes with an 8 mm pupil. The leftmost display is the corneal PSF in which the color represents mean sphere (measured in diopters) and the contour lines represent the 2, 4 and 8 minute distance to the best focus on the retina. The next two visualizations are a three dimensional and overhead view of the $\overline{\text{PSF}}$. The rightmost two representations are views of the MTF, one a three dimensional view and one a radial average about the center. 156

8.15 Retinal representations for the six problem eyes with an 8 mm pupil. The leftmost display is the corneal PSF in which the color represents mean sphere (measured in diopters) and the contour lines represent the 2, 4 and 8 minute distance to the best focus on the retina. The next two visualizations are a three dimensional and overhead view of the $\overline{\text{PSF}}$. The rightmost two representations are views of the MTF, one a three dimensional view and one a radial average about the center. 158
8.16 Representations of tumbling Es blurred as they would by the regular eyes with a 2 mm pupil. The size of the letters from left to right are: 20/10, 20/20, 20/40, 20/80 and 20/160. We also include a fan test for gauging astigmatism. 160
8.17 Representations of tumbling Es blurred as they would by the problem eyes with a 2 mm pupil. The size of the letters from left to right are: 20/10, 20/20, 20/40, 20/80 and 20/160. We also include a fan test for gauging astigmatism. 162
8.18 Representations of tumbling Es blurred as they would by the regular eyes with a 4 mm pupil. The size of the letters from left to right are: 20/10, 20/20, 20/40, 20/80 and 20/160. We also include a fan test for gauging astigmatism. 163
8.19 Representations of tumbling Es blurred as they would by the problem eyes with a 4 mm pupil. The size of the letters from left to right are: 20/10, 20/20, 20/40, 20/80 and 20/160. We also include a fan test for gauging astigmatism. 165
8.20 Representations of tumbling Es blurred as they would by the regular eyes with an 8 mm pupil. The size of the letters from left to right are: 20/10, 20/20, 20/40, 20/80 and 20/160. We also include a fan test for gauging astigmatism. 166
8.21 Representations of tumbling Es blurred as they would by the problem eyes with an 8 mm pupil. The size of the letters from left to right are: 20/10, 20/20, 20/40, 20/80 and 20/160. We also include a fan test for gauging astigmatism. 167
8.22 A representation of an outdoor scene blurred as it would by the regular eyes with a 2 mm pupil. Photograph of U. C. Berkeley's Campanile courtesy of Paul Debevec. 169
8.23 A representation of an outdoor scene blurred as it would by the problem eyes with a 2 mm pupil. Photograph of U. C. Berkeley's Campanile courtesy of Paul Debevec. 170
8.24 A representation of an outdoor scene blurred as it would by the regular eyes with a 4 mm pupil. Photograph of U. C. Berkeley's Campanile courtesy of Paul Debevec. 172
8.25 A representation of an outdoor scene blurred as it would by the problem eyes with a 4 mm pupil. Photograph of U. C. Berkeley's Campanile courtesy of Paul Debevec. 173
8.26 A representation of an outdoor scene blurred as it would by the regular eyes with an 8 mm pupil. Photograph of U. C. Berkeley's Campanile courtesy of Paul Debevec. 174

8.27 A representation of an outdoor scene blurred as it would by the problem eyes with an 8 mm pupil. Photograph of U. C. Berkeley's Campanile courtesy of Paul Debevec. 175

9.1 When customized LASIK procedures and accurate surgical simulations become commonplace, **CWhatUC++** could be used in a feedback loop to optimize for visual acuity. Patients would have the opportunity to see the predicted corneal shape and overall acuity before they decided to undergo the procedure. 179

List of Tables

6.1 The 2×2 post-processing smoothing filter we apply to the PSF for our optimization. 103

7.1 The relationship between MAR and Snellen notations. 125

8.1 The template for visualizations of the regular corneas. The section in which each cornea is described is listed in parentheses. Viz_i stands for the ith Visualization of the series. The model corneas indicated by * are purely analytic and did not require fitting by our polynomial. 132

8.2 The template for visualizations of the problem corneas. The section in which each cornea is described is listed in parentheses. Viz_i stands for the ith Visualization of the series. The model corneas indicated by * are purely analytic and did not require fitting by our polynomial. Those corneas indicated by † were generated by sampling an analytic shape to derive a high density point cloud, which was then fit by our polynomial. 132

8.3 An alternate template for visualizations with varied sized pupils. This would allow analysis of how pupil size affected acuity, but would sacrifice consistency and would not provide immediate comparison with other corneas in the same classification. 151

Acknowledgements

This dissertation is the final chapter to a long and fulfilling graduate career. There are many people who have helped me along the way; first and foremost is my advisor and mentor, Professor Brian Barsky. I cannot say enough about the positive influence he has had on my development as a researcher and teacher. He recognized the sparkle in my eyes when I put on my instructor hat, and supported my growth throughout. Our six years and thirteen classes teaching together as the "Brian and Dan" team rank among my most fulfilling experiences. We've been through lots of highs (SIGGRAPH 1996, CS39a, CS184, OPTICAL meetings) with very few lows (uh oh, there's the neck thing again), and it's as good a working relationship one could ask for. Thank you, Brian, for the years of support and friendship.

Professor Stanley Klein provided the technical advice at the heart of this thesis. He helped me bridge the knowledge gap between computer graphics and vision science. I fondly recall late night (2 am, when most faculty are sound asleep) email sessions debugging corneal visualizations with him. What fun it was working alongside someone with such youthful vigor who, at the ripe age of sixty, rode in to give a guest lecture in computer graphics on a scooter! Stan is a brilliant and enthusiastic teacher, and is someone from whom I wish I could have learned *all* my physics.

Professor Larry Stark is one of the wisest men I know. What a privilege it has been to work with (and accept advice from) someone with such intellectual breadth and experience. Teaching a class in Virtual Reality with Larry was quite positive and memorable. Professor Robert Mandell was involved with the OPTICAL project in its early stages, and

it was a real honor to work with someone of such renown. I also enjoyed interacting with Professor John Corzine, who provided lots of assistance with TVT data and was always ready to "talk shop" about our Macintoshes.

I would like to thank Corina van de Pol for her continual help along the way, her contribution to my PSF code, and for her sense of humor. She never failed to make me smile; what spirit she has! Jacob Corbin and I became fast friends when we realized how many buddies and interests we had in common. Jacob served as my main Matlab consultant, helping me navigate the TVT world with data, reconstruction and visualization code. He also throws great house-warming parties. Henry Tran was always fun, generous with his time to help fix a downed PC, and has the largest archive of DVDs this side of Blockbuster Video.

The other graduate students in the OPTICAL group were not only my officemates and colleagues, but my friends. My "brother" Zijiang Yang (we were born on the same day and year!) remains very close, even though he is now on the other side of the globe. My OPTICAL officemates Lillian Chu, Alex Berg, Michael Downes, and alumni Jonathan Kung, Roger Kumpf, Mark Halstead and Neha Wickramasekaran are all folks I'm fortunate to have met and with whom I've shared some truly enjoyable years. Don't be strangers when I move up to room 795, y'all, if for no reason other than to visit my chair!

Why did I take 9 $\frac{1}{2}$ years to graduate? I credit my close GTAT friends Dan Rice, Angie Schuett, Drew Roselli and Ajay Sreekanth, my best friends Michael Sheriar, Greg Wolff and Jason Palmer, the game of golf and NBC's Thursday night lineup. They all provided an unbelievably enjoyable world of diversion and memories — why would anyone

leave when they were having so much fun?! A special note goes to Jason for introducing our kitten Baby (who has never met a wall that didn't deserve to be sprayed) into my life. My housemate and friend Ronnen "Father Theresa" Levinson, was different; I can't count how many times he asked how he could help with my thesis. He selflessly dished out advice, support and served as WebVan for me these last few months.

On the family front, my biggest supporter has to be my mom, always ready with a proud "How to go!" and loving voice on the phone. My late father Raymond Garcia and Abuela Mary Turner always made me feel I was their biggest source of pride — truly uplifting. My stepfather George Badgley only had to give me a warm look and place a reassuring hand on my shoulder and I knew how much my success meant to him.

When it all comes down to it, however, I could not have done it without my fiancée Tao. She pushed me when I needed to be pushed (several times), gave me shoulder and arm massages at crucial final stages, fixed my hung Linux box, and assisted me in uncountable ways. I do credit her parents for holding our marriage hostage until I graduated as the straw which broke the proverbial camel's writer's block.

Borrowing a line from Lou Gehrig's famous speech, I consider myself one of the luckiest men alive to have had such a rich graduate school experience and met such wonderful people. Thanks to you all!

Chapter 1

Introduction

> A child of *five* would understand this... Send somebody to fetch a child of five!
> — *Groucho Marx, "Duck Soup"*

1.1 The Cornea

The cornea is the transparent tissue covering the front of the eye, and performs about two-thirds of the refraction, or bending of light into the eye. Subtle variations in its shape significantly affect a patient's visual acuity. Clinicians need to know the shape and refractive contribution of the cornea for several reasons:

Corneal refractive surgery Over 160 million people in the United States alone wear contact lenses or glasses. Of those, almost three-quarters of a million people are expected to undergo elective laser refractive eye surgery in 2000 [36]. It is critical that the clinician understand the shape and refractive properties of the cornea before surgery. It is equally important that he or she has effective tools to evaluate the patient post-surgically, to gauge healing and to make informed decisions as to whether further

"enhancements" are necessary.

Diagnosis of eye conditions Keratoconus in a degenerative eye condition which can deleteriously affect a patient's vision. It results in the bulging and thinning of the cornea [68]; the vision of patients is often rendered uncorrectable due to the shape changes that occur. Although contact lenses offer the potential of visual correction, it is difficult to fit a contact lens to a keratoconic cornea. In addition, these patients need to be screened out as poor candidates for refractive surgery.

Contact lens fitting Eye care practitioners need to know the shape of a patient's cornea to fit contact lenses effectively [81]. The optical and fit properties of the lenses are now set by trial-and-error; having an understanding of corneal shape provides the clinician with a better initial guess. Also, a current area of research is providing fully customized rigid contact lenses with hundreds of parameters individually tailored to a patient's needs. Shape constraints would help to optimize the back surface of the lens for maximum comfort.

1.2 Measurement and Modeling

Instruments that measure the cornea's topography are called *corneal topographers* (CTs) [64, 65, 79, 114, 118]. These devices typically shine rings of light onto the cornea and capture the reflection pattern with a built-in video camera. Figure 1.1 shows a keratoconic patient being measured by a corneal topographer, and Figure 1.2 shows the resulting ring pattern. In practice, the CT then constructs its own internal model of the cornea and allows the clinician to choose from among its custom visualizations for analysis. However, instead

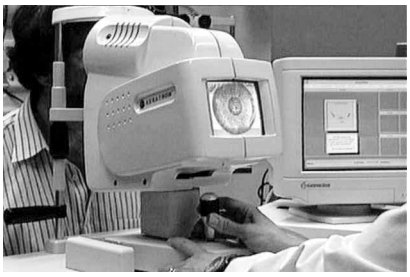

Figure 1.1: A keratoconic patient having his cornea measured by a corneal topographer.

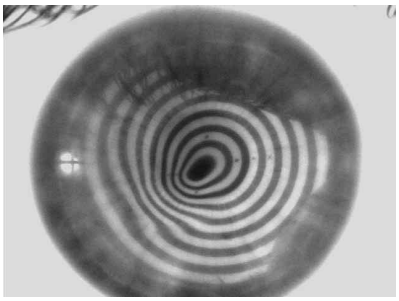

Figure 1.2: The reflection pattern for the keratoconic cornea from the patient shown in Figure 1.1. Note how the ring patterns are affected by the bulging of the cornea in the lower-left.

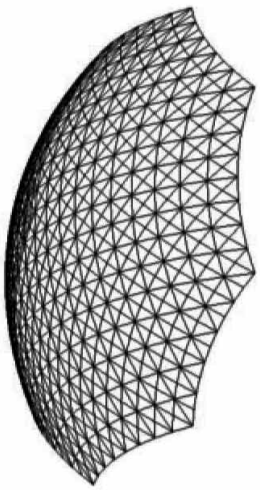

Figure 1.3: A wireframe rendering of a reconstructed mathematical spline surface.

of allowing the CT to process the pattern, the OPTICAL project extracts the data and constructs a spline surface representation from these reflection patterns [20, 41, 42].

The continuous nature of the reconstructed surface allows arbitrary sampling to query position, normals and principal curvatures. These are passed to our visualization algorithms which perform the calculations necessary to image different characteristics. A wireframe rendering of an example surface with a very low sampling density is shown in Figure 1.3.

1.3 Corneal Shape Visualization

Traditional three-dimensional computer graphics (CG) techniques that simulate realistic lighting models work well in CAD / CAM applications but fail for the display of corneal shape because they do not capture important shape subtleties. Figure 1.4 shows how poorly the shape of a patient's cornea is represented using traditional CG techniques.

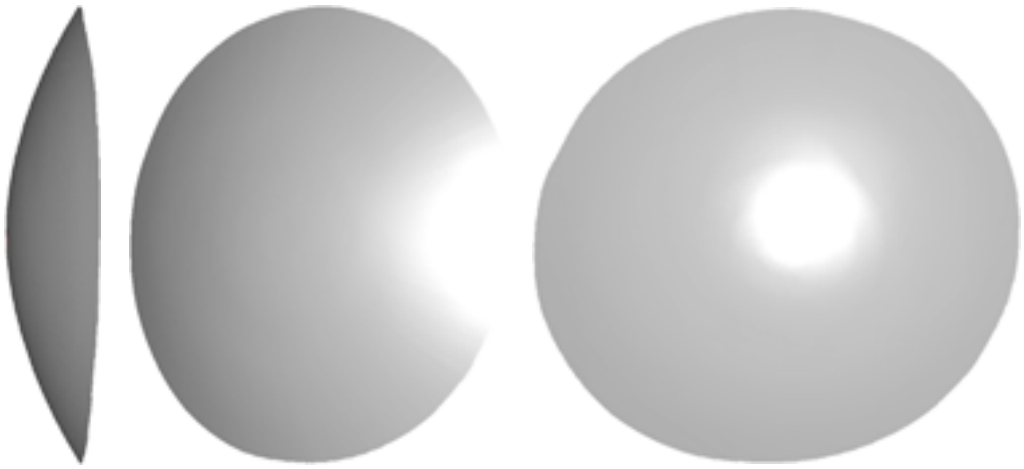

Figure 1.4: Three images of a patient's cornea using realistic lighting models as in CAD / CAM applications. In this sequence, the cornea is progressively rotated to face forward, and the light source can be seen as a highlight. Although this cornea may seem smooth and "normal", it is in fact keratoconic, with a large region of high curvature in the lower-left. Traditional computer graphics techniques fail to highlight this anomaly.

The solution is to pseudo-color the cornea with a revealing calculation based on the subtleties of its shape; this is the essence of corneal topography visualizations. We discuss traditional and more recent techniques in Section 2.1.

1.4 Corneal Acuity Visualization

The "Achilles' heel" of corneal shape visualizations is that they do not answer critical questions about how well (and in what regions) the cornea *focuses light* coherently onto the retina, nor do they provide an approximation of what the patient actually sees. A particular cornea may appear to be a smooth and efficient refracting surface, but in fact may have several aberrations [78] that prevent good vision. To address this, we present **CWhatUC** (pronounced "see what you see"), a collection of software tools for the prediction, visualization and simulation of corneal visual acuity.

1.5 Overview

Chapter 2 provides background information on shape visualization using curvature, highlights traditional and more recent techniques as well as reviewing related work. It also explains the basics of geometric and wave optics, common visual system aberrations, how clinicians correct them, and discusses related work in corneal acuity visualizations. Chapter 3 explains our representation of the cornea used in our calculations, enumerates all of the analytical models, and describes some of the patient data sets we consider. Chapter 4 focuses on (no pun intended) visual acuity prediction, and our attempt to create and evaluate a metric for characterizing the acuity of post-surgical corneas. Chapter 5 explains four corneal representations for visual acuity based on fundamentals of geometric optics. Chapter 6 explains three retinal representations, meant to simulate how parallel incoming rays of light fall onto the fovea, revealing aberrations and glare. Chapter 7 builds on techniques from Chapter 6 and two-dimensional signal processing to simulate what the actual patients would see when looking at different things, such as an eye chart and an outdoor scene. Chapter 8 catalogues and provides analysis of all the visualizations and simulations for all the corneal data, real and analytic. Finally, Chapter 9 summarizes the principal contributions of this dissertation.

Chapter 2

Background

> You never know what is enough unless you know what is more than enough.
> — *William Blake, "The Marriage of Heaven and Hell"*

2.1 Corneal Shape Visualization

In this section we briefly describe the anatomy of the eye and explain the mathematical foundation of *curvature*, a critical building block for much of our research on corneal shape visualization. We also explain traditional methods and more recent techniques, and review related work in corneal shape representations.

2.1.1 Anatomy of the Eye

As our colleague Dr. Mandell (of contact lens theory fame [80]) is oft to point out, the "celestial committee" did a remarkable job when it designed the human eye. Its various structures work in a perfect harmony, with each component fulfilling a needed task. In fact, its optical performance "has almost reached the limit imposed by nature itself" [90].

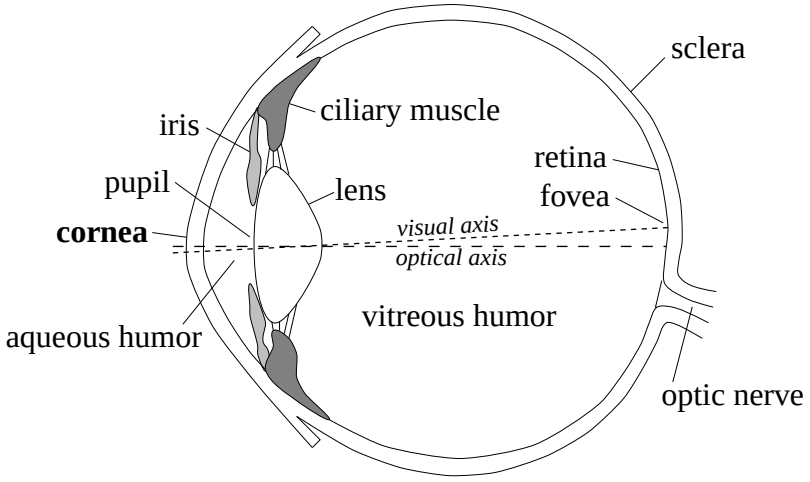

Figure 2.1: A side view of the human eye.

We highlight several of the key elements in this subsection; for more detailed descriptions, see [1], [55], [80], or [90].

Sclera The outermost fibrous layer which completely surrounds the eye (except for the cornea) and maintains its shape.

Cornea The transparent front surface of the eye, serving as its main refractive component, and contributing about two-thirds of the total power. Light enters the inner elements of the eye via the cornea. Its size is approximately 12 mm in diameter, and it is vertically squashed a slight amount. The thickness of the cornea is approximately 0.5 mm at the center. There is a *tear film* on the anterior (front) of the cornea which fills in irregularities and improves the overall optics.

The cornea has five layers as indicated in Figure 2.2: the *epithelium*, *Bowman's membrane*, *stroma*, *Descemet's membrane* and *endothelium*. The stroma composes 90% of the cornea's thickness, and is responsible for its elasticity and strength.

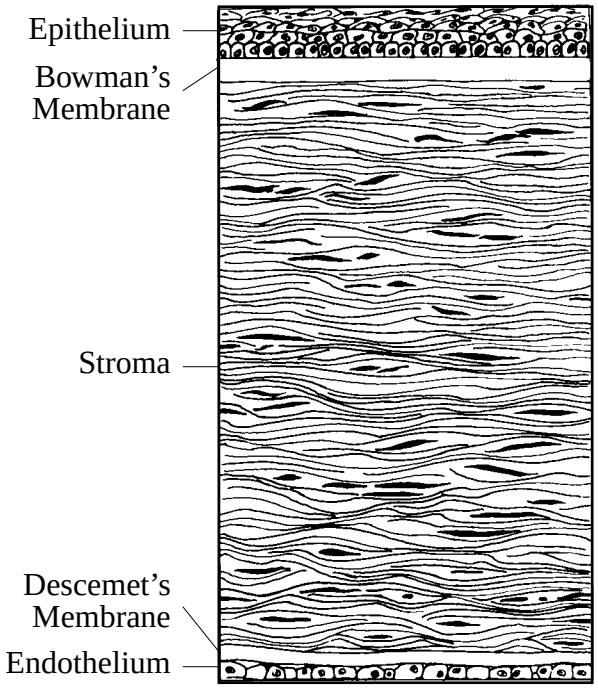

Figure 2.2: The five layers of the cornea. (Reprinted with permission from [80].)

Aqueous Humor A transparent watery liquid which fills the *anterior chamber* behind the cornea and in front of the iris and crystalline lens.

Iris The opaque structure which gives the eye its color, it has a near-circular opening in the center called the pupil. It contains involuntary muscles which react to incoming luminance and regulate the amount of light which enters the eye. Its autonomic ability to constrict and dilate (and thus change the pupil size) serves as an important indicator of patient health for trauma professionals.

Pupil The opening in the iris. Pupil size decreases with age at a roughly uniform rate, slowing in later years. In total darkness, the pupil expands to allow in as much light as possible, which is 7.6 mm at age 10 and dwindles to 3.4 mm by age 80 [90].

Lens A transparent, crystalline, high-protein material which focuses the light onto the back of the eye. Its structure is complex, composed of a radial pattern of fibrous layers which is the source of diffraction halos people see at night. It is surrounded by a ciliary muscle which contracts, changing its shape to better focus incoming light.

Ciliary Muscle The muscle which constricts to modify the shape of the lens — a process known as *accommodation*. As the lens ages, it grows fresh layers on the exterior, much like a tree. As well, it undergoes reduced flexibility and transparency, severely limiting the degree of accommodation.

Vitreous Humor The dark chamber behind the lens filled with a transparent, gelatinous substance.

Retina The image-forming sensitive tissue on the posterior (back) inner surface of the

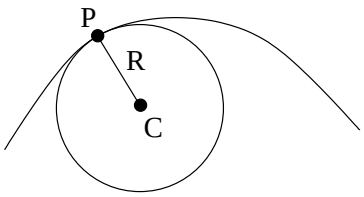

Figure 2.3: A curve and its osculating circle. The circle centered at C has the same first and second derivatives as the curve at point P. The radius of curvature of the curve at P is R. The curvature of the curve at P is $\frac{1}{R}$.

eye. Light-sensitive nerve endings called *rods* and *cones* convert the light energy into neural signals sent to the brain via the *optic nerve*. The central region of the retina is the 1.5 mm diameter *foveal* area, with closely packed cones and few rods. As the distance from the fovea increases, the number of rods increases and the number of cones decreases. The peripheral region of the retina is used more for light and motion detection, whereas the foveal area is used more for form detection, color detection, and resolution of fine detail. The area where the optic nerve connects to the retina contains neither rods nor cones, and thus is a *blind spot*.

2.1.2 Curvature

One traditional technique that reveals subtle changes in shape is to display curvature across the surface. Curvature is a two-dimensional concept which describes how much a curve "bends". It is defined in the following way: the circle that has the same first and second derivatives as the curve is called the *osculating circle*, shown in Figure 2.3. The radius of this circle is called the *radius of curvature*, and the *curvature* is the reciprocal of this radius (sometimes measured in mm^{-1}). Clinicians think of curvature in terms of diopters (D), which is linearly related to geometric curvature by a simple scale factor as

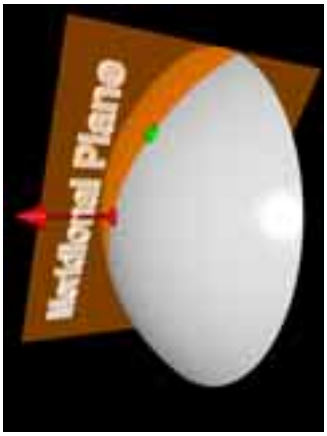

Figure 2.4: The meridional plane is depicted in orange. This plane contains the corneal point of interest (shown as a green dot) and the corneal topographer axis (depicted as a red vector).

in Equation 2.1. As an example, a spherical cornea with a radius of 8 mm would have a curvature of $\frac{1}{8}$ mm^{-1}, or $42\frac{3}{16}$ D.

$$\text{Curvature [D]} = 337.5 \times \text{Curvature [mm}^{-1}\text{]} \tag{2.1}$$

However, the data representing our corneas is three-dimensional, whereas curvature is a two-dimensional concept. Thus, we need to determine how to take a particular planar cross-section through the data to calculate the curvature in that plane.

2.1.3 Axial and Instantaneous Curvature

The usual approach taken by developers of corneal topographers is to take radial cross-sections going through the CT axis. Thus, the curvature at a particular point is calculated in the plane that contains the point and the CT axis; this is called the *meridional plane*. Figure 2.4 shows a meridional plane, depicted in orange[1]. The red vector represents

[1]All color figures can be found online at `http://www.cs.berkeley.edu/~ddgarcia/CWhatUC/`.

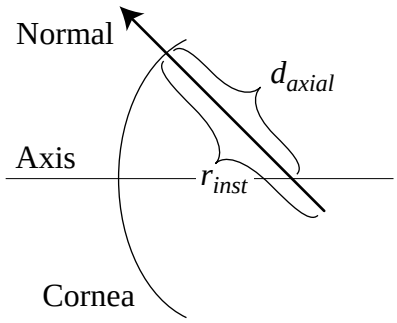

Figure 2.5: The axial distance d_{axial} and instantaneous radius r_{inst} are shown defined in the meridional plane.

the CT axis and the red dot is the point where the CT axis intersects the cornea. The corneal point of interest is shown as a green dot. This method provides measurements of both *axial* and *instantaneous curvature*.

Axial curvature is defined as:

$$C_{axial} = \frac{337.5}{d_{axial}} \tag{2.2}$$

where d_{axial} is the *axial distance* (measured in mm) along the corneal normal from the corneal point to the center of curvature truncated by the CT central axis as in Figure 2.5. Axial curvature is expressed in diopters when the CT central axial distance is given in millimeters.

Instantaneous curvature is analogous to the standard mathematical definition of curvature, and is defined as:

$$C_{inst} = \frac{337.5}{r_{inst}} \tag{2.3}$$

where r_{inst} is the *instantaneous radius*, which is simply the standard mathematical definition of radius of curvature illustrated in Figure 2.5. Instantaneous curvature is expressed in

diopters when the radius is given in millimeters.

These representations have several shortcomings: there is a singularity, which is due to any asymmetry on the cornea at the CT axis, and the corneal map changes appearance and value depending on the location of the CT axis. Fortunately, there are representations that overcome these problems.

2.1.4 Minimum and Maximum Curvature

From differential geometry [19, 24], it is known that at each point on a smooth surface, there exists a unique direction (assuming not locally a sphere) along which the curvature of the surface is a maximum and another along which it is a minimum. Furthermore, these two directions will always be orthogonal provided that the surface is continuous in the first and second derivatives at that point. This is a reasonable assumption for the cornea because even in the case of laser ablative refractive surgery, the epithelium (the outer-most layer of the cornea) would be smooth. The *maximum* and *minimum* curvatures are called the principal curvatures and the directions along which these principal curvatures lie are called the principal directions.

In Figure 2.6, the yellow cross-sectional plane contains the normal vector (shown in green) at the point of interest (shown as a green dot). Imagine spinning the yellow plane around the normal, and computing the normal curvature in all directions. The two directions of interest to us are the principal directions, mentioned above. Figure 2.7 shows this; the planes corresponding to the minimum and maximum curvature directions are shown in blue and red, respectively. At each point on the surface of the cornea we calculate the principal curvatures, convert them to diopters as in Equation 2.1 above, and generate

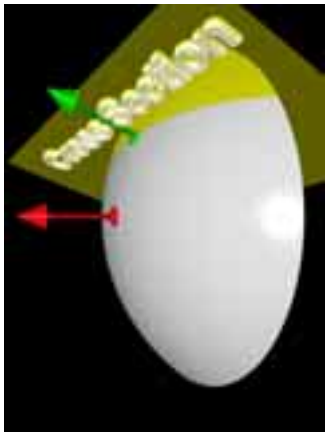

Figure 2.6: The yellow cross-sectional plane contains the normal vector at the corneal point of interest (both shown in green).

topography maps.

2.1.5 Gaussian Curvature with a Cylinder Overlay

It is often informative to look at the same quantitative information in several ways; this is the motivation for the following visualization. The difference of the principal curvatures (in diopters) is called *cylinder*, their arithmetic mean is called *mean sphere* and their geometric mean (square root of the product) is called *Gaussian power* [24]. We find it preferable to use the word "Gaussian curvature" (in dioptric units) rather than "Gaussian power" because the quantity being expressed is a representation of shape rather than of refractive power. This is a strategy followed in two papers by Klein [58, 59]. Since there is a strong mathematical correlation between the arithmetic and geometric means, the mean sphere is very similar to Gaussian curvature; thus, we will consider only Gaussian curvature and not mean sphere.

Instead of visualizing cylinder and mean sphere in two separate maps as in [69], we

Figure 2.7: The planes corresponding to the minimum and maximum curvature directions are shown in blue and red, respectively.

add a twist which allows us to view the two relations simultaneously. We overlay a cylinder vector field on top of the Gaussian curvature map, where each vector shows the orientation of the minimum curvature, similar to what we did in [5]. This illustrates the principal directions over the cornea by the direction of the vectors. Since vectors can represent more than just orientation, we use the length to depict the amount of cylinder; that is, the lengths of the vectors are scaled according to the amount of cylinder at each point.

We use this scaling for clarification — the larger the difference between the principal curvatures, the more important is the direction of the vectors. Also, recall that the minimum and maximum curvatures are orthogonal at any corneal data point (as long as they are nonzero and unequal). Although we allow the display of either the minimum and maximum curvatures, we propose the use of the minimum curvature. This shows the least curved ("flattest") direction: for a cylindrically-shaped surface, this would show its axis.

2.1.6 Related Work

The reason clinicians have desired precise information about the corneal shape has shifted over the years. Early on, it was the diagnosis of corneal diseases, then it was proper fitting of contact lenses, and more recently evaluation of pre- and postoperative refractive corneal surgery and overall corneal diagnostics [15, 56]. The use of a computer to visualize corneal shape is often called computerized corneal topography (CCT), and the manner in which the data is presented to the clinician can significantly affect the efficiency of interpretation.

Pseudo-color maps have become the standard method for displaying the topography of the cornea [110]. Axial power maps are the most popular, which Klein and Mandell [62] show are extremely robust to noise. They also mention that instantaneous power is quite effective, as it is sensitive to local curvature. However, possible misinterpretations of these maps are pointed out by Barsky et al [5], who suggest the use of alternative multi-dimensional representations based on surface principal powers, such as Gaussian power with cylinder vector fields. Vos and Spoelder [112] discuss a three-part representation, including a 3D display of shape deviation from a best-fitting ellipsoid, height contour lines and mean radius of curvature. Schwiegerling and Greivenkamp [96] also argue for the use of height maps, and remove single or multiple reference surfaces to allow for analysis of the resulting basis functions.

The use principal curvatures to visualize surface shape is not new to the field of computer graphics. Beck et al [8] and Hagen et al [39] each developed a suite of methods for analyzing geometrical properties (e.g., surface "fairness") of analytical surfaces. More

recently, Interrante [54] used principal directions to define a natural "flow" over the surface and create a stroke texture to represent shape in an intuitive way.

2.2 Geometric and Wave Optics

In this section we will review some of the basic optics we will use throughout the dissertation. We begin with the physics of reflection and refraction, continue with apertures and diffraction and conclude with an explanation of the relevant wave optics.

2.2.1 Reflection and Refraction

When light passes through a boundary from one media to another, it undergoes reflection and refraction. Reflection is the "bending back" of light from whence it came, derived from the Latin word *reflectere* [55]. The reflected ray lies in the same plane as that formed by the surface normal and the incoming ray. The law of reflection shown in Equation 2.4 determines $\theta_{reflected}$, the *angle of the reflection*, defined as the angle between the reflected ray and the surface normal. It states that $\theta_{reflected}$ is equal to $\theta_{incoming}$, the *angle of incidence*, defined as the angle between the incoming ray and the surface normal. This is illustrated in Figure 2.8 for a ray passing from air to the cornea. It is useful to remember that Equation 2.4 holds true independent of the wavelength of the incoming light [55].

$$\theta_{incoming} = \theta_{reflected} \tag{2.4}$$

We are fortunate that the cornea is a smooth and highly *specular*, or mirror-like

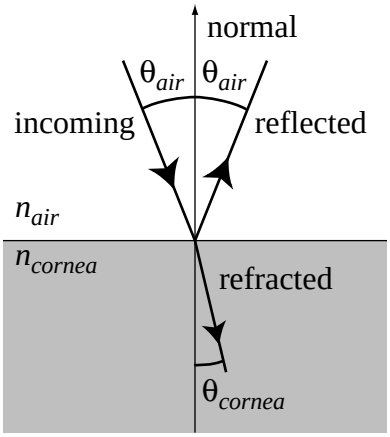

Figure 2.8: Snell's law governs the angular relationship of refracted rays as they pass from one medium to another, here shown passing from air ($n_{air} = 1.0$) into the more dense cornea ($n_{cornea} = 1.3375$). The path of the reflected ray is governed by the law of reflection, which states that the angle of reflection is equal to the angle of incidence.

surface, as the incident angles of neighboring parallel light are similar. This is not the case for *diffuse*, or rough surfaces, whose reflected light is diffused in all directions. It is exactly this specular reflection that allows the CTs to capture the images of the target rings of light, as in Figure 1.2.

Refraction is the bending of light when it enters a different media, derived from the Latin word *refractus* [55]. Most people are familiar with this phenomenon when they place an object under water, which seems to bend the object at the surface [84]. The physical basis for refraction is that light changes speed when it passes into a new medium, and thus the light wavefront changes direction. To understand this more clearly, it is helpful to look at the *wavefront* of the light rays.

The wavefront of light is parallel to the direction of travel, and the light waves are regularly spaced as they travel through air. As the light enters a denser medium, the lower edge of the wavefront slows down first, while the upper edge is still in air traveling

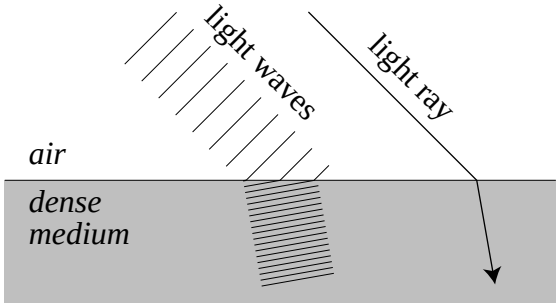

Figure 2.9: The reason for the refraction of light as it enters a denser medium can often be understood by examining the wavefront and the density of light waves.

at the initial speed. When the upper edge finally reaches the boundary, the lower edge has traveled less distance due to its slower speed. The overall effect is that the direction of the wavefront (and thus, the ray) changes, bending toward the normal [55]. This is illustrated in Figure 2.9.

The denser the material, the slower the speed of light in it. The *index of refraction* characterizes the ratio of c, the speed of light in a vacuum to v, the speed of light in that medium, we call this value n [55]:

$$n = \frac{c}{v} \tag{2.5}$$

The index of refraction for air (n_{air}) at 20° and 1 atmosphere is 1.0003 [55]; we use the Gullstrand approximation of 1.0 [90]. The effective index of refraction for the cornea (n_{cornea}), is 1.3375 [49]. As in the case of reflection, the refracted ray lies in the plane determined by the incoming ray and the surface normal. *Snell's law* governs the relationship between the angle of incidence and the angle of the refraction:

$$n_{air} \sin\theta_{air} = n_{cornea} \sin\theta_{cornea} \tag{2.6}$$

One important concept is the *principle of reversibility* (or *reciprocity rule* as in [26]), which states that if light can get from point A to point B, it can also get from B to A [55]. This principle is the key concept that allows Snell's law to hold true independent of the light ray direction. Thus, when light travels from a dense medium to one that is less dense (e.g., from the cornea to air), the rays refract away from the normal in accordance with Snell's law. We make use of this when we calculate wavefront aberrations [47], by placing a simulated point light source within the eye and charting the progress of the wavefront as it exits the cornea.

2.2.2 Apertures and Diffraction

We begin with some terminology. Rays near the axis of an optical system are called *paraxial* rays, and those far from the axis are called *peripheral* rays. When we are tracing light rays (or when nature is doing the work) through optical systems, it is often useful to limit how much gets through. As we will see in Section 2.3, sometimes peripheral rays cause us problems, so we would like to remove them and improve image quality.

We introduce a *stop* to the system, usually a circular opening from an opaque screen. We also include the edges of our optical system as stops [12]. The maximum diameter a light beam can pass is called the *aperture*, and its image is called the *entrance pupil* [14]. The *exit pupil* is the image of the aperture stop formed by the components of the optical system past it. The ray which passes through the center of the entrance pupil is known as the *chief ray*; it is also called the *principal*, or *reference* ray. If there are no aberrations (see Section 2.3) present, that ray will also pierce the center of the aperture stop and the exit pupil.

It would seem that, since image quality increases as we decrease our aperture, it makes sense to restrict it as small as possible, down to a pinhole. There are two problems which crop up with small apertures: greatly reduced brightness (since far less of the beam passes through), and *diffraction*. The latter is the bending of light around an opening, and only occurs when the opening is very small [35]. As most incoming light to the eye is not monochromatic, the effects for the various wavelengths overlap and is not as apparent [40].

In the eye, the pupil acts as our stop, changing size in reaction to the amount of incoming light. The human visual system has a remarkable ability to successfully adapt to scenes of varying intensity. In our modeling of the eye and light transport, we primarily ignore diffraction effects, except when comparing the visual performance of the eye to an ideal, or *diffraction-limited* system.

2.2.3 Light Waves

We can investigate the quality of an optical system by considering light *rays*, tracing them to find out how well they focus, or light *waves* and watching how they propagate. Ray tracing is something familiar to those in computer graphics and vision science [27], and it involves calculating the refraction and reflection as described earlier in Section 2.2.1. The field of wave optics may not be as familiar; we review several key concepts here.

A distant point light source in a uniform medium emits light waves with equal energy and speed in all directions. As the waves get farther away from the source, their curvature drops inversely, and eventually can be considered plane waves as in Figure 2.10. When this assumption is made, the point source is said to be at *optical infinity* [55].

The degree of *convergence* or *divergence* of light waves at a location is called the

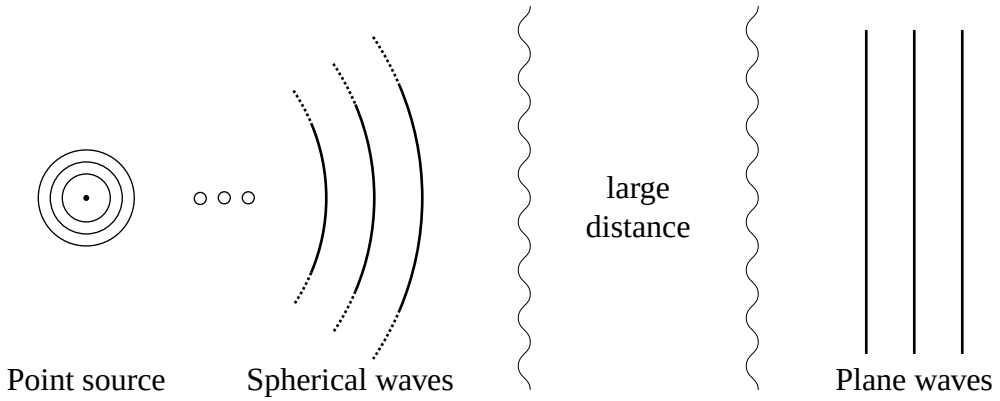

Figure 2.10: Spherical waves emanating from a point source of light. At great distances, these waves approach the shape of plane waves.

vergence of the light. In air, it is equal to the curvature of the wavefront we learned about in Section 2.1.2. The units are therefore the same as curvature, $\frac{1}{m}$. Waves that are converging are positive and those that are diverging are negative. Plane waves have zero curvature and thus zero vergence.

Let us consider an ideal optical system; it would have the ability to take the waves radiating from the point source in Figure 2.10 and make them converge to a single point. That is, it would take waves that are diverging and have them converge to the focus, as in Figure 2.11. The approximate shape of the lens that accomplishes this task is shown in grey; lenses that change diverging light to converging light are called *positive lenses*.

Our optical system was able to change the vergence of the wavefront because light travels at different speeds through different media. We saw this earlier in Section 2.2.1 as the reason for light *rays* bending with refraction. Here we see it bending a light *wavefront* — different ways to describe the same effect. This is because the paraxial rays had to travel longer through the thickest portion in the center of the lens and slowed down the most. The peripheral rays traveled through the least lens thickness so were slowed down the least.

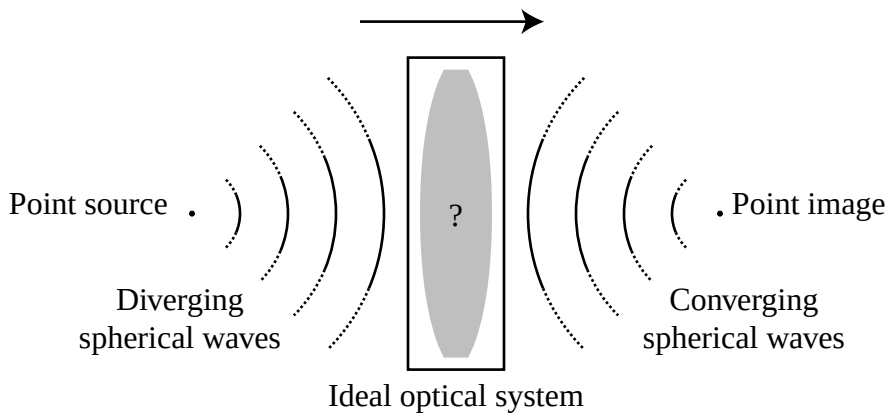

Figure 2.11: Diverging waves pass through our ideal optical system and converge to a point. The approximate shape of the positive lens that performs this process is sketched in grey.

.

If we think of light in terms of *time*, as Feynman suggests in [26], we come up with a new way of looking at this. The wavefront, in essence, describes all the light that left the point source at the same time. Let us say, for a particular location (x, y) on the wavefront (i.e., for a particular ray), we wish to know t, how long it has been since it left its home at the point source. This calculation would involve summing up the time it spent in various media, as follows:

$$t(x, y) = \sum_{i \in media} t_i \tag{2.7}$$

where $media$ is the set of all the media through which the ray traveled and t_i is the time spent in $media_i$. But we do not know t_i, it all went by so fast! We *do* know the path the ray took, perhaps we can figure it out from there. We recall from our first year of physics [86] the relationship between time, distance and velocity to be

$$t_i = \frac{d_i}{v_i} \tag{2.8}$$

and we know we can compute the distance d_i from geometry. We also know the velocity of light v_i is inversely proportional to the index of refraction, from Equation 2.5. Thus, given that

$$v_i = \frac{c}{n_i} \tag{2.9}$$

we now have all the machinery to find $t(x, y)$. Replacing v_i in 2.8, we get

$$t_i = \frac{d_i c}{n_i} \tag{2.10}$$

and replacing this into Equation 2.7,

$$t(x, y) = \sum_{i \in media} \frac{d_i}{\frac{c}{n_i}} = \sum_{i \in media} \frac{d_i n_i}{c}, \tag{2.11}$$

exactly what we wanted. The interesting thing is that $\frac{1}{c}$, in units of $\frac{s}{m}$, is present in every term. If we were to divide out this constant from Equation 2.11, we would get a measure of *distance*, which is known as the *Optical Path Length*, or *OPL*:

$$OPL(x, y) = \sum_{i \in media} d_i n_i, \tag{2.12}$$

We will make significant use of OPL in Chapter 4, where we attempt to predict patient's acuity by analyzing the wavefront aberration. Note that this derivation is based on ray tracing and is thus an approximation to the wavefront rather than true wave optics.

2.2.4 Coddington's Equations

A wavefront, as we will see in Section 2.3, can be classified by a Taylor series expansion. For a moment, let us assume we only care about the direction of the central ray and the principal curvatures of the wavefront. When this wave refracts into a different media, the central ray bends as we have shown, according to Snell's law. The principal curvatures of the resulting wavefront may also change as a function of its original pre-refraction values as well as the principal curvatures of the surface itself. *Coddington's equations* quantitatively describe this relationship [70, 100]; we will make extensive use of them in Chapter 4.

2.3 Aberrations

Aberrations are any optical sources which degrade image quality, blur the image, or create a loss of acuity [18, 55]. There are two sub-classifications commonly used here, *chromatic* and *monochromatic*. Chromatic aberrations describe the *dispersion* that occurs when white light passes through a prism as in Figure 2.12; the outgoing light is dispersed into its component spectra. The physical basis for this effect is that the refractive index, n, of the material varies with wavelength [26]. In this dissertation, we ignore chromatic aberration, choosing instead to focus on aberrations from light of a single frequency.

To design a lens that focuses all light perfectly from one point to another requires a tremendously complicated surface, so most lens designers consider only paraxial rays. The geometric optics then reduce to very simple equations, and the resulting lens surfaces are straightforward combinations of primitive geometric shapes: spheres, cylinders and tori. A

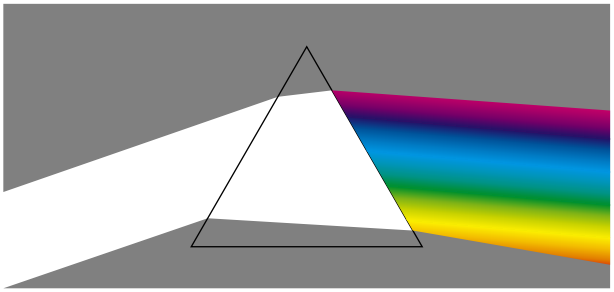

Figure 2.12: A prism disperses incoming white light into its spectra [105].

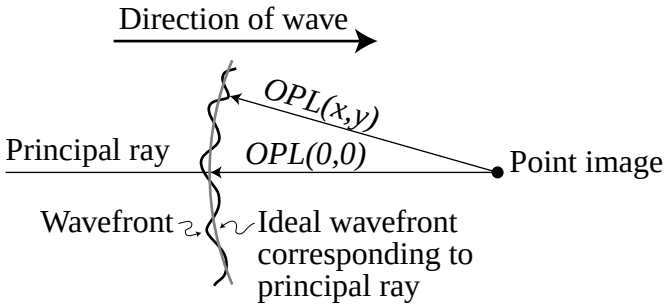

Figure 2.13: As the wave approaches its target, it may deviate from an ideal spherical wave; this deviation is called the wavefront aberration. It is measured by calculating the difference between the Optical Path Length (OPL) of the principal ray (whose corresponding perfect spherical wavefront is shown in grey) and the OPL for the other rays, at location (x, y).

few problems arise when we use these shapes for lenses, not the least of which is that all the peripheral rays don't always land at the same place as their paraxial brethren. This leads us to a discussion of different classifications of monochromatic aberrations in general.

Recall the converging wavefront from Figure 2.11; ideally it is a perfect spherical wave. Any deviation from this is called *wavefront aberration*, expressed as $W(x, y)$ (in microns), where x and y are normalized coordinates at the exit pupil (in mm):

$$W(x, y) = OPL(x, y) - OPL(0, 0) \tag{2.13}$$

That is, for every point (x, y) on the wavefront, we calculate the difference from its

OPL to that of our reference OPL from the principal ray at $(0,0)$, as shown in Figure 2.13. The grey wavefront is the ideal wavefront corresponding to the principal ray. If we then do a Taylor series expansion of $W(x,y)$ as in [48] we get:

$$\begin{aligned} W(x,y) &= A + \\ & Bx + Cy + \\ & Dx^2 + Exy + Fy^2 + \\ & Gx^3 + Hx^2y + Ixy^2 + Jy^3 + \\ & Kx^4 + Lx^3y + Mx^2y^2 + Nxy^3 + Oy^4 + \cdots \end{aligned} \tag{2.14}$$

The coefficients of the terms tell a great deal about the wavefront itself. Zero-order term A is the offset, and first-order terms Bx and Cy are the tilt, or horizontal and vertical *prism* terms familiar to ophthalmologists. Second-order terms with coefficients D through F are the sphere, cylinder and axis, used to describe spectacle correction. The third-order terms G through J are often called *coma-like* aberrations and are characteristic of de-centered spherical optical systems [71]. The fourth-order terms K through O add additional unique components to the overall aberration and are called spherical aberration.

2.3.1 Spherical Aberration

Spherical aberration [67] is most easily seen in optical systems that we create from primitive geometric shapes, such as spheres. Spherical-surface lenses work very well paraxially, and are used in spectacle design today. However, as rays deviate from the axis, they begin to fall short of the focus. This is because the refractive power of these optical

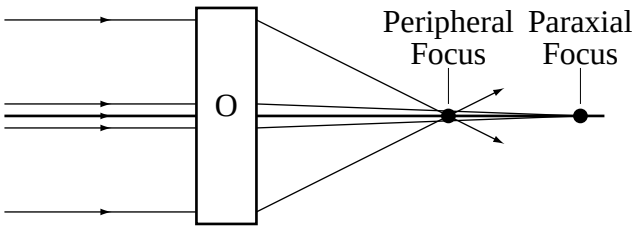

Figure 2.14: A side view of optical system O exhibiting spherical aberration for incoming parallel light from a distant object. The peripheral rays converge faster than the paraxial rays.

systems increases away from the axis, as shown in Figure 2.14 [26, 28, 55].

As we will see, spherical aberration affects the formation of a good focus, instead causing a smear, or blurred image. To eliminate this effect, we must use *aspheric* surfaces. One which does not exhibit any spherical aberration is called a *Cartesian oval* [55]. One special case is the "perfect ellipsoid"; we will investigate this surface in Section 3.2.4. It is useful to note that this aberration is represented by the Taylor terms with coefficients K, M and O [48] from Equation 2.14. An example of this expressed as a wave aberration [14] is

$$W(x, y) = (x^2 + y^2)^2 \tag{2.15}$$

which we display as a three-dimensional surface in Figure 2.15.

2.3.2 Astigmatism

Astigmatism is the most common aberration to the layman, and is used to describe the presence of any rotational asymmetry in an optical system. This asymmetry results in two separate and distinct foci, one for each principal direction of refractive curvature. The primary, or more curved direction comes to a focus first, at point A in Figure 2.16. Then

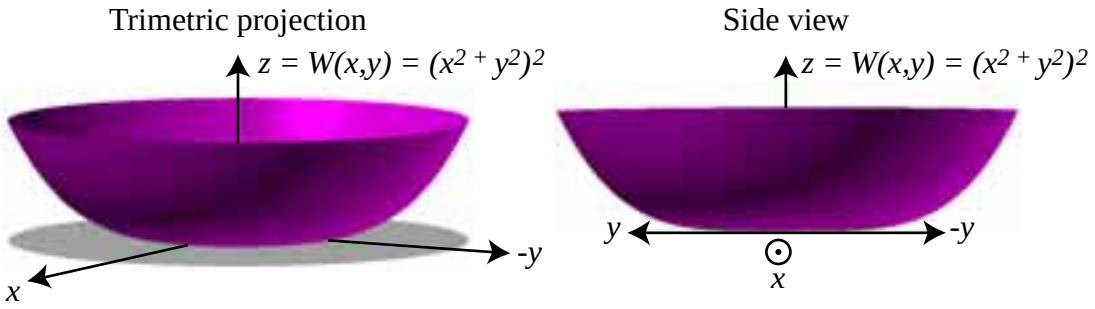

Figure 2.15: Two three-dimensional views of an example of the primary aberration *spherical aberration* viewed as the wave aberration $z = W(x, y) = (x^2 + y^2)^2$. A trimetric projection is on the left and a side view on the right. Spherical aberration is a common problem for lenses; peripheral rays converge more quickly than paraxial rays, resulting in a blur.

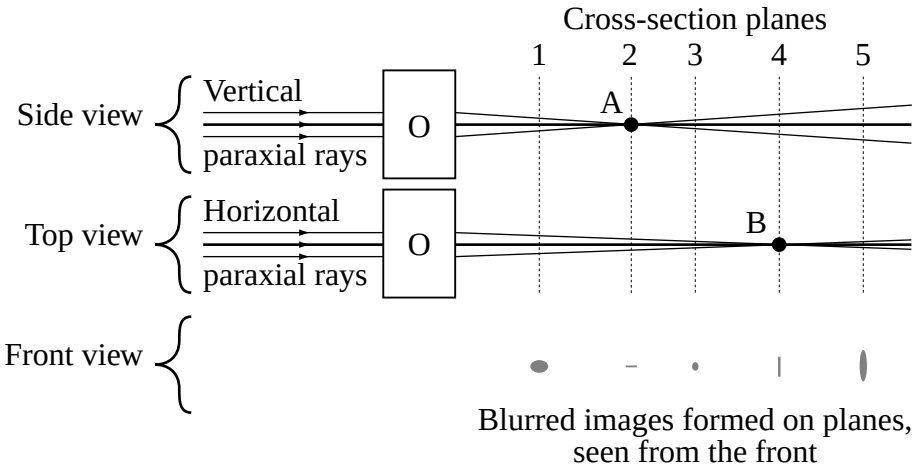

Figure 2.16: Three views of optical system O exhibiting *astigmatism* from a distant point source of light. The top image is a side view showing the vertical paraxial rays converging to point A on plane 2. The middle image is a top view showing the horizontal paraxial rays converging to point B on plane 4. The bottom image is a cross-section through the rays, showing how the blur changes shape as we move from planes 1 through 5. We see the blur as a vertically collapsing oval until plane 2, where it degenerates to a small horizontal line. By plane 3 it is almost circular; this is our *circle of least confusion*. Then the horizontal rays finally converge at point B on plane 4 and the result is a vertical blurred line. Past point B the blur remains a tall and thin oval, shown on plane 5.

the secondary focus is reached farther back, at point B in Figure 2.16. At each of these foci the image from a distant point light source is a thin sliver, oriented with the principal curvatures. Between the foci is a point where the blur is most circular; this is called the *circle of least confusion.*

The amount of astigmatism is described as a degree of *cylinder* and its corresponding *axis*, because sections of cylinders were the geometric shape initially used to induce and correct the effect. The disadvantage of the use of a cylinder with principal powers $(C, 0)$ for correction is that its mean power is nonzero (it is $\frac{C}{2}$) so it contributes residual power to the optical system. In 1887 Jackson introduced a *cross cylinder* approach which had lenses with principal powers equal but at opposite signs, e.g., $-\frac{C}{2}, \frac{C}{2}$ for a lens with cylinder C. These had the benefit that they did not contribute any residual power, since their mean power was zero [90].

Uncorrected astigmatic light distribution typically manifests itself as an oval smear on the image plane. From a wave optics point of view, it is the terms D through F which capture the sphere, cylinder and axis from the wavefront aberration [113]. One example of this from [71] is

$$W(x, y) = y^2 \tag{2.16}$$

which is viewed in three-dimensions in Figure 2.17.

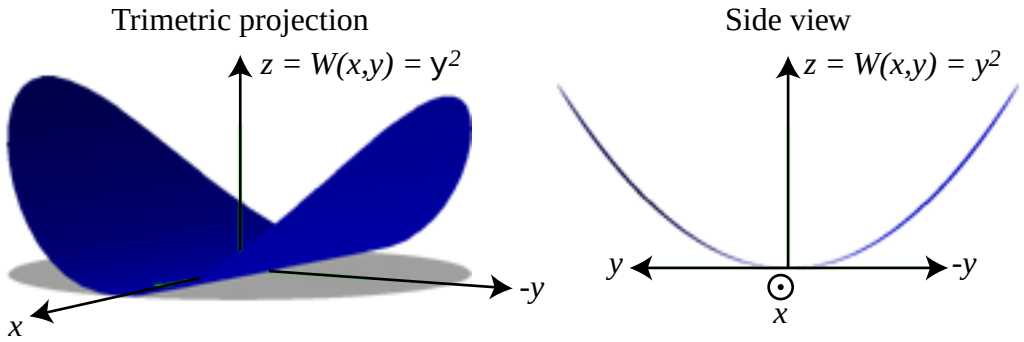

Figure 2.17: Two three-dimensional views of an example of the primary aberration *astigmatism* viewed as the wave aberration $z = W(x, y) = y^2$. A trimetric projection is on the left and a side view on the right. Astigmatism adds an asymmetry to the wavefront, by contributing refractive power in one direction but not the other. This is known as adding a "cylinder" component, which blurs the image point.

2.4 Corneal Acuity Visualization

Broadly speaking, *visual acuity* is the measurement of the ability of the eye to resolve images and distinguish form and detail [10, 25]. *Corneal* visual acuity is the corneal contribution to the overall vision [38]. In this section, we explain common visual system classifications and how clinicians correct for many of them. We close the chapter with a review of related work in corneal acuity visualizations.

2.4.1 Eye Classifications

Eyes are generally classified into three categories: *emmetropic*, *myopic*, and *hyperopic*. In addition, eyes may contain some astigmatism, mentioned earlier in Section 2.3.2. An excellent characterization of these conditions is found in [55], and is briefly summarized in the following subsections. A comparison of their vision when viewing a distant object is shown in Figure 2.18. In addition, there are two corneal disorders we study at the end of the section.

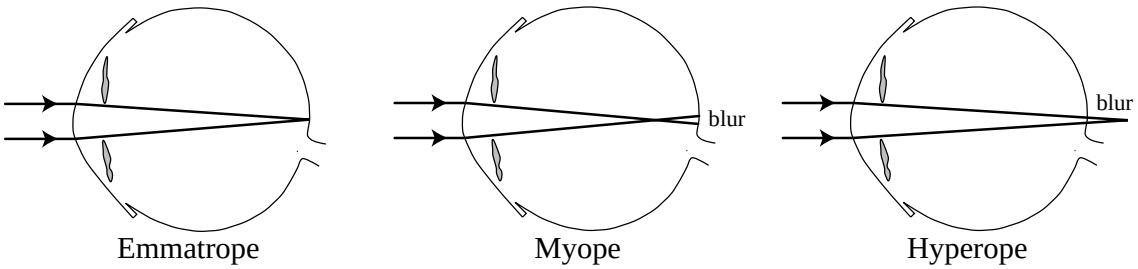

Figure 2.18: A side-view of an emmetropic, myopic and hyperopic schematic eye shown unaccommodated viewing a distant object. Note the retinal blur in the rightmost two ametropic eyes.

Emmetropia

Emmetropic eyes are those which when relaxed, or *unaccommodated*, focus distant parallel light well onto the retina as shown in Figure 2.18. Patients who are not emmetropes are called *ametropes*. Accommodation is the process of "focusing your eye" on something, which involves a tightening of the ciliary muscle around the crystalline lens to increase its power. To view near objects, emmetropes simply accommodate accordingly. When people age, their lens becomes harder and doesn't change its shape as easily as before, limiting the amount of accommodation that can be done. People with this condition are called *presbyopes*.

Myopia

Myopia, or *nearsightedness*, describes an eye which, when unaccommodated and viewing a distant eye, focuses the light in front of the retina. This causes distant objects to be blurred out, as shown in Figure 2.18. However, as the object nears the eye, there is a distance M_R, called the *far point*, at which the unaccommodated eye sees in perfect focus. If the object is moved closer than that point, the eye simply accommodates to keep it in

focus. As myopes age, they don't have that luxury, so their uncorrected eye can only see objects when placed at roughly M_R.

Myopia is caused when the cornea is too highly curved, the eyeball is too long, or both. There are several refractive surgeries described below in Section 2.4.2, all of which are primarily aimed at flattening the myopic cornea to correct its vision.

Hyperopia

Hyperopia, or *farsightedness*, is the opposite of myopia, in that the unaccommodated eye focuses distant light behind the retina. This also causes a blur for distant objects, as shown in Figure 2.18. To compensate, the hyperope simply accommodates to focus the incoming light more, and thus can see distant objects, unlike myopes. As the objects is brought near the eye, the degree of accommodation increases correspondingly. As hyperopes age and lose that ability, they have difficulty seeing anything in perfect focus without spectacle or surgical correction. There are several refractive surgical techniques to correct hyperopia by increasing the curvature, or *steepening* the cornea. Hyperopia is caused by a cornea which is too flat, or an eye which is not long enough, or both.

Astigmatism

Astigmatism refers to a lack of rotational symmetry in the cornea, preventing incoming light from forming a crisp focus. This asymmetry means that the cornea has a higher curvature in one direction than another. It is the most common optical aberration affecting human vision, although for mild astigmatism its effect might be slight. PARK (described in Section 2.4.2) is a refractive surgical technique intended to correct this prob-

lem. Clinicians often model astigmatism with an ellipsoid or torus; we choose an ellipsoid as discussed in Section 3.2.3

Keratoconus

As mentioned in Section 1.1 of the Introduction, keratoconus in an eye condition which usually reduces a patient's visual acuity. It results in the bulging and thinning of the cornea, as well as localized regions of high curvature. It is critical that keratoconus be diagnosed; performing refractive surgery on a keratoconic eye is malpractice [83].

Monocular Diplopia

Diplopia is more commonly known as "Double Vision", which occurs when a patient fixates on a single object but perceives multiple objects. It is usually caused by problems with the muscles of the eye preventing a unique fused image from being formed. Monocular diplopia is slightly different; the shape of the cornea of a single eye creates multiple images of an object as in Figure 2.19. It is believed to be caused by corneal warpage, trauma or keratoconus.

2.4.2 Corrections

There are several techniques to correct some of the refractive defects we just mentioned. The most common is to pre-refract the light rays before they enter eye with spectacles or contact lenses with the desired corrections [43]. Another which has become quite popular of late is *corneal refractive surgery*, which aims to change the shape of the cornea with either a scalpel or laser. These are briefly described below.

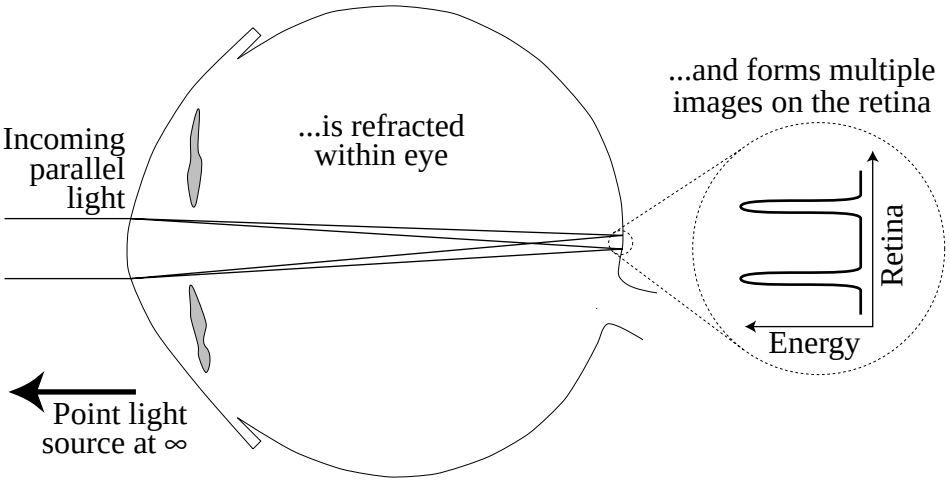

Figure 2.19: Monocular diplopia is a corneal condition in which a single distant point light appears to the patient as two lights.

RK

Radial keratotomy (RK) is a surgical technique intended to correct myopia. Radial cuts are made with a scalpel outside of the central, "optical zone", with the intention to weaken the cornea. When it heals, it flattens, thus reducing some of the curvature and moving the focal point back toward the retina. The surgeon adjusts the lengths and number of radial incisions (usually from 4 to 16) based on the desired correction. RK was the most common form of refractive surgery until the mid-1990s [7, 92], at which point its popularity was overtaken by laser-driven corrective surgeries. Almost three-quarters of a million Americans are expected to get their eyes "lasered" in 2000 [36]. Part of the reason for this was that the results from RK were hard to predict, and the healing process was painful and slow. A graphic representation a cornea with RK incisions is shown in Figure 2.20.

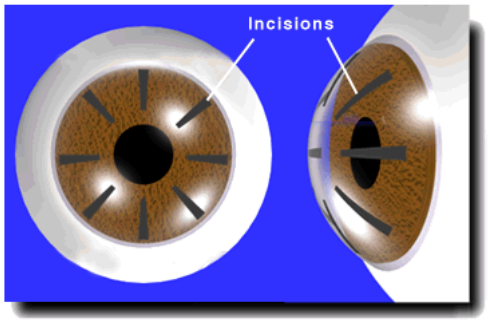

Figure 2.20: A cornea with eight RK incisions. (Reprinted with permission from [53]. ©1996-2000, Internet Media Services, Inc. All rights reserved.)

PRK and PARK

Photorefractive Keratectomy (PRK) is a surgical procedure also intended to correct myopic refractive defects [102], and was the first such procedure to use the excimer laser [36]. The procedure involves the ablation of the layers of the cornea with the intention of flattening or steepening it [33, 73], as shown in Figure 2.21. The surgeon controls the shape of the ablation depending on the amount of correction desired. After the surgery, it is important for the clinician to measure how the shape is healing, as it often takes six or more months for the shape and corneal clarity to stabilize [32, 46, 106, 111]. Although PRK was an improvement over RK, the healing of the front surface of the cornea was still painful.

Photorefractive astigmatic keratectomy (PARK) is similar to PRK, but there is an elliptical ablation following the regular ablation (if needed) to correct for astigmatism [33, 73]. We will be predicting the acuity for 62 eyes of patients who had undergone PRK and PARK surgery in Chapter 4.

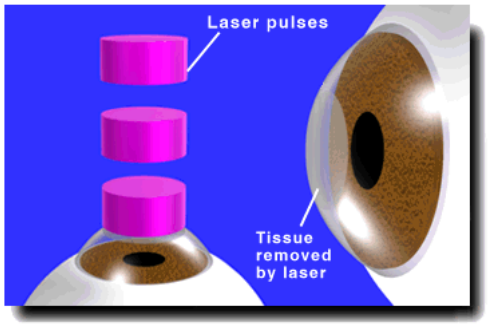

Figure 2.21: A graphical representation of the PRK process illustrating the ablation of the front surface of the cornea. (Reprinted with permission from [53]. ©1996-2000, Internet Media Services, Inc. All rights reserved.)

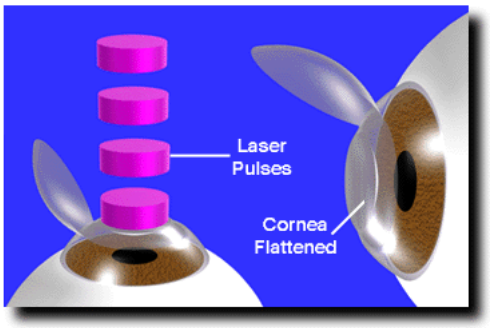

Figure 2.22: A graphical representation of the LASIK process illustrating the ablation of the front surface of the cornea beneath the flap. (Reprinted with permission from [53]. ©1996-2000, Internet Media Services, Inc. All rights reserved.)

LASIK

Laser In-situ Keratomileusis (LASIK) is similar to PRK in that it uses the same excimer laser to ablate the cornea. The difference is that with LASIK, a corneal flap is cut with a microkeratome, and the laser pulses ablate the central *stromal* layers of the cornea. The flap is then replaced, which reconnects with the cornea without the need for sutures. The surgery is primarily done to correct myopia, but it can be used to correct hyperopia as well, by ablating a doughnut-shaped region instead of a central spherical region [36].

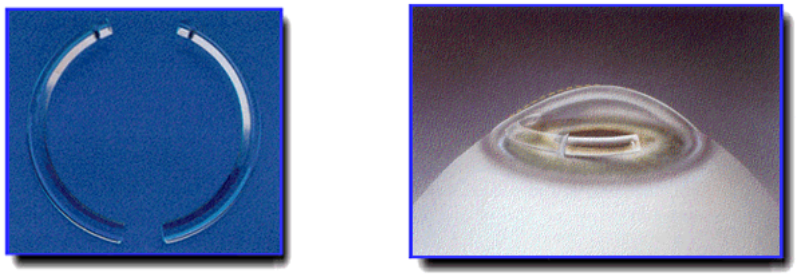

Figure 2.23: Intacs are clear, crescent-shaped rings as shown on the right. They are inserted into the stromal layers of the cornea to correct mild myopia, shown on the right. (Reprinted with permission from [53]. ©1996-2000, Internet Media Services, Inc. All rights reserved.)

This surgery was not available in the United States until 1996, and as mentioned earlier, is becoming the most popular form of elective corneal refractive surgery [36]. In the near future, it may be possible to have "custom LASIK", in which the surgery is much more tailored to the patient's overall visual system [36]. Common post-operative complaints of laser procedures are glare and diminished contrast. In Chapter 4, we use a test that measures small letter contrast sensitivity (SLCT) as one means for measuring the acuity of post-surgical patients. In Chapter 7, we attempt to simulate the effect that glare has on the visual field.

Other Corrective Surgeries

There are at least two other options for correcting vision without the need for lasers and scalpels: *Intacs* and *intra-ocular lenses*. Intacs are removable crescent-shaped rings placed within the stromal corneal layer as shown in Figure 2.23. This has the effect of pulling the cornea flatter [107], and is effective for mild myopes. That they are removable and leave the cornea intact is an attractive option for many. They were the first FDA-approved (in April of 1999 [36]) option for correcting myopia that did not include a laser [53].

Intra-ocular lenses are lenses implanted either behind the cornea or iris. They are effective for high myopia and hyperopia, and have the advantage that they leave the cornea intact. Their disadvantage is that they may lead to cataracts, corneal injury or intra-ocular infection [36].

2.4.3 Related Work

In this section we discuss the related work in the prediction, visualization and simulation of corneal visual acuity.

Prediction

Most of the research in the prediction and modeling of acuity centers on refractive corneal surgery. It is crucial that the surgeon have an accurate gauge of how the surgical parameters affect the eye's final shape and refractive properties. As mentioned in Section 2.4.2, RK was the earliest and most popular forms of surgery. Several models for optical performance prediction following RK surgery were presented by Howland et al [51], Patel et al [88], and Schwiegerling et al [97]. Ludwig et al [74] simulated PRK using the Gullstrand eye model and predicted the retinal image contrast loss. Finally, Van de Pol [107] evaluated visual performance after PRK, PARK and LASIK using high contrast visual acuity (HCVA) tests as well as small letter contrast tests (SLCT) to measure contrast sensitivity.

Visualization

In 1976 and 1977, Howland and Howland published their seminal papers [48, 50] on the subjective measurements of high-order monochromatic aberrations of the eye. They used a modified aberroscope and were able to de-construct the wave aberrations using a Taylor series expansion. Since then, Walsh et al [113] created an *objective* technique using a camera and beam-splitter. They analyzed the high-order Taylor coefficients for 11 patients, and confirmed earlier findings that coma-like aberrations play a dominant role for most pupil sizes.

The Hartmann-Shack Sensor [89] (HSS) is a device that provides a way to precisely measure the phase information of wavefronts. It uses between 50 and 200 lenslets to focus the rays emerging from the eye onto a CCD image array, which records it. The local slope of the wavefront is determined by the lateral offset of the focus from each lenslet. Phase information is then derived from the slope [60].

It is believed that the HSS is the most effective device for the measurement of human eye aberration [71]. It was used in conjunction with a laser tomographic scanner by Liang [71] to create a new technique to test aberrations and describe them with Zernike coefficients. More recently, López-Gil and Howland [72] used near infrared light (NIRL) to objectively measure aberrations, which is more comfortable to the subject because lower source irradiance is needed.

Klein [60] created an algorithm to calculate the optimal corneal ablation based on the phase information from the HSS, and Klein and Garcia [61] investigated alternate representations of the wavefront itself.

Simulation

With the advent of CCT and accurate corneal reconstruction, several researchers have simulated the acuity of the eye using ray tracing techniques to generate retinal light distribution. Camp et al created a ray tracing algorithm and computer model for evaluation of optical performance [16, 17]. Maguire et al employed these techniques to analyze post-surgical corneas using their optical bench software [76, 77]. Greivenkamp created a quite sophisticated model which included the Stiles-Crawford effect [85], diffraction and contrast sensitivity [37].

In the computer graphics domain, Kolb et al [66] created a realistic camera model including focusing and exit pupil effects. Spencer et al [99] simulated physically-based glare effects for digital images using a model which included parameters for age and light-adapted state. Finally, Debevec and Malik [22] devised an algorithm to recover high dynamic range (HDR) radiance maps from photographs, a critical step toward realistic simulations of glare and acuity.

Chapter 3

Corneas

— Mr. Boffo © 1997 Joe Martin, Inc. Reprinted with permission of Universal Press Syndicate. All rights reserved.

In this chapter, we explain the various corneal models we will be using. We begin with the representation we use for the eye itself, and explain some of the tradeoffs we make. Then we discuss three categories of corneal models: basic models created from

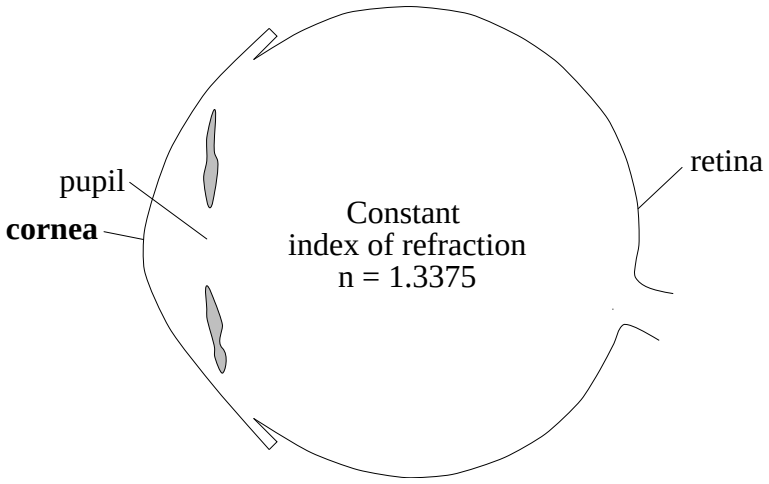

Figure 3.1: Our schematic model of the eye.

simple geometrical shapes, more elaborate models intended to simulate corneal conditions, and conclude with real corneal data from patients covering a wide range of eye conditions. Note that we adjust the parameters of each model eye to approximate the corresponding patient eye.

3.1 Schematic Eye Model

Figure 2.1 showed a side view of the human eye, with its many visual components. We decided to use a simple schematic model for our calculations based on Gullstrand's reduced eye [55]. We treat the entire eye to be a uniform medium with an index of refraction of 1.3375. This number represents the effective refractive index of the cornea [49]. We include a "pupil" (located at the front-most surface of the cornea) of variable diameter, which is used to cull away entering rays that do not pass through to the retina. The cornea itself is either an analytical function, such as an ellipsoid, or the reconstruction from the

measurement of a patient's eye [20].

We model the retina of the eye as a very small planar section, placed a certain distance from the front of the cornea. We adjust this retinal distance in Chapters 5 and 6 based on the best paraxial and overall focus, respectively. Figure 3.1 shows a diagram of our final computational eye model.

One obvious criticism is that this model ignores the lens, vitreous humor and corneal layers. It also does not account for scattering and the directional sensitivity of the cones on the retina known as the Stiles-Crawford effect [85]. In response, we bring up four points and one concluding remark.

First, we do not have lens data for the patient, although we could use a model eye; all we have is reconstructed corneal data. Second, adding other elements to our model would not change our results much, since the differences in indices of refraction of internal elements is not as great as that between the cornea and air. Third, ray tracing through several surfaces is computationally expensive due to the vast amount of intersection searching involved. Furthermore, to use a correct model of the lens with a gradient index of refraction would be prohibitively expensive; our model requires no searching, as we will see in Chapter 6. Finally, it is very possible that many of these techniques may be rendered obsolete with the advent of machines capable of capturing the full aberrations of the eye using Hartmann-Shack [89] information.

Let us now survey some of the basic corneal models we employ.

3.2 Basic Corneal Models

We have found it instructive to use simulated corneas when beginning to examine new visualizations. These simple shapes serve as a tutorial for clinicians who have experience with these shapes in other contexts, as well as "sanity-checks" for us that everything is working properly. We will consider four forms of general ellipsoids, a sphere (in which all ellipsoid axes are equal), an ellipsoid model of a "normal" eye, a "perfect ellipsoid" (which has very interesting refracting properties), and a general ellipsoid (in which each axis is a different length) to simulate astigmatism. We adjust the parameters for the first three models to resemble the normal cornea from Section 3.4.1 and the fourth to resemble the astigmatic cornea from Section 3.4.2.

We recall the equation for a general ellipsoid shifted by C in the z-direction so that its apex is at the origin:

$$\frac{x^2}{A^2} + \frac{y^2}{B^2} + \frac{(z-C)^2}{C^2} = 1 \tag{3.1}$$

which when solved for z gives us:

$$z(x, y, A, B, C) = \frac{ABC - C\sqrt{A^2B^2 - B^2x^2 - A^2y^2}}{AB}. \tag{3.2}$$

To simulate different ellipsoids, we only need to specify the different values of A, B, and C. For all data, both analytic and real, we translate the cornea so that the central corneal apex is at the origin, hence the shift above.

However, this representation has its limitations. If we wanted to choose an ellipsoid that had the same curvature as a sphere of radius R but with a variable *eccentricity* e, we

would have to vary A, B and C simultaneously. It would be nice if we had a model in which we could simply vary e. Let us look at another way of representing an ellipsoid, known as Baker's equation [3]:

$$pz^2 - 2Rz + r^2 = 0 \tag{3.3}$$

where

$$p = 1 - e^2 \tag{3.4}$$

and R is the radius of curvature of the ellipsoid at its apex. Thus, we can now specify our shape in terms of (A, B and C) or in terms of (R and e).

3.2.1 Sphere

A spherical cornea, the simplest of all the shapes, has the unique property that any cross-section containing the normal results in a circle with radius equal to that of the original sphere. We recall from our review of shape properties in Section 2.1.2 that this eye will therefore have constant values of any curvature-based calculation (axial, instantaneous, mean sphere, etc.) over its entire surface. We include this model as a reference surface when comparing shape and acuity metrics of our other corneas.

We'll set the parameters describing our sphere to be the same as that of the "normal cornea" data we will see in Section 3.4.1. That is, we set the radius such that its apical curvature is 43.5 D, where $R = A = B = C = \frac{337.5}{43.5} \approx 7.76$ mm. We recall the eccentricity of a sphere is zero. Equation 3.2 simplifies to:

$$z(x, y, R) = R - \sqrt{R^2 - x^2 - y^2} \tag{3.5}$$

which, when written in cylindrical coordinates, becomes:

$$z(r, \theta, R) = R - \sqrt{R^2 - r^2} \tag{3.6}$$

3.2.2 Ellipsoid Model of "Normal Eye"

Our sphere model of the previous section fails to capture the flattening of the cornea in the periphery. We would like to include a more accurate rotationally symmetric model of the eye. Using our representation from Equation 3.3, we choose a model with eccentricity $\frac{1}{2}$ and radius $R = \frac{337.5}{43.5} \approx 7.76$ mm to better approximate our normal eye from Section 3.4.1.

3.2.3 Ellipsoid Model of Astigmatism

Our general ellipsoid allows us to simulate astigmatism, which we wish to orient at any arbitrary axis. We modify Equation 3.2 to allow for rotation about the θ axis with the simple variable substitution:

$$x(x', y', \theta) = x' \cos\theta + y' \sin\theta \tag{3.7}$$

$$y(x', y', \theta) = -x' \sin\theta + y' \cos\theta \tag{3.8}$$

which when substituted for x and y in Equation 3.2 becomes

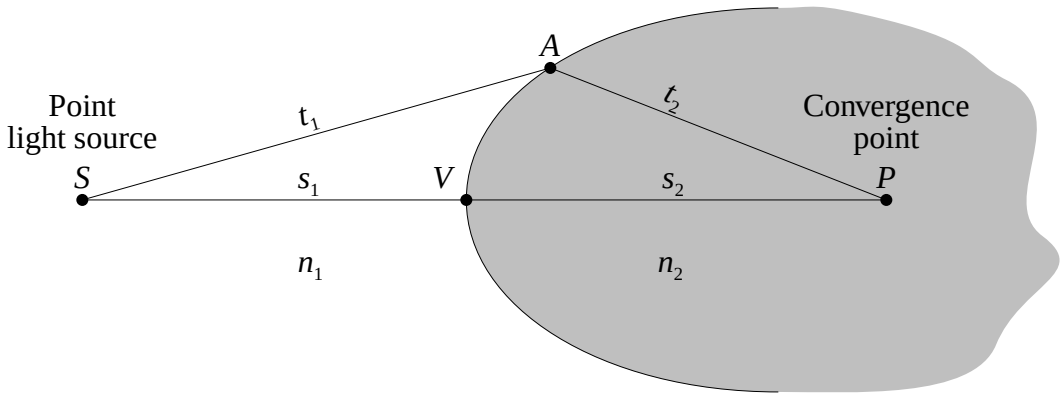

Figure 3.2: A Cartesian oval. All the rays from S converge at P with equal optical path length [44].

$$z(x', y', A, B, C, \theta) = \frac{ABC - C\sqrt{A^2B^2 - B^2x(x', y', \theta)^2 - A^2y(x', y', \theta)^2}}{AB}. \tag{3.9}$$

Fortunately, our real astigmatic cornea is *with the rule*, that is, its orientation is axially aligned and has higher curvature in the y-direction than x-direction. Therefore, we set θ to be zero. The curvatures in the principal directions for our real cornea from Section 3.4.2 are 42.5 and 44 D, so to match that we set C to be 11 mm, A to be $\sqrt{C\frac{337.5}{42.5}} \approx 9.35$ mm and B to be $\sqrt{C\frac{337.5}{44}} \approx 9.19$ mm.

3.2.4 Perfect Ellipsoid

In Section 2.3.1 we alluded to a surface with a remarkable refractive property — it had no spherical aberration. Every ray, peripheral and paraxial, fell perfectly on the focus. Let us see if we can derive such a surface, with a proof similar to the one presented in [44].

Perfect Ellipsoid Proof

In Figure 3.2, we would like to design a surface that takes every light ray emitted from point light source S and converges it to a single point, P. Where shall we start? Thankfully, we have the tools we learned in Chapter 2, such as optical path length at our disposal. We know that to eliminate wavefront aberration, every ray leaving S and arriving at P must have identical optical path lengths. This means that for all points A on the surface, the time from S to A to P must be the same as the time for the principal ray, from S to V to P. Applying Equation 2.12 for optical path length to this situation, we get:

$$t_1 n_1 + t_2 n_2 = s_1 n_1 + s_2 n_2 \tag{3.10}$$

but we know that for all A, the right-hand side of Equation 3.10 is fixed. This means

$$t_1 n_1 + t_2 n_2 = \text{constant} \tag{3.11}$$

and the only shape that satisfies this is a *Cartesian oval*. Figure 3.2 illustrates a cross-section through this ovoid shape; to generate a full 3D surface, we simply rotate the shape around the $\overline{SP}$ axis. Points S and P are called *conjugates*, because light from one will be imaged at the other (recall the reciprocity rule from Section 2.2.1). In fact, if we move S to optical infinity so that the incoming rays are parallel, two things happen. First, our ovoid transforms into an ellipsoid, and the location of P is easy to determine — it is the far focus of the ellipsoid! Let's see why.

We begin with a plane wave traveling toward our ellipsoid, as in Figure 3.3. If we look at the light ray that passes through point D, we see that it intersects our surface at

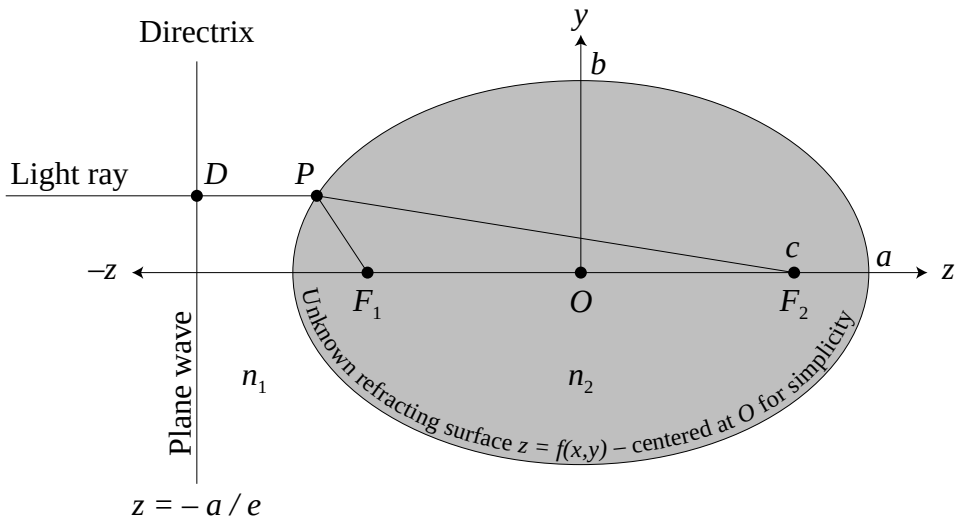

Figure 3.3: A perfect ellipsoid, which focuses all plane waves to a point (F_2) with no aberrations [44].

P and is refracted within the ellipsoid. If indeed the surface is to be "perfect", then the optical path lengths from any point D on the planar wavefront to the focus F_2 must be equal. That is, given some constant C,

$$n_1(\overline{DP}) + n_2(\overline{PF_2}) = C \tag{3.12}$$

which rewritten to isolate $\overline{PF_2}$ becomes

$$\frac{n_1}{n_2}(\overline{DP}) + (\overline{PF_2}) = \frac{C}{n_2}. \tag{3.13}$$

We recall from analytic geometry [101] that a *directrix* is a plane perpendicular to an ellipse's major axis and a fixed, particular distance away. The distance is such that for all points D, P and and F_1 as shown in Figure 3.3,

$$(\overline{PF_1}) = e(\overline{DP}) \tag{3.14}$$

where, as we recall, e is the eccentricity of the ellipse. It is defined as a function of c, the distance from the origin O to a focus, and a, the distance from the origin to the edge of the ellipse along the major axis in the following relation:

$$e = \frac{c}{a}. \tag{3.15}$$

Therefore, if we set

$$e = \frac{n_1}{n_2}, \tag{3.16}$$

we can replace $\frac{n_1}{n_2}(\overline{DP})$ in Equation 3.13 with $(\overline{PF_1})$ yielding

$$(\overline{PF_1}) + (\overline{PF_2}) = \frac{C}{n_2} = \text{constant} \tag{3.17}$$

which we know to be true, by the definition of an ellipse! That is, an ellipse is the locus of points which are a constant combined distance from the two defining foci.

Relationship Between Ellipsoid Parameters

Now that we have proved that the perfect ellipsoid is our ideal refracting surface and that all plane rays converge on F_2, we need to determine the relationship between a and b, the *major* and *minor* axes. We know the relationship between a and c from Equations 3.15 and 3.16 to be

$$c = \frac{n_1 a}{n_2}. \tag{3.18}$$

The relationship between a, b and c is given from analytic geometry [101]:

$$b = \sqrt{a^2 - c^2} \tag{3.19}$$

which we rewrite to isolate c:

$$c = \sqrt{a^2 - b^2}. \tag{3.20}$$

Combining Equations 3.18 and 3.20 we obtain our relationship between a and b in terms of n_1 and n_2:

$$\frac{n_1 a}{n_2} = \sqrt{a^2 - b^2}. \tag{3.21}$$

Squaring both sides, moving a^2 over, and eventually isolating $\frac{a}{b}$ we get what we wanted all along:

$$\frac{a}{b} = \frac{1}{\sqrt{1 - (\frac{n_1}{n_2})^2}}. \tag{3.22}$$

In this dissertation, medium n_1 will be air ($n_{air} = 1$) and n_2 will be the cornea ($n_{cornea} = 1.3375$). This means we can now assign a value to the right hand side of Equation 3.22:

$$\frac{a}{b} = \frac{1}{\sqrt{1 - (\frac{1}{1.3375})^2}} \approx 1.5 \tag{3.23}$$

which is a surprisingly simple approximated ratio.

Functional Representation

We had been operating in flatland until now, always suggesting we could migrate to 3D by spinning our surface around the z-axis. When we do this, our ellipsoid parameters of Equation 3.2 absorb the ellipse parameters we just solved for as follows:

$$A = b \tag{3.24}$$

$$B = b \tag{3.25}$$

$$C = a \tag{3.26}$$

since the z-axis remains our major axis, and the x- and y-axes are our identical twin minor axes. Recall that we always displace our surface so that its apex (the front-most part of the refractive surface) is snug with the origin. However, we will find with the monocular diplopia model that it is useful to move the ellipsoid around so that its apex is an arbitrary point $P_1 = (x_1, y_1, z_1)$. This is accomplished by the simple variable substitution in our primary $z = f(x, y, A, B, C)$ ellipsoid function from Equation 3.2 as such:

$$x' = x - x_1 \tag{3.27}$$

$$y' = y - y_1 \tag{3.28}$$

$$z' = z - z_1. \tag{3.29}$$

We are almost finished. Instead of characterizing this surface as a ratio of A and B to C, it would be useful if we could describe it as having the equivalent paraxial focusing

power of a sphere of radius r_1. We recall that our perfect ellipse from Figure 3.3 focuses all light to point F_2, which means paraxial rays travel

$$f_{PE} = a + c \tag{3.30}$$

units within the medium to the focus. Unknown quantity c is expressed as a function of a in Equation 3.18, b is related to a from Equation 3.23, and a and b are related to A, B, and C through Equation 3.26. Therefore, working backwards, if we were given f_{PE}, we could determine all the parameters of the perfect ellipsoid. We have one last step; we need to determine the focusing distance of a sphere f_S as a function of the radius. This is a standard expression for incoming plane waves from optics [44]:

$$f_S = \frac{n_2}{n_2 - n_1} R \tag{3.31}$$

which in our case becomes

$$f_S = \frac{1.3375}{.3375} R = 3.\overline{962} R \tag{3.32}$$

and we're done! We now have an expression relating R to f_S, which we set equal to f_{PE} to determine our ellipsoid parameters. This allows us to create a function `PE` for our surface given r_1 as the radius of the sphere, and P_1 as the apex displacement:

$$z(x, y, r_1, P_1) = \texttt{PE}(x, y, r_1, P_1) \tag{3.33}$$

In Section 3.3.3, we utilize different values for r and P to create a model of monocular diplopia. In Chapter 8 we set the value of r_1 to be that of the sphere model we saw

earlier in Section 3.2.1.

3.3 Models of "Problem" Corneas

In this section, we discuss the three models of "problem" corneas: one following PRK surgery, one with the condition of keratoconus, and one with monocular diplopia. We fully parameterize each of these models so that they can simulate a real cornea; we then choose values for the parameters based on the real data from Section 3.4.

3.3.1 PRK

The shape of a PRK cornea is usually characterized by a large central ablation area of low curvature, a ring-shaped transition zone, and the untouched outer cornea. In figure 3.4 we render a 3-D version of a model of a PRK cornea (in white) with a centered ablation zone (in red) and transition zone (in blue).

Since our model is entirely rotationally symmetric and independent of θ, we can describe our surface z_{PRK} as a two-dimensional function of r, then sweep the plane around the z-axis to generate the final surface(s). Any circle (or semi-circle) described by $z = f(r)$ in the 2-D rz plane that is displaced horizontally in r becomes a *torus* when we sweep the plane to generate the function $z = f(r, \theta)$. We will see this when we investigate the surface of the transition zone.

We model the pre-surgical base cornea with a horizontally-centered circle C_b whose radius is r_b, and the $2w$ mm-wide central ablation zone as a smaller horizontally-centered circle C_a whose radius is r_a. The transition zone of width t is slightly more complicated,

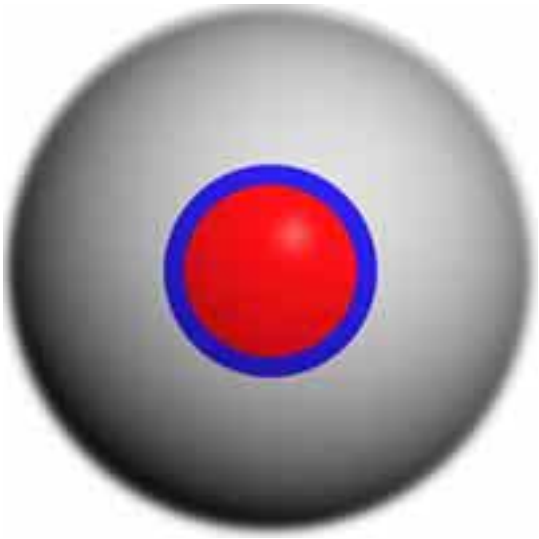

Figure 3.4: A 3-D rendering of our PRK model. The white cornea has a central transition zone (in blue) and an ablation zone (in red).

since we want to ensure smoothness at the joins between the zones. We would like to find a displaced circle C_t which meets with positional and tangent continuity with the other two circles at the joins, which are the two radius values r_{at} and r_{tb} defined as:

$$r_{at} = w \tag{3.34}$$

$$r_{tb} = w + t \tag{3.35}$$

We are given r_a, r_b, w and t and need to find the centers of circles C_a, C_b, C_t and the radius of C_t, r_t. We begin with a technique known as *constraint propagation* [120], in which we propagate our constraints forward, eliminating our unknowns one by one.

During the following explanation, the reader may wish to follow along with Figure 3.5. First, we were given a centered ablation circle C_a (in red) with radius r_a and intersection at the origin. This determines the circle's center, point C_a to be $(0, r_a)$. Circle

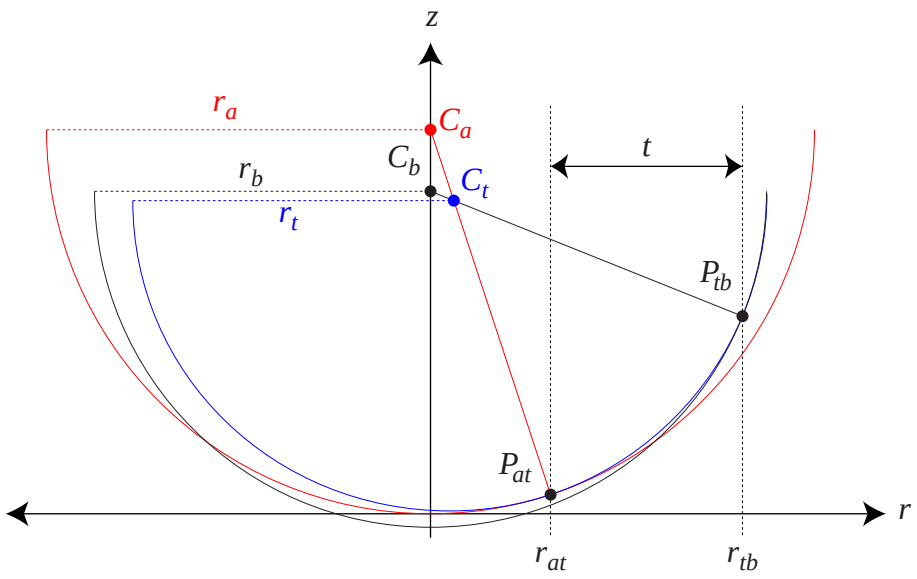

Figure 3.5: A diagram indicating the constraint propagation that takes place as we create our PRK model. We progressively determine C_a, C_t, r_t, and finally C_b.

C_a intersects the line $r = r_{at}$ at P_{at}, creating our first two constraints. We want our transition circle C_t (in blue) to join C_a with positional and tangent continuity. Thus, circle C_t must intersect P_{at}, and its center must lie along the line defined by P_{at} and C_a. We are left with one degree of freedom; we can "grow" C_t from P_{at} toward C_a and still maintain our current constraints. But how much should we grow it?

We bring in the constraint that our base circle C_b (in black) must have radius r_b and must also have its center on the z-axis. C_b will intersect the line $r = r_{tb}$ at P_{tb} with some slope. This is our remaining constraint for C_t; when it intersects $r = r_{tb}$ it must share this slope. So we grow C_t from P_{at} toward C_a until its slope at P_{tb} matches C_b. The intersection now formed with C_t and $r = r_{tb}$ determines point P_{tb}. The last remaining constraint is how high on the z-axis we position C_b. This is easily determined because we know C_b has to intersect P_{tb}.

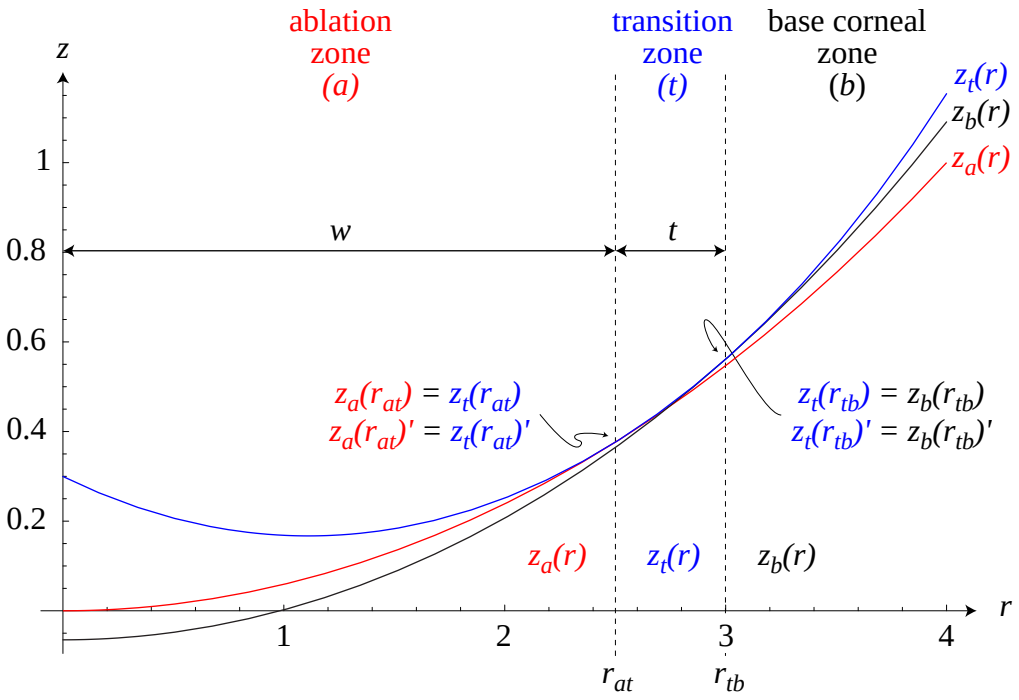

Figure 3.6: A 2-D plot of $z_{PRK}(r)$ through its three helper functions z_a, z_t, and z_b, representing the active surfaces for the ablation zone, transition zone and base corneal zone. The curves are scaled (and, in the case of C_t, de-centered) circles which meet with positional and tangent continuity at the junctions. Our transitions are at $r_{at} = 2.5$ and $r_{tb} = 3$, since we were given $w = 2.5$ and $t = 0.5$.

If we look at our PRK model as a function, we see that we need to define three sub-functions, active during each of the three zones shown in Figure 3.6

$$z_{\text{PRK}}(r,\theta,r_a,r_b,w,t) = \begin{cases} z_a(r,\theta,r_a,r_b,w,t) & r \le r_{at} \\ z_t(r,\theta,r_a,r_b,w,t) & r_{at} < r \le r_{tb} \\ z_b(r,\theta,r_a,r_b,w,t) & r_{tb} < r \end{cases} \tag{3.36}$$

where, as we just explained, each of z_a, z_t and z_b are simply circles with centers at C_a, C_t and C_b and radii r_a, r_t and r_b. Let us rewrite Equation 3.6 as a circle function with parameters of radius r_i and center (C_{ir}, C_{iz}):

$$\texttt{Circle}(r, r_i, C_{ir}, C_{iz}) = C_{iz} - \sqrt{r_i^2 - (r - C_{ir})^2} \tag{3.37}$$

which allows us to finally define z_a, z_t and z_b given that we have found all circle positions and radii as shown earlier:

$$z_a(r,\theta,r_a,r_b,w,t) = \texttt{Circle}(r, r_a, C_{ar}, C_{az}) \tag{3.38}$$

$$z_t(r,\theta,r_a,r_b,w,t) = \texttt{Circle}(r, r_t, C_{tr}, C_{tz}) \tag{3.39}$$

$$z_b(r,\theta,r_a,r_b,w,t) = \texttt{Circle}(r, r_b, C_{br}, C_{bz}) \tag{3.40}$$

To model our real PRK eye from Section 3.4.3, we choose w to be 2.5 mm, the transition zone width t to be 1 mm, the base cornea to have radius $r_b = 7.5$ mm and the ablation zone to have radius $r_a = 9.64$ mm. We center the ablation at $\phi = 5°$ and $\theta = 170°$.

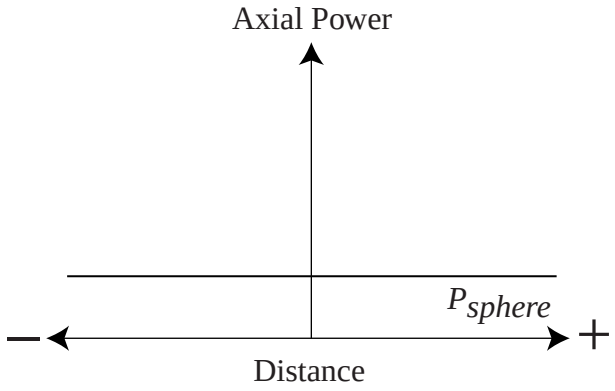

Figure 3.7: This graph illustrates the base corneal model without keratoconus. The model is a simple sphere with constant axial power across its surface. This is represented here as a yellow straight line when plotting axial power vs. distance. The power is denoted P_{sphere} and is labeled on the right.

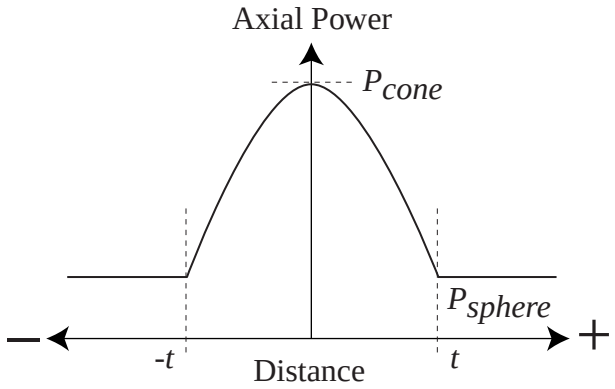

Figure 3.8: To model keratoconus, a section of the sphere is removed and replaced with a surface of revolution formed from a hyperbola. The axial power associated with the hyperbola between $-t$ and t is shown as the central curve. The maximum power of the cone is denoted P_{cone}.

3.3.2 Keratoconus

We use a hyperbolic model of keratoconus [21]. To explain our simulated keratoconic model, we first look at a graph of axial power, as a function of distance, as shown in Figure 3.7. To simulate the cornea, we use a perfect sphere centered at the origin with constant axial power over its surface. This is represented in the graph as a straight line. The power is denoted P_{sphere}. Now, to simulated keratoconus, we represent the "cone" on the cornea by removing a section of the sphere and replacing it with a surface of revolution formed from a hyperbola such that the slope is continuous. Considering this hyperbola between $-t$ and t, its axial power is represented as the curve shown in Figure 3.8. The maximum power of the cone is denoted P_{cone}. The cornea is represented by three free parameters: the power of the sphere (P_{sphere}), the maximum power of the cone (P_{cone}), and the half-width of the cone (t). The eccentricity of the hyperboloid ($e^2 > 1$) can be expressed in terms of these three parameters as:

$$e^2 = \frac{r_{sphere}^2 - r_{cone}^2}{t^2} \tag{3.41}$$

where r_{cone} is the apical radius of curvature of the cone region and r_{sphere} is the radius of curvature of the sphere, related to the paraxial powers P_{cone} and P_{sphere} by:

$$P_{cone} = \frac{n-1}{r_{cone}} \tag{3.42}$$

and

$$P_{sphere} = \frac{n-1}{r_{sphere}} \tag{3.43}$$

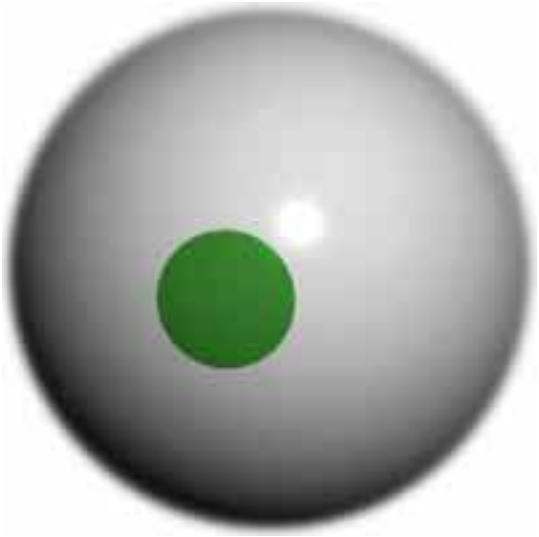

Figure 3.9: A 3-D rendering of the position of the cone (shown in green) on the cornea (in white). The cone is centered at ($\phi = 12°$, $\theta = 215°$), P_{sphere} is 45 D (radius 7.5 mm), P_{cone} is 82 D and t is 2 mm.

where n is the index of refraction, which again is taken to be 1.3375, the effective refractive index of the cornea [49]. In our model, we also allow the cone to be rotated (using spherical coordinates θ and ϕ) to any place on the cornea. This allows us to simulate the keratoconus of a particular patient, in this case the right eye of the patient from Figure 1.1 which we discuss in Section 3.4.4. To model the real cornea from Section 3.4.4, we center the cone at $\phi = 12°$ and $\theta = 215°$, and set P_{sphere} to 45 D (radius 7.5 mm), P_{cone} to 82 D and t to 2 mm as shown in the 3-D rendering from Figure 3.9.

3.3.3 Monocular Diplopia

We use a first-order approximation model of monocular diplopia. We begin with our familiar perfect ellipsoid from Equation 3.33, centrally located, which we denote by the function $\texttt{PE}(x, y, r_1, 0)$. Recall that r_1 specifies the paraxial focusing equivalent of a

sphere with radius r_1. We then add a second perfect ellipsoid, $\texttt{PE}(x, y, r_2, P_2)$, whose origin is shifted over and down in 3D space by P_2. We define our model to be the surface created when we take the lower, or min(), of the two surfaces as in Equation 3.44.

$$z_{MonocularDiplopia}(x, y, r_1, r_2, P_2) = \min(\texttt{PE}(x, y, r_1, 0), \texttt{PE}(x, y, r_2, P_2)) \tag{3.44}$$

The advantage of this model is that the energy distribution on the retina has two discrete peaks, corresponding to the two ellipsoid foci. If r_2 is equal to r_1, and z_2 (the z-component of P_2) is zero, then the contribution onto the retina of PE_2 is a crisp second image, otherwise it is blurred. Typical distances from apex to apex of the two ellipsoids is 10 microns, almost imperceptible to the naked eye. The disadvantage of this model is that the transition between the two ellipsoids involves a very slight discontinuity in slope and curvature, not usually found in corneal data. A second-order approximation model would eliminate the discontinuities with a smooth transition, or *blend* of the two surfaces using a spline.

To model our real monocular diplopia from Section 3.4.5, we choose r_2 to be equal to $r_1 \approx 7.55$ mm, and P_2 to be $(0, 0.2, 0.01425)$. This results in a secondary focus which is 0.2 mm *below* the primary on the retina, and had the same peak-to-peak ratio of 28.7%.

3.4 Real Corneal Data

We have included five examples from the wide variety of corneas that clinicians encounter: a "normal" cornea (free from astigmatism, surgery and defects), one with astigmatism, one with keratoconus, one with monocular diplopia, and one that has undergone

PRK. We discuss the details of each of these corneas in the following sections.

3.4.1 "Normal" Cornea

We chose to include a healthy "normal" cornea to act as a reference; one that was free from astigmatism, major aberrations, and the scarring that usually follows corneal surgeries. As such, it is relatively rotationally symmetric and smooth across the entire surface. It has an apical mean curvature of 43.5 D, and flattens in the periphery.

3.4.2 Astigmatism

There are usually two parameters describing the asymmetry associated with astigmatism, magnitude and angle. Most astigmatism is "with-the-rule", which means that it is more curved vertically than horizontally. This particular eye belongs to our colleague Dr. Mandell, and contains a mild degree (approximately 1.5 D) of with-the-rule astigmatism. That is, its curvature is 44 D vertically and 42.5 D horizontally.

3.4.3 PRK

This particular subject was drawn from patients in the phase III FDA trials of the Nidek excimer laser system [30]. The data was taken from a corneal topography scan 9 months after surgery. The ablation is a bit off-axis, centered at $\phi = 5^\circ$ and $\theta = 170^\circ$. The base cornea has a radius of 7.5 mm and the ablation zone has a radius of 9.64 mm. We estimate the ablation diameter to be approximately 5 mm.

3.4.4 Keratoconus

This famous eye (shown photographed in Figure 1.2) has been used in our research on effective visualization of keratoconus [4, 5]. The thin, problem corneal region, or "cone," bulges significantly for this patient. It is located in the lower right (lower left from our viewpoint), at approximately $\phi = 12^\circ$ and $\theta = 215^\circ$ in spherical coordinates. There is much higher curvature (over 80 D!) in that region than in the other areas, as we shall see.

3.4.5 Monocular Diplopia

This patient's cornea has a flat region of good focus in its center and another in the upper region. There is slight corneal warpage between these two areas, causing both to form quite distinct foci on the retina, causing the monocular diplopia. The second focus is approximately 0.2 mm (200 μm) below the main focus on the retina and subjectively measured as 0.45° above the main focus of her right eye [108].

Chapter 4

Visual Acuity Prediction

> I have bad eyesight and I'm sensitive about it. When I take an eye test, the optometrist points to the letters and *he* calls them out...
> He says "True" or "False".
> — *Woody Allen, "The Nightclub Years" album*

4.1 Introduction

Corneal Topographers (CTs) use the pattern from reflected rings to reconstruct an internal model of the cornea to compute and display refractive power for the clinician [9, 64, 65, 79, 114, 118]. Many now offer "acuity indices" based on overall corneal smoothness to analyze predicted visual acuity. We find the vision of post-refractive surgery patients to be poorly predicted by these indices. Our goal is to create a new acuity index that would be a better predictor for these patients.

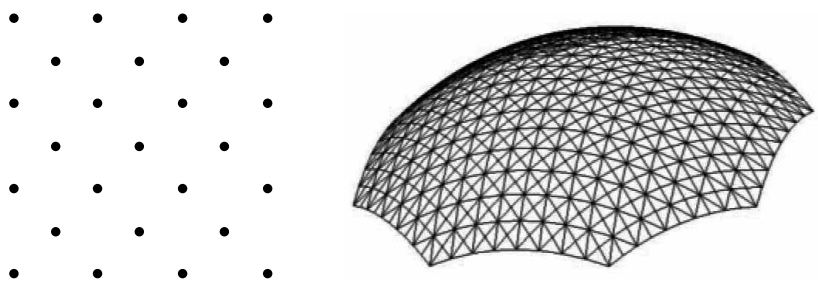

Figure 4.1: The crosshatched sampling technique on the left was used to query the geometry information from our reconstructed corneal models. The cornea on the right is shown sampled by this method to form a triangular mesh.

4.2 Methods

We created a new metric for visual acuity based on the ability of a cornea to focus light coherently to a single point. To analyze real patient data, we recovered the raw ring data from the CT and then reconstructed the cornea as a mathematical curved surface [20] in a method similar to the one used in our earlier work [41, 42, 43]. The continuous nature of the surface allowed for arbitrary sampling to query both the position and derivative information that is necessary for our calculation. We showered each cornea with approximately 2,800 light rays, in a 2 mm radius arranged in a crosshatched pattern, as illustrated by Figure 4.1 below.

Once we had the mathematical machinery in place to analyze an arbitrary recovered corneal surface, all that was needed was to run actual corneal patient data through our system. We used the data from 62 post-refractive surgical corneas and determined the correlation of our acuity index with three measurements of the patient's visual acuity. Then, using the same data, we compared our correlation with that of other popular indices. Finally, we removed two corneas from the sample and analyzed how the fittings changed.

4.2.1 Measurements from Post-PRK and Post-PARK Eyes

The subjects for this study were drawn from patients in the phase III FDA trials of the Nidek excimer laser system. All procedures were performed by one of three refractive surgeons at the Beckman Vision Center, Refractive Surgery Service in the Ophthalmology department of the University of California, San Francisco. The ablation zone diameter of the Nidek laser is 7 millimeters. Photorefractive keratectomy (PRK) involves a single spherical ablation of the anterior cornea. Photorefractive astigmatic keratectomy (PARK) involves a spherical ablation followed by an elliptical ablation to correct for astigmatism [33, 73]. The mean correction for the PRK eyes (n = 31) was -7.5 diopters of myopia and for the PARK eyes (n = 31) was -5.8 diopters. The PRK patients were 41 $\pm$ 10 years old and the PARK patients were 48 $\pm$ 10 years old. Only the latest examination (six or more months postoperative) was used in this study since prior studies have shown that corneal clarity and shape stabilize by this time [32, 46]. The test battery included best spectacle-corrected high contrast visual acuity (HCVA) and small letter contrast sensitivity under standard (SLCT-L) and low luminance (SLCT-D) conditions [91]. The corneal topography was performed using the ©TMS-2 corneal topography instrument [13], and one colleague completed all visual and topography measurements.

4.2.2 Wavefront Coherence Area

The idea behind the wavefront coherence area metric is to measure the fraction of the cornea's area inside a specified pupil diameter that is able to focus light coherently onto the retina of the eye. Our model of the cornea is the same one used in our earlier

work [29]; we again ignore the contribution of the lens and consider the cornea to be a uniform material with an effective index of refraction (n) of 1.3375.

We begin by treating every point on the cornea as a reference corneal point. Next, we determine where the light for that point will focus using Snell's law and Coddington's equations [70, 100]. However, instead of calculating the focus from the mean of the principle refractive curvatures as we did in our earlier work [29], here we use the maximum. We will discuss the rationale in the next section when we describe the cylinder correction. From that focus, we first calculate the reference optical path length (OPLref) through the reference corneal point to a reference plane. The focus is then used to originate a wavefront that we refract back through the cornea and out to a reference plane. We measure the percentage of the wavefront that passes through the cornea and the 4 mm diameter pupil whose optical path length (OPL) is within a quarter wavelength of yellow-green light (550 nm) of the reference OPL. The process is graphically shown in Figure 4.2. We also include the pseudo-code that implements the calculation of the wavefront coherence area below:

```
CalculateMaximumWavefrontCoherence(cornea, pupil_diameter, reference_plane)
Set theMaximumCoherence = -1
For every (corneal) point P in the pupil_diameter on the cornea:
  Find the focus F for incoming parallel bundle of rays passing through P
  Set OPLref = OPL from the focus F to the point P to the reference_plane
  Set theCoherenceForPointQ = 0
  For every (wavefront) point Q in the pupil_diameter on the cornea:
    Set OPLQ = OPL from the focus F to the point Q to the reference_plane
    If OPLQ is within a quarter wavelength of OPLref
       Increase theCoherenceForPointQ by Q's representative area
  If theCoherenceForPointQ is greater than theMaximumCoherence, replace it
Return(theMaximumCoherence)
```

The optical path length is calculated simply by determining the amount of time it would have taken light to travel from the focus to the cornea, through our cylinder

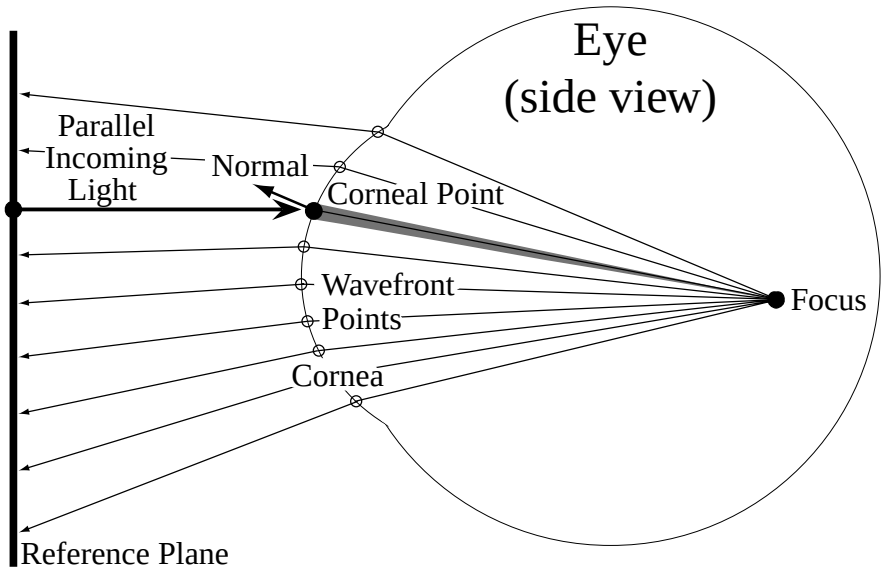

Figure 4.2: A simple model of a side view of the eye and the technique used for finding the wavefront coherence area.

corrective lens and to a plane. More specifically, the OPL is the sum of three terms as shown in equation 4.1 below. The first is the distance, D_{3d}, from the focus to the wavefront point weighted by the index of refraction of the cornea. The second is the refractive cylinder correction, RCC, determined from the corneal point and the wavefront point. The third term is the distance, D_{RP}, along the refracted exit ray (from the cornea) to the reference plane, which is located at z = 3 mm, at the entrance pupil plane. If the ray is directed away from the plane, as it will be for most points that we consider, this terms contribution is negative. However, for the sake of simplicity, Figure 4.2 shows all rays directed towards the plane which we have located outside the cornea at a position of approximately z = -15 mm.

$$OPL = 1.3375\ D_{3d} + RCC + D_{RP} \tag{4.1}$$

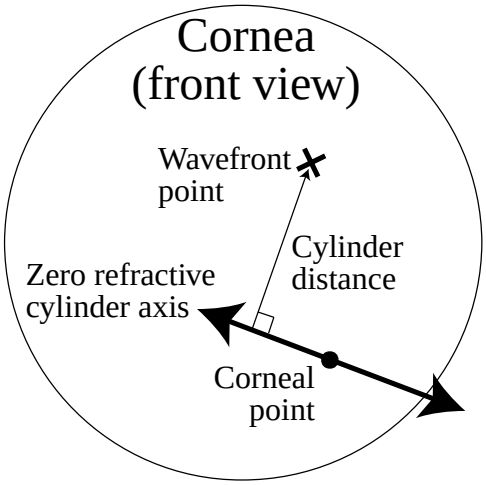

Figure 4.3: A simple model of the front view of the cornea highlighting the method used to calculate the cylinder distance.

4.2.3 OPL Refractive Cylinder Correction

The second term in the OPL calculation is based on our need to compensate for the dominant refractive cylinder present for most corneal points. Recall that we chose the maximum refractive curvature when determining our focus. That means the bundle of rays around the corneal point in the maximum refractive curvature direction will have very similar OPLs as the reference. We define the "zero refractive cylinder axis" to be the maximum curvature direction; wavefront points along this line will not need any OPL correction. However, due to the non-zero refractive cylinder at the corneal point, wavefront points that are away from the zero refractive cylinder axis will have different OPLs from the reference. We define another term, the "cylinder distance", to be the perpendicular distance from the wavefront point to the zero refractive cylinder axis as shown below in Figure 4.3.

The refractive cylinder correction, RCC, is the product of the square of the cylin-

der distance and half of the refractive cylinder at the corneal point as shown in equation 4.2 below. This simulates the amount of time a ray would take to travel through a thin cylinder corrective lens with corrective power equal to the refractive cylinder.

$$RCC = \frac{Cylinder\_Distance^2 * Refractive\_Cylinder\_At\_Corneal\_Point}{2} \tag{4.2}$$

4.2.4 Other Visual Acuity Metrics

We compared our wavefront coherence area (denoted CA) with three popular metrics taken from the ©TMS-2 corneal topography instrument: the surface regularity index (SRI), the surface asymmetry index (SAI) and the coefficient of variation of corneal power (CVP) [23, 119]. The explanations below are taken directly from the ©TMS-2 itself:

> **Surface Regularity Index.** The SRI is a correlate to potential visual acuity and is a measure of local fluctuations in central corneal power. When SRI is elevated, the corneal surface ahead of the entrance pupil will be irregular, leading to a reduction in best spectacle-corrected visual acuity. High SRI values are found with dry eyes, contact lens wear, trauma, and penetrating keratoplasty.
>
> **Surface Asymmetry Index.** The SAI measures the difference in corneal powers at every ring (180 degrees apart) over the entire corneal surface. The SAI is often higher than normal in keratoconus, penetrating keratoplasty, de-centered myopic refractive surgical procedures, trauma, and contact lens warpage. Adequate spectacle correction is often not achieved when SAI is high.
>
> **Coefficient of Variation of corneal Power.** The CVP is calculated from the Standard Deviation of corneal Powers (SDP) divided by the grand average of corneal powers. This fundamental statistic is high when there is a broad range of powers in the corneal surface and has been found to be a good measure of corneal varifocality. High values of CVP are found in moderate to severe keratoconus corneas as well as corneal transplants in the early post-operative period. Manifest refraction of an eye with high CVP will be difficult to achieve, but attention to refraction is important in such a patient to attain spectacle tolerance. The CVP value given has been scaled up by a factor of 1000.

4.3 Results

We charted the correlation of our metric and the other acuity predictors against the actual acuity measurements. We found that none of the predicted indices was able to provide R^2 values much above 0.25, which is what we expected. It is well known that it is difficult to predict the vision of post-refractive surgical corneas. In that context, our predicted acuity metric had the best correlation values for both low contrast (SLCT-L) and low luminance (SLCT-D) vision. It shared the best correlation value with the SAI index for low contrast acuity prediction, but it was the only one that could predict low luminance. HCVA remained poorly predicted by all indices, with correlation values near zero on every chart. The scatter plots for the four acuity predictors are shown in Figure 4.4, and the correlation summary is in Figure 4.5.

4.3.1 Analysis of the Data Fit

Close analysis of the scatter plots of Figure 4.4 reveals two patients who have extremely poor low contrast acuity, as measured by the SLCT-L test. These corneas exhibit two of the most de-centered ablations of the group. All of the acuity metrics accurately predict that they would have vision far below average, but it is interesting to examine what would happen to the fit of the regression lines if the data from these two corneas were removed from the sample. We would like to know how much of the correlation is based on these two data points. When these data points are removed, our CA metric is virtually unchanged, as are many of the others. The correlation that changes the most is the SAI vs. SLCT-L comparison. This is especially curious since it was the only correlation whose

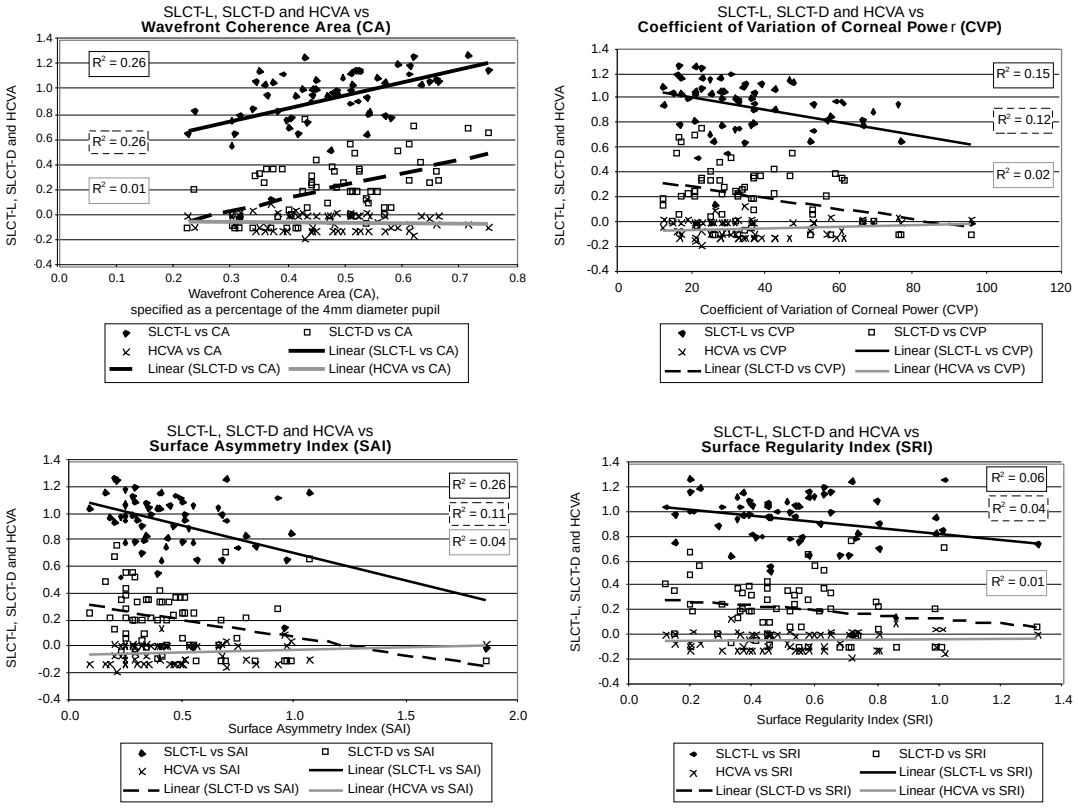

Figure 4.4: Scatter plots of CA, CVP, SAI and SRI versus the three actual acuity indices, SLCT-L, SLCT-D and HCVA.

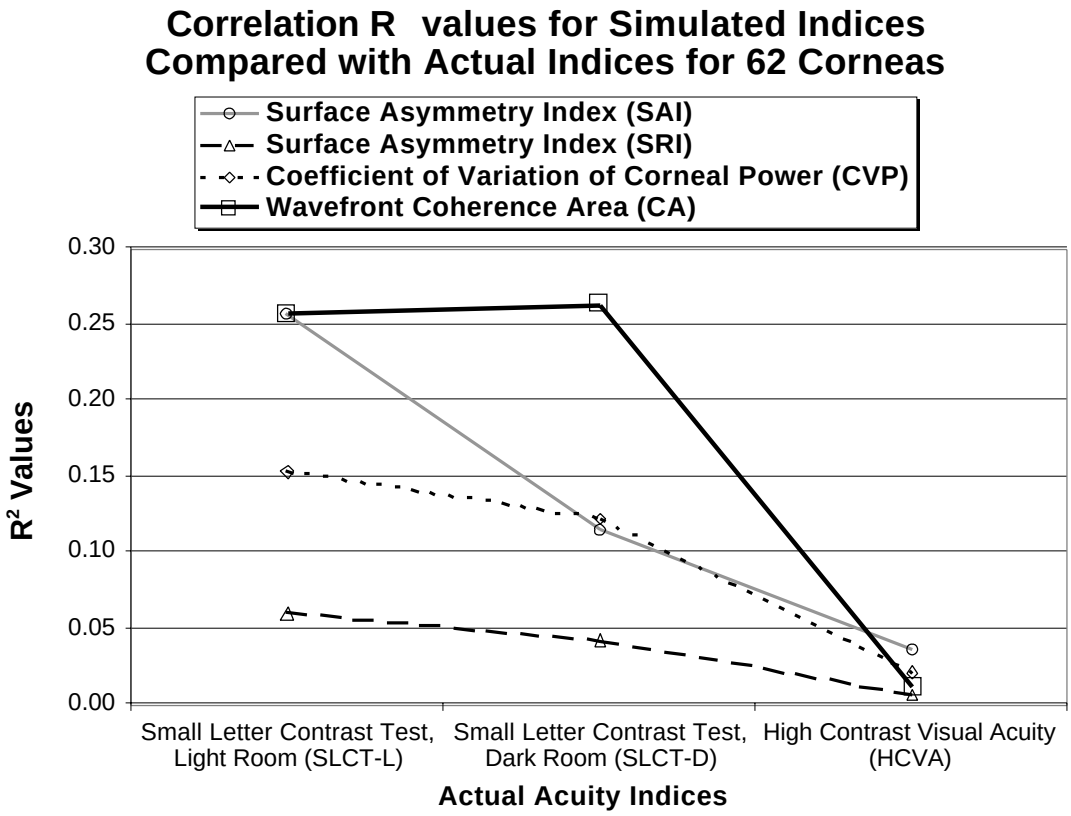

Figure 4.5: Comparison of correlation R^2 values for the four visual acuity predictors.

R^2 value was even remotely close to ours with all 62 eyes. Figure 4.6 shows the comparison of the SAI vs. SLCT-L metric before and after removing the two eyes from the sample set. Note that the R^2 value drops from 0.26 to 0.03. This highlights how unstable R^2 is for comparing correlation as well as how dependent the SAI metric was on the two poor corneas for achieving its good fit.

Finally, Figure 4.7 shows the new correlation comparison after removing the two poor corneas from the sample, leaving 60 eyes. Note that with this data, the correlation values for wavefront coherence area remain virtually unchanged and it is now the best predictor of visual acuity for both low contrast and low luminance.

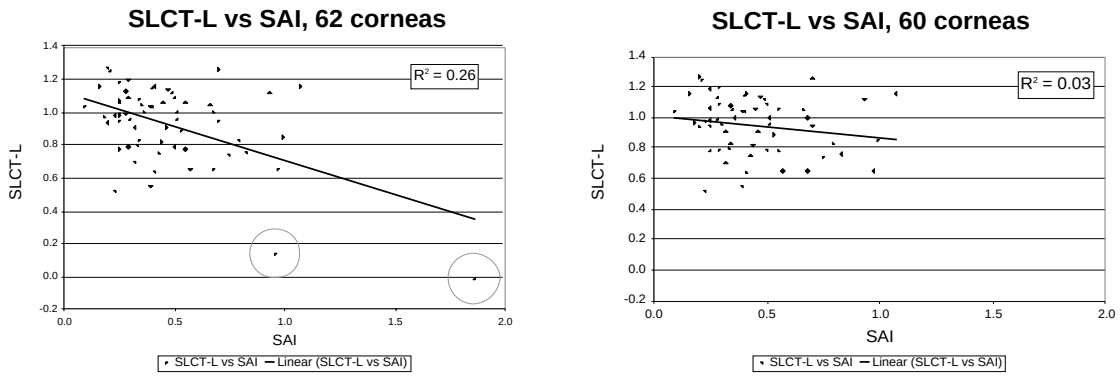

Figure 4.6: Predictor SAI versus measured low contrast SLCT-L before and after removing the two circled poor performing eyes.

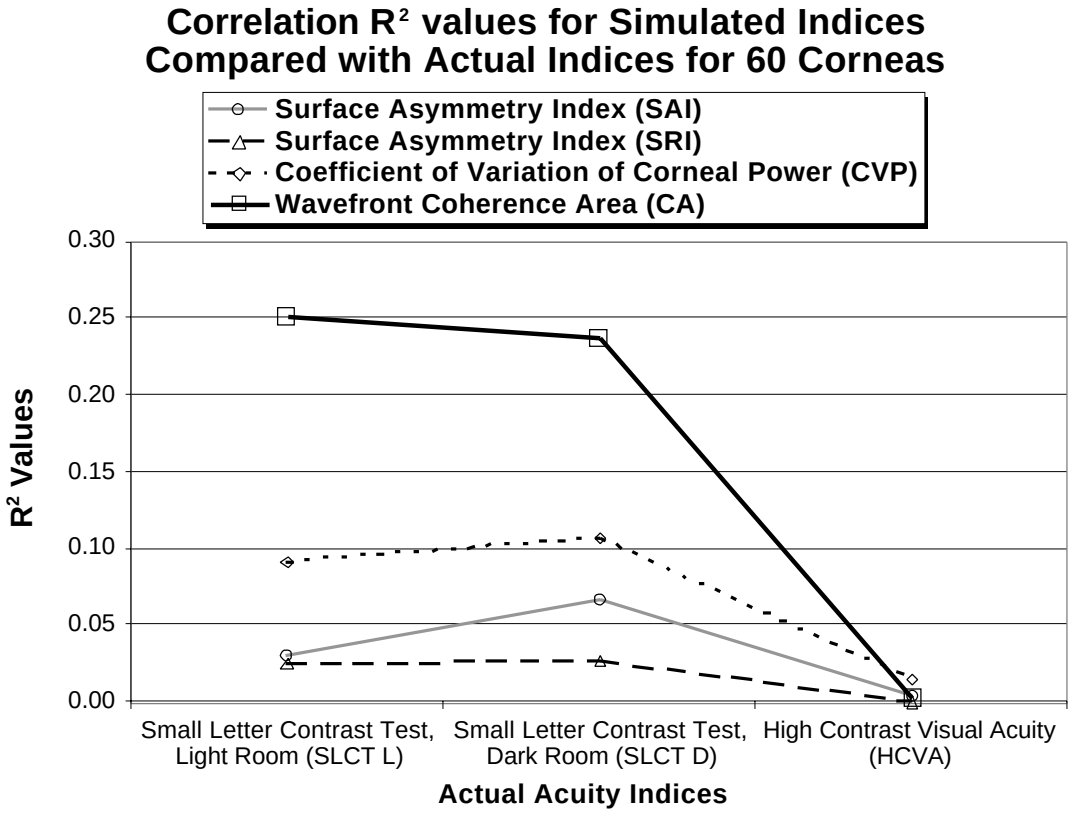

Figure 4.7: The correlation comparison after removing two patients' corneas from the sample.

4.4 Conclusion

We presented a metric for simulating visual acuity based on wave and ray optics called the wavefront coherence area. We evaluated 62 post-PRK and post-PARK corneas and found that our index predicted the low contrast and low luminance acuity for these corneas better than the three popular metrics SAI, SRI and CVP. However, high contrast visual acuity was poorly predicted by all the metrics. Removal of two corneas with extremely de-centered ablations from the sample resulted in a significant decrease in the correlation of the SAI index, with the others remaining relatively constant.

In summary, our representation has considerable advantages, as it more accurately reflects what contributes to visual acuity — the ability of a region of the cornea to focus light coherently onto the retina of the eye.

Chapter 5

Corneal Representations of Refractive Power

> The principal objective of visualization in scientific computing is to develop techniques that make perceptible the most important informational aspects of a data set.
> — *Robert S. Wolff and Larry Yeager [121]*

5.1 Introduction

Our goal is to convey to clinicians the visual acuity of the cornea using several techniques based on fundamentals of geometric optics. The scientific visualizations we propose can be clustered into two classes: corneal representations and retinal representations; however, in this chapter, we focus our discussion on corneal representations. It is important to note that, for each method listed below, we can illustrate the visual acuity with or without spectacle correction. Corneal representations are meant to reveal how well the cornea focuses parallel light onto the fovea of the eye by providing a pseudo-colored display

of various error metrics. For each error metric, we show both real and simulated data, and illustrate how each representation contributes to the simulation of corneal visual acuity.

5.2 Methods

We classify the corneal representations into two categories, refractive power visualizations based on paraxial focus and wavefront visualizations. We'll begin with a discussion of refractive power maps.

We propose four metrics to simulate the corneal contribution to visual acuity. Figure 5.1 illustrates how we compute the values that we use in our calculations. As explained in Section 3.1, our corneal model is a very simple one since we ignore the contribution of the lens and consider the entire cornea to be a uniform material with a constant index of refraction (n) of 1.3375. It is important to note that the metrics we propose here are independent of our implementation. If we were to improve the quality of the model, the metrics themselves would remain unchanged.

We begin the computation at the central axial point on the cornea. We refract incoming parallel light and calculate where it converges to a focus using Coddington's equations [70, 100]. Fortunately, due to constraints in our representation, the normal at the central point is parallel to the incoming parallel light; thus, according to Snell's law, the refracted light will also be in this same direction. If the central axial point has some astigmatism, or cylinder, then so will the refracted wavefront and there will be two principal curvatures. We define the paraxial focal point (PFP) to be the focus as determined by the average of these curvatures (also known as "mean sphere"). The CT axis, which is the

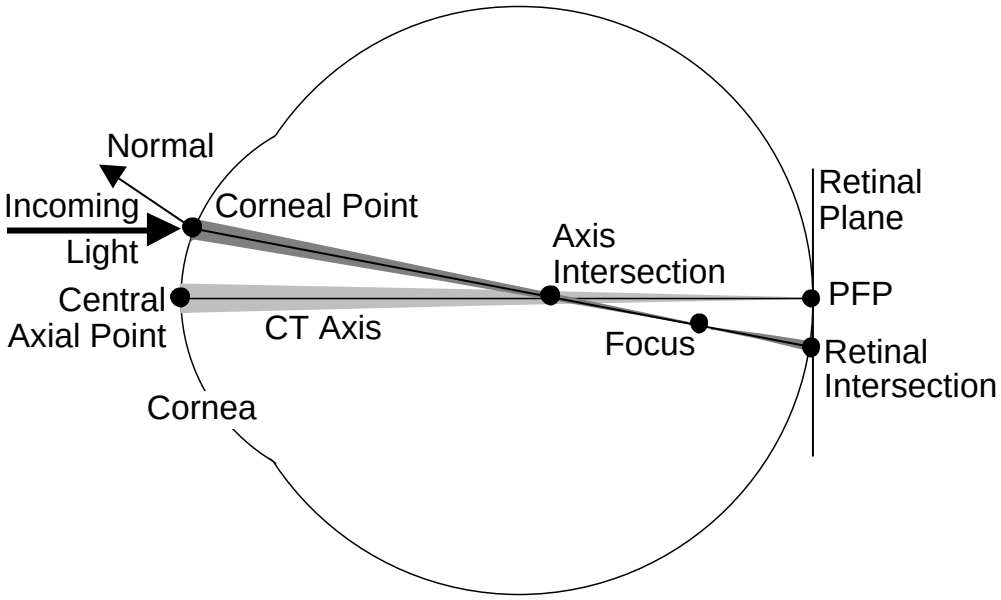

Figure 5.1: A simple model of the cornea, eye, and the refraction of a ray of incoming light.

z-axis, is the line from the central axial point to the PFP. The retinal plane is the plane that passes through the PFP and is normal to the CT axis.

Then, for each corneal point of interest, we refract parallel incoming light according to Snell's law and Coddington's equations and we calculate where that light focuses. Again, if there is any cylinder in the refracted wavefront, then there will be two principal curvatures; in that case, we use their average to determine the focus. The retinal intersection is the location where the refracted ray intersects the retinal plane. If the normal lies in the meridional plane[1] , then the axis intersection is the intersection of the refracted ray with the CT axis; otherwise, the refracted ray will not intersect the CT axis. In that case, we choose the axis intersection to be the point of closest approach to the central axis along the refracted ray. At the central axial point there are infinitely many such intersections; thus, for that corneal point, we set the axis intersection to be the PFP.

[1]We define the meridional plane to be the plane containing the CT Axis and the corneal point.

It is important to note that if the pupil is de-centered, our PFP may not be the optimal PFP. For refractive purposes, most people advocate using the line of sight (LOS) rather than the CT axis.

For each acuity metric, we determine the minimum and maximum values over all the points on the cornea, define a colormap to span those values, and index into that colormap to pseudo-color the surface of the cornea. Often we have found it effective to quantize the color map so that contours and contour lines can be more easily identified.

5.2.1 Paraxial Focus vs. "Best" Focus

All of the refractive power displays we describe in the following sections are based on the paraxial focus, the PFP. However, this may not be the most optimal focus for the entire eye. If we were to find this "best" focus, it would depend on how large our pupil is, and thus what range of corneal data we consider. As the pupil approached a pinhole, our best focus would approach the paraxial focus. However, with peripheral spherical aberration, the best focus may move closer to the cornea.

The following four visualizations could also be calculated by replacing the PFP with a computed overall optimal focus. We discuss the process of determining the best focus in Section 6.2.1. We'll utilize this best focus when we discuss our wavefront representations in Section 5.2.6.

5.2.2 Axial Refractive Power

We define axial refractive power at a corneal point to be the quotient of index of refraction of the cornea model divided by the distance from the corneal point to the axis

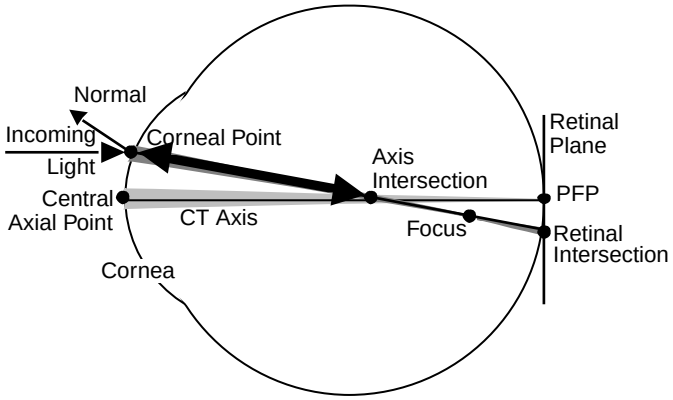

Figure 5.2: Axial refractive power is a function of the distance between the corneal point and the axis intersection.

intersection. This map often has a characteristic "figure-8" or "crescent" shape. Clinicians are familiar with this representation because it is similar to the standard axial curvature maps used in most corneal topography instruments. The figure-8 indicates the amount and orientation of astigmatism.

$$Axial\_Refractive\_Power = \frac{n}{\texttt{Distance3D}(Corneal\_Point, Axis\_Intersection)} \tag{5.1}$$

where

$$\texttt{Distance3D}(P_0, P_1) = \sqrt{(P_{1x} - P_{0x})^2 + (P_{1y} - P_{0y})^2 + (P_{1z} - P_{0z})^2} \tag{5.2}$$

This definition differs from the traditional axial curvature map [63, 82, 93] in that this refractive power map takes into account the refraction of an incoming parallel ray, whereas the standard map is purely a surface shape quantity. For example, the standard axial curvature of a sphere is constant over its surface, whereas the axial refractive power increases as we move away from the center. Figure 5.3 illustrates a direct comparison

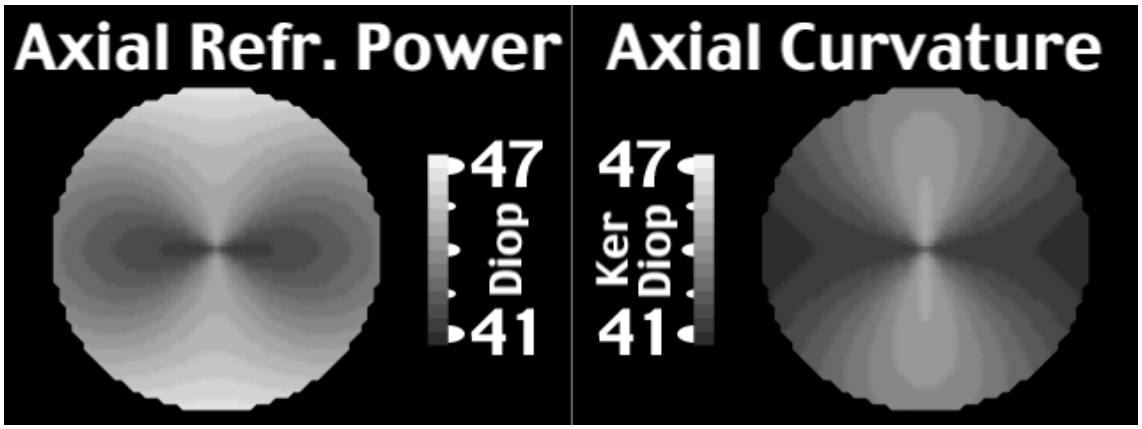

Figure 5.3: A comparison between axial refractive power and axial curvature.

of these two quantities on a simulated cornea having with-the-rule astigmatism. Note that even though there is a difference in the orientation of the figure-8 pattern, they are identical in the central region near the CT axis. This is similar to the results of [95].

5.2.3 Instantaneous Mean Refractive Power

We define instantaneous mean refractive power at a corneal point to be the quotient of index of refraction of our cornea model divided by the focal distance of the cornea at that point, which is the distance from the corneal point to the focus. This is the only one of our four metrics that is not a function of the central axis or of the PFP; rather, it is purely a measure of the surface's refracting power. The advantage of this definition over other curvature representations is that this metric includes the effects of spherical aberration. Those other metrics would be constant for a sphere, whereas instantaneous refractive power increases away from the center.

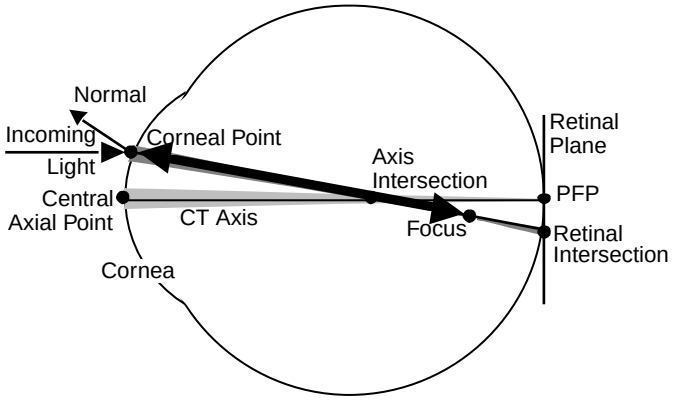

Figure 5.4: Instantaneous mean refractive power is a function of the distance between the corneal point and the focus.

$$Instantaneous\_Mean\_Refractive\_Power = \frac{n}{\texttt{Distance3D}(Corneal\_Point, Focus)} \quad (5.3)$$

5.2.4 Retinal Distance

We define the retinal distance, for each corneal point, to be the distance from the PFP to the retinal intersection, that is, to the point of intersection of the refracted ray with the retinal plane. Since the retinal plane was defined to contain the PFP, both the retinal intersection and the PFP lie in that plane; thus, the distance calculation is a two-dimensional planar distance measure. For a perfect eye, parallel light would converge to a point focus at the PFP and thus, in this case, the retinal distance at every corneal point would be zero. This metric provides an estimate of lateral spherical aberration.

$$Retinal\_Distance = \texttt{Distance2D}(Retinal\_Intersection, PFP) \quad (5.4)$$

where

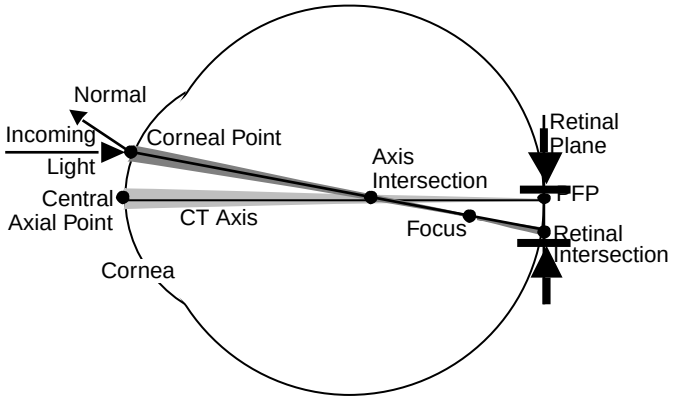

Figure 5.5: Retinal distance is the distance between the retinal intersection and the PFP.

$$\texttt{Distance2D}(P_0, P_1) = \sqrt{(P_{1x} - P_{0x})^2 + (P_{1y} - P_{0y})^2} \tag{5.5}$$

As mentioned earlier, instead of basing distance calculations on our PFP, we could base them on the best focus as determined by all the rays incident on the eye. This is exactly what we do in Section 6.2.3 when we introduce the *Corneal PSF*, simply a shape display with an overlay of retinal distance (to the best focus) contour lines. We defer the explanation of this visualization until we discuss the calculation of the best focus.

5.2.5 Focusing Distance

We define focusing distance, for each corneal point, to be the distance from the focal point of the refracted ray to the PFP. For a perfect eye, the rays of incoming parallel light would converge to a point focus at the PFP and thus the focusing distance for every corneal point would be zero in this case. We will find that focusing distance produces visualizations very similar to instantaneous mean refractive power.

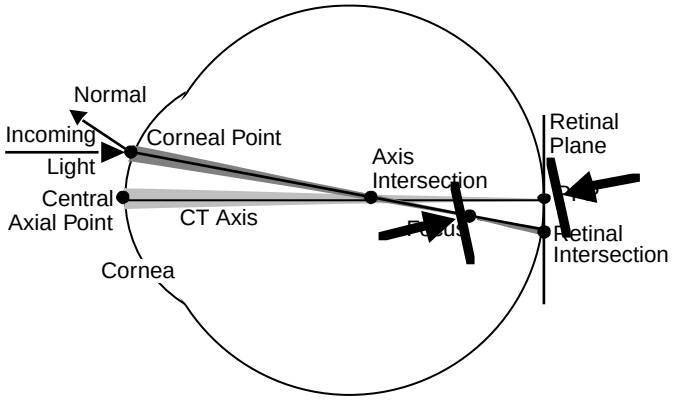

Figure 5.6: Focusing distance is the distance between the focus and the PFP.

$$Focusing\_Distance = \texttt{Distance3D}(Focus, PFP) \tag{5.6}$$

5.2.6 Wavefront Representations

As discussed in Section 5.2.1, let us assume we have at our disposal a point representing the "best" focus for a particular eye. We could imagine this point as a light source and begin emanating a wavefront, just as we did in Chapter 4. We then calculate parameters describing its deviation from ideal after it passes through our refractive surfaces, as shown in Figure 5.7. These techniques are similar to those presented in [61].

We would like to calculate the wavefront in *object* space, as seen from the outside. This has become the standard method for representing refractive properties of the eye. We begin by determining the reference optical path length, OPL_{ref}. This is the sum of three factors: the time spent in the cornea, the time spent in air until it hits the entrance pupil at $z = 3$ mm, and a phase term to account for our cylinder correction.

As we showed in Sections 2.2.3 and 4.2.2, each term is simply the product of the

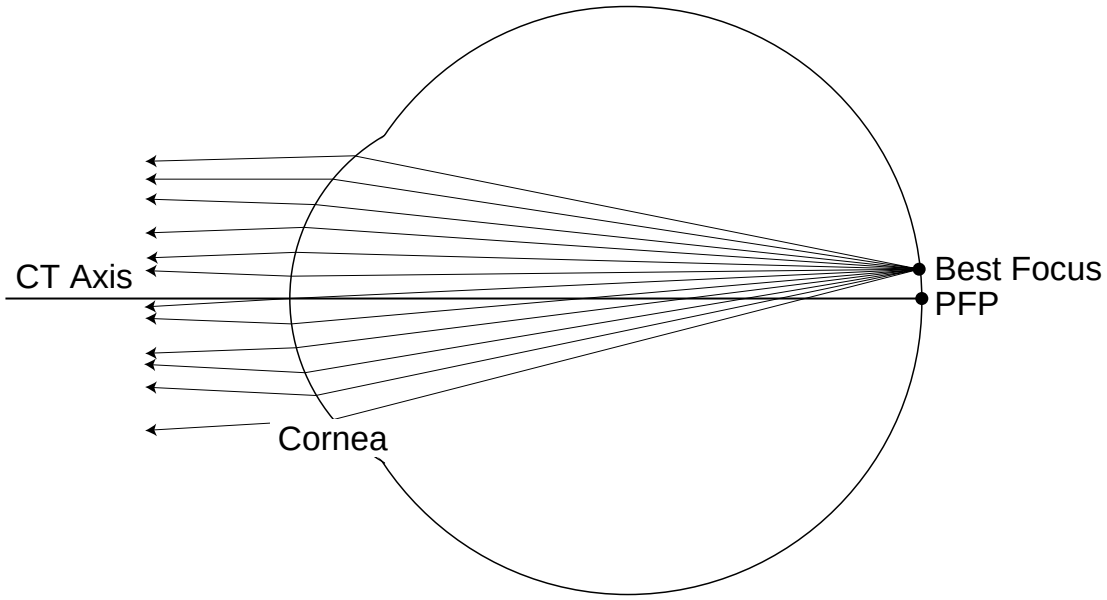

Figure 5.7: We begin our wavefront calculation at our best focus (which may be distinct from the PFP), then send out rays of light to the cornea, and refract them into air. They may not all be parallel.

distance traveled in a media and the index of refraction of the media. We also saw the phase compensation term in Equation 4.2. What differs here is that the time spent outside the cornea is a negative value, since we want to know how long it took until the ray hit the pupil plane which is behind the ray. We compensate for any astigmatism with a corrective cylinder lens; we leave the explanation of this to Section 6.2.1. This is not local refractive cylinder as in Section 4.2.2, it is the overall cylinder we had to apply to get the best focus.

Once we have OPL_{ref}, we know how long we can let our wavefront propagate. For a particular point P on the cornea, we follow the ray for the same time as the reference ray. This involves tracing the ray to the cornea, refracting it into air, correcting for any cylinder, and following that refracted ray until our "time" equals that of the reference ray. As we just mentioned, this means we follow the normal backwards as shown by the dotted

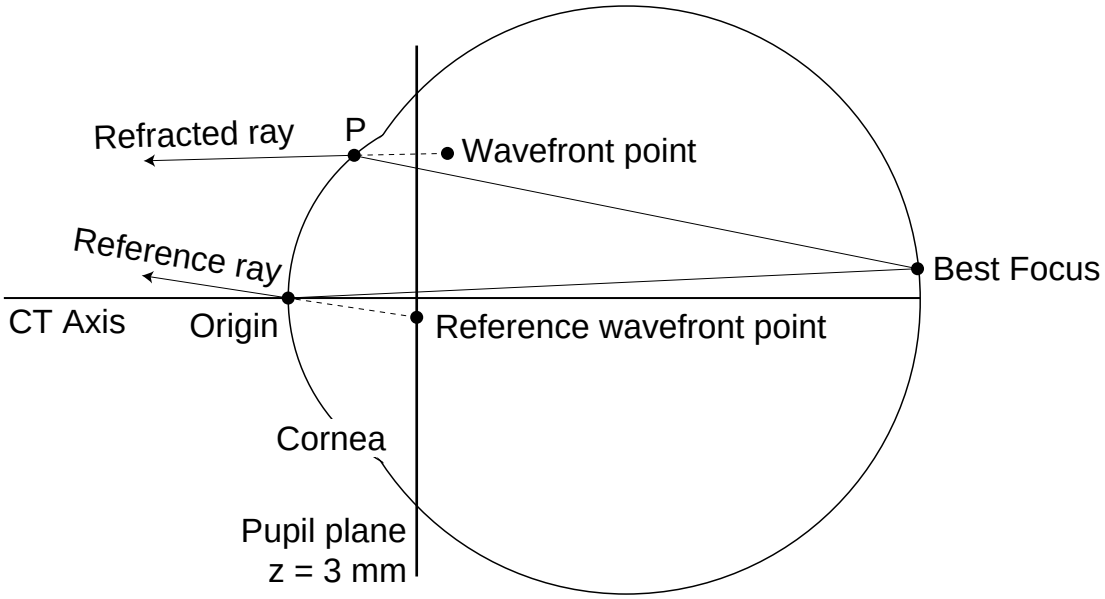

Figure 5.8: We calculate the position of the wavefront by first determining the reference optical path length (OPL_{ref}). This is the sum of the time spent in the cornea, the time spent in air until it hits the entrance pupil at $z = 3$ mm, and a phase term to account for our cylinder correction. For a particular point P on the cornea, we follow the ray for the same time as the reference ray. This involves tracing the ray to the cornea, refracting it into air, and following that refracted ray until our "time" equals that of the reference ray. This means we follow the normal backwards as shown by the dotted line, until we hit our wavefront point.

line in Figure 5.8, until we hit our wavefront point.

If we do this for densely sampled points P on the cornea, we can generate a full cloud of wavefront points. We then fit a surface to this and query curvature information. We now discuss several parameters we can visualize based on these computations.

Wave Angle

For every uniformly sampled point P on the cornea, we calculate the angular difference (measured in minutes) from the refracted ray to the z-axis.

Wave Height

For every uniformly sampled point P on the cornea, we calculate the z-value of the corresponding wavefront point. It is important to note that if the wave angle is non-zero, the (x, y) location of the point P may not correspond to the (x, y) location of the wavefront point.

Wavefront curvatures

Once we have the wavefront as a surface, we can display standard (axial, instantaneous, minimum, maximum, mean sphere) curvature representations just as if it were a corneal surface. The difference is we do not compensate with the 337.5 term as in Section 2.1.2, since this is the curvature of the wavefront, not of the cornea.

5.3 Results

We display our four paraxial refractive power visualization metrics on two sets of data, a simulated cornea and a real cornea. The four metrics each contribute some information to the clinician about the projected visual acuity, as we will see. In addition, Section 8.4.1 contains visualizations and analysis of all of the corneal data from Chapter 3 for our wavefront visualizations.

5.3.1 Simulated Data

We use a simple asymmetric ellipsoid to simulate a cornea that has with-the-rule astigmatism. The equation for the ellipsoid is

$$\left(\frac{x}{A}\right)^2 + \left(\frac{y}{B}\right)^2 + \left(\frac{C-z}{C}\right)^2 = 1 \tag{5.7}$$

with $A = 8.7$, $B = 9$ and $C = 10$. This results in principal curvatures $\frac{337.5}{7.569} \approx 44.6$ D in the x-direction and $\frac{337.5}{8.1} = 41\frac{2}{3}$ D in the y-direction. This shape is rendered in three dimensions below in Figure 5.9. The intensity of every point in this image is a linear function of the z value of the data; the lighter data points are closer to the $z = 0$ plane. We define the range of the data to be x, y = [-3,3][-3,3].

The most striking metric is axial refractive power. It highlights the inherent astigmatism associated with this asymmetric model. We can easily measure that there are four diopters of cylinder and the model is exactly against-the-rule. Retinal distance demonstrates that the left and right areas contribute to focus slightly better than the top and bottom regions, with a good focus in the central circle. Instantaneous refractive power and

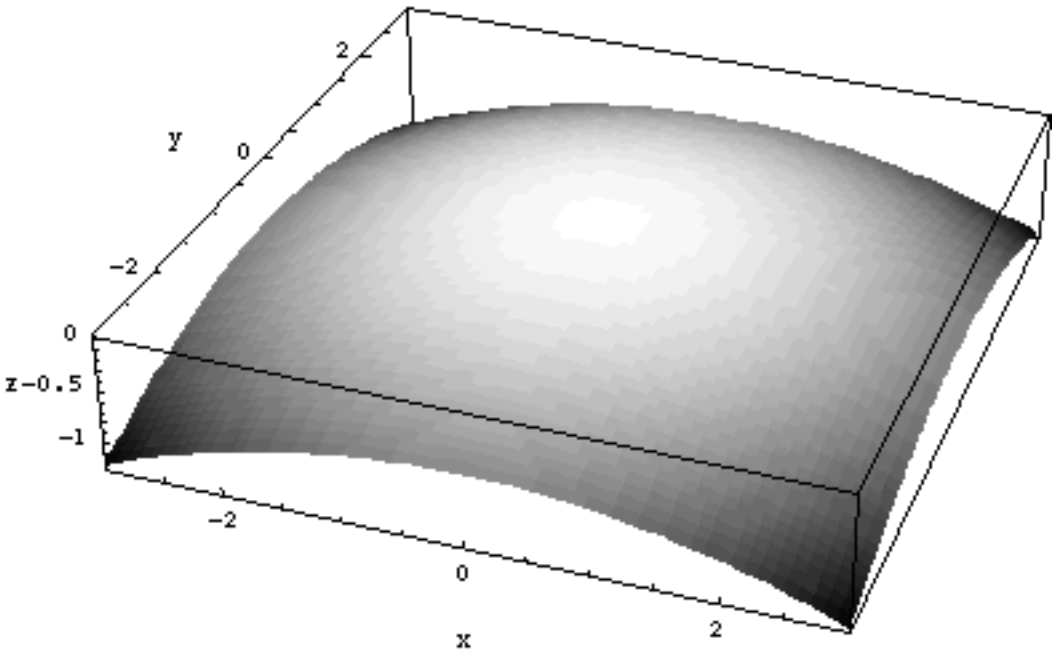

Figure 5.9: A three-dimensional view of our simulated cornea, modeled as an ellipsoid with $A = 8.7$, $B = 9$ and $C = 10$.

focusing distance indicate little here other than the focus is worse away from the center, and that the errors are close to rotationally symmetric.

5.3.2 Real Data

This data is from a patient with keratoconus [6, 68, 75], a condition in which the cornea has a local region of high curvature, which for this cornea is an oval region in the lower left of the image. This data was reconstructed from the ring patterns shown in Figure 1.2. Of our metrics, instantaneous mean refractive power and focusing distance highlight the keratoconus best. In fact, instantaneous mean refractive power gives similar values for the amount of curvature in the region as does instantaneous power, Gaussian power, and mean sphere. The axial refractive power map has a crescent shape because the

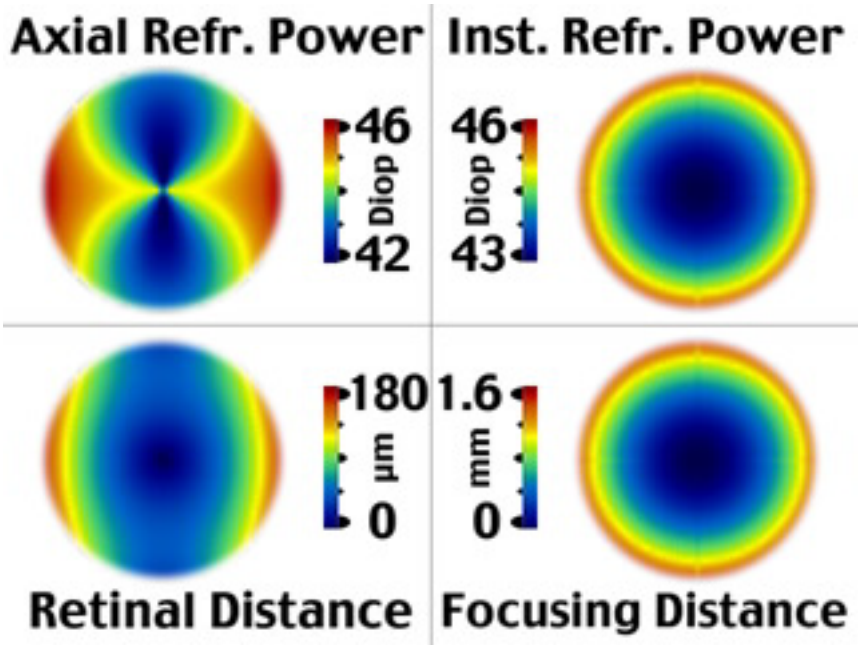

Figure 5.10: Figure 10: A view of our four acuity metrics for ellipsoidal simulated data.

keratoconus is eccentric and results in some astigmatism. Retinal distance, in conjunction with focusing distance, indicates which rays contribute to good focus. In this case, only a small central area provides a good focus, as this is the only area where both maps are near zero. It is possible, however, that there is a large region away from the center which provides good focus.

5.4 Conclusion

We have presented several corneal representations of refractive power based on geometric optics, four based on paraxial focus and several based on wavefront calculations. We showed the results using simulated and real data as implemented by **CWhatUC**. Axial refractive power is familiar to clinicians who often use a similar measure for astigmatism.

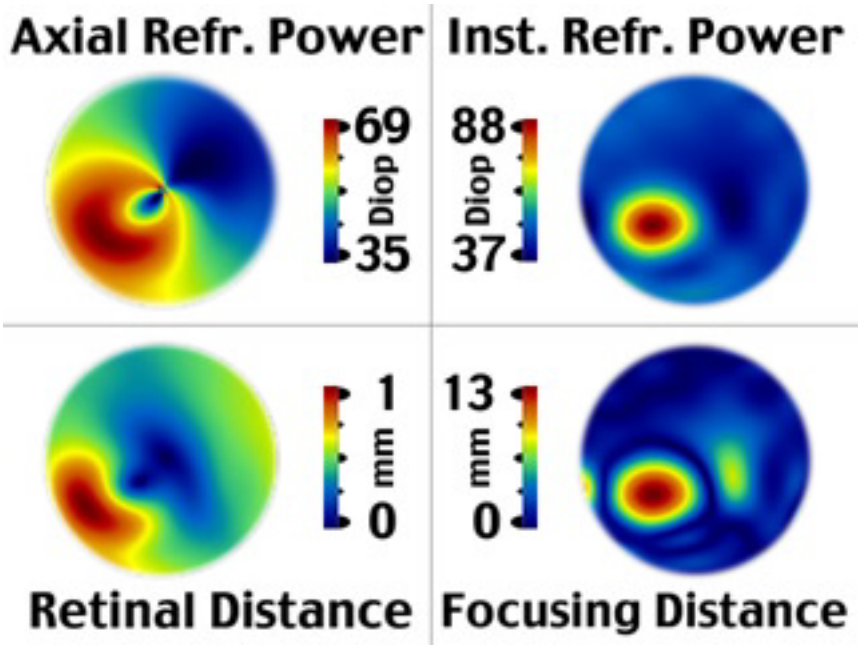

Figure 5.11: A view of our four acuity metrics for the real data of a keratoconic cornea.

Instantaneous mean refractive power is useful for describing the corneal shape, but doesn't take the PFP into account. Focusing distance and retinal distance taken together illustrate which regions contribute to a crisp focus onto the PFP. Our wavefront maps highlight how the wavefront emanating from a best focus deviates from ideal as it passes out of the cornea. In summary, these visualizations, when used to supplement one another, provide additional insight into the prediction of a patient's visual acuity.

Chapter 6

Retinal Representations of Refractive Power

> How do you know the color blue you see is the same as the color blue I see?
> — *Dennis Miller, comedian*

6.1 Introduction

Our goal continues to be the accurate and informative display of the corneal contribution to visual acuity. In Chapter 5, we described *corneal* representations; here we will center our discussion on *retinal* representations. These utilize geometric, or ray optics to reveal how well parallel light comes to a crisp focus on the retina of the eye. We make use of two standard techniques common for describing the quality of optical systems, and introduce a novel visualization which combines shape and acuity methods. We then investigate how pupil size affects the representations. Finally, we show how effective this is for monocular diplopia, as it reveals exactly which area of the cornea contributes to the ghost

image.

6.2 Methods

We wish to measure how well the corneas focus light from a single, distant source like a bright star. One standard technique is called the *point spread function* (PSF), which is the retinal energy distribution from a point source [2, 11, 52, 57, 87, 115, 116]. Its frequency response is called the *modulation transfer function* (MTF), which allows easy comparisons with an ideal, or diffraction-limited system [109, 117]. We introduce a new technique called the *corneal PSF*, in which we overlay a pseudo-colored cornea with contour lines of equal distance to the best PSF focus, similar to the *retinal distance* calculation from Chapter 5. As always, our model of the eye is the simplified schematic representation from Section 3.1.

6.2.1 Point Spread Function

We begin the calculation of the PSF by ray tracing light through the system and onto the retina, as others have done [16, 17, 37, 45, 76, 77, 98, 108]. We assume the point is placed at optical infinity, so that the incoming light rays are parallel. We also assume that the retina is planar, a reasonable approximation given that our entire retinal region of interest (ROI) is 0.64 mm wide and deviates in height from a spherical retinal model by only 3 μm. The PSF is the distribution, or "spread", of light at the retina. Figure 6.1 illustrates light rays showering a cornea and forming a PSF on the retina.

We generate a *normalized* PSF (denoted $\overline{\text{PSF}}$), which is simply our PSF divided by the number of rays N_r which land:

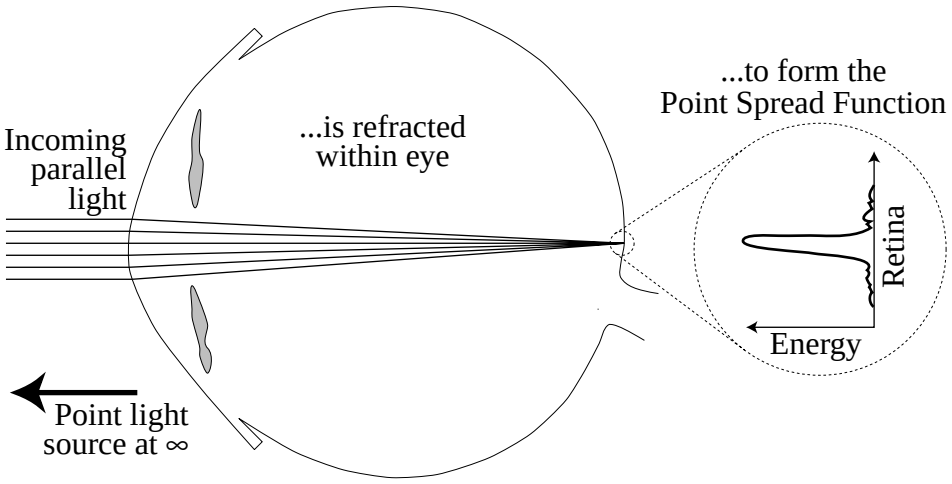

Figure 6.1: Light from a point source is refracted to form the PSF.

$$\overline{\mathrm{PSF}}(x, y) = \frac{\mathrm{PSF}(x, y)}{N_r} \tag{6.1}$$

and typically plot it as a height field for analysis, as in the example from Figure 6.2. The $\overline{\mathrm{PSF}}$ for an ideal optical system (like a perfect ellipsoid) would have a very small, localized region of height one and zero elsewhere, as we will see in Figure 6.9. The *Strehl ratio* is the relative peak intensity of an optical system's PSF with that of an ideal, aberration-free system. As we are only dealing with geometric optics, we define an equivalent concept, the *geometric* Strehl ratio, which we will call Strehl_g. Since we normalize our PSF, it is simply the maximum value of our $\overline{\mathrm{PSF}}$.

Sampling

To create the PSF, we must shower the cornea with light rays and trace them all as they are refracted toward the retina. Ideally, every microscopic patch of the cornea would

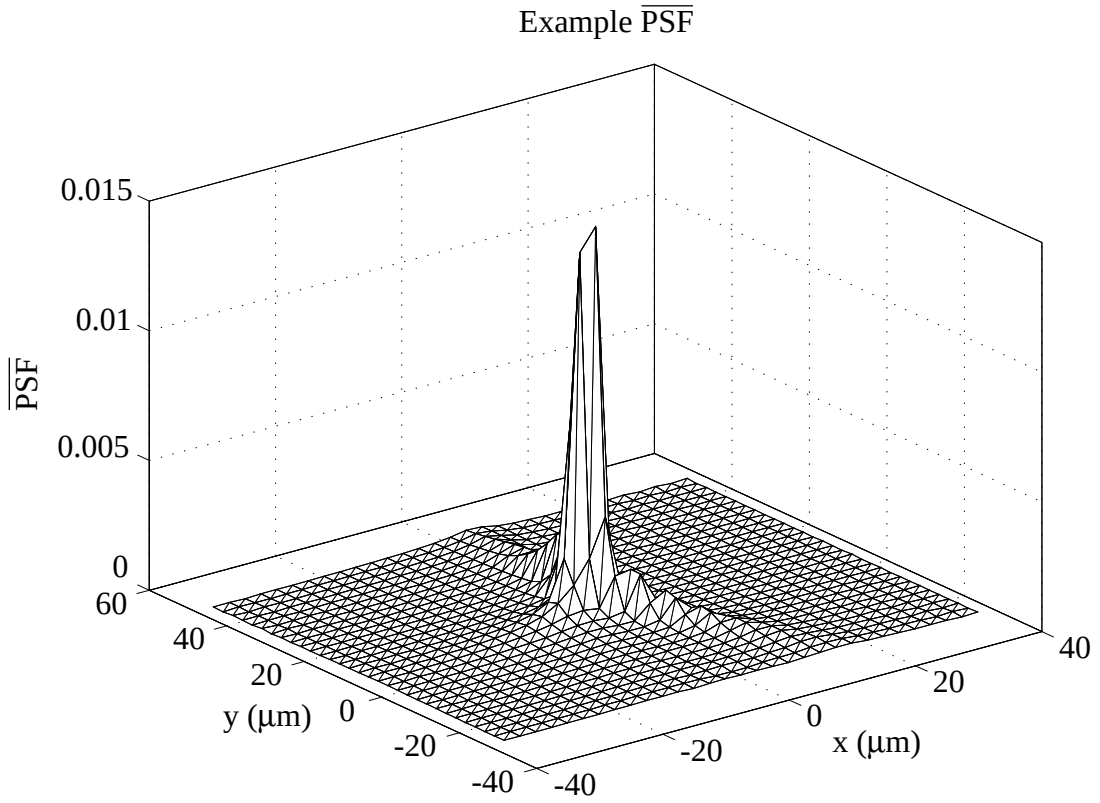

Figure 6.2: A height field representation of a sample $\overline{\text{PSF}}$.

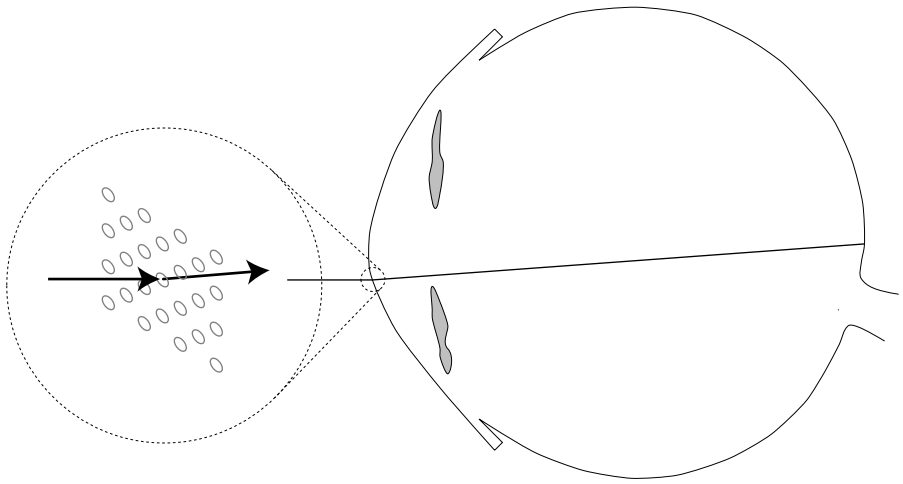

Figure 6.3: The crosshatched sampling pattern used to sample the cornea. Rays from the infinite light source pass through these samples and are refracted into the eye.

be pierced with a light ray, but for computation purposes, we must sample the continuous surface into discrete corneal points. We use a crosshatched sampling pattern as shown in Figure 6.3. We typically sample the corneas at a 100×100 resolution (with an inner 99×99 group), which produces 19,801 samples. As most corneal reconstructions are round, approximately 78% or 15,000 of those samples produce valid rays.

We introduce a *simulated pupil* located at the front surface of the eye. As we reduce the diameter of our pupil, we subsequently reduce the number of rays that are allowed to pass. This is consistent with our model that the samples represent a predefined *flux* of incoming light radiation, and culling the peripheral rays with our pupil reduces that flux accordingly. The simple expression for rays allowed to pass is that their distance from the CT axis be less than our pupil radius. That is, if the ray pierces the $z = 0$ plane with polar coordinates (r, θ), the rays allowed to enter are those satisfying the expression

$$r < r_{pupil}. \tag{6.2}$$

At each sample in our pupil, we query point and derivative information necessary for determining the refraction into the eye. It is here that we apply our simulated *spectacle correction*. We found that simple aberrations based on astigmatism dominated our distribution, so we compensate by placing a simulated infinitely thin contact lens on the cornea to correct for basic cylinder. We search to find the optimal cross-cylinder lens that gives the best retinal focus, which we discuss shortly in Section 6.2.1.

The corrected ray then enters the corneal surface according to Snell's law as we saw in Equation 2.6 and was illustrated in Figure 2.8. After the rays pass through the cornea and eye, they intersect the retinal "plane", which is a variable distance away. This distance is the third and final parameter in our spectacle correction optimization.

We then sample the retinal plane, dividing it into 257×257 square buckets which are 2.5 μm, or roughly one-half minute on a side. This produces a square retinal "patch" which is 0.6425 mm on a side. Figure 6.4 shows a ray striking the retina and landing within one of the sample buckets.

Every time a ray lands in a sample, it contributes one unit to our histogram. The accumulation of all the rays forms the overall PSF energy distribution. If a ray lands in the center of a sample, that sample receives the entire unit energy contribution. However, if a ray does not land in the direct center of a sample, we contribute some of its energy to its neighbors. The distribution is based on the amount of overlap of an unweighted unit cube centered at the point of intersection. Our retinal patch is large enough that most corneas have all rays land in it. If not, the rays are considered *stray*, and are not counted.

Figure 6.5 illustrates the contribution into several sample samples for a ray that

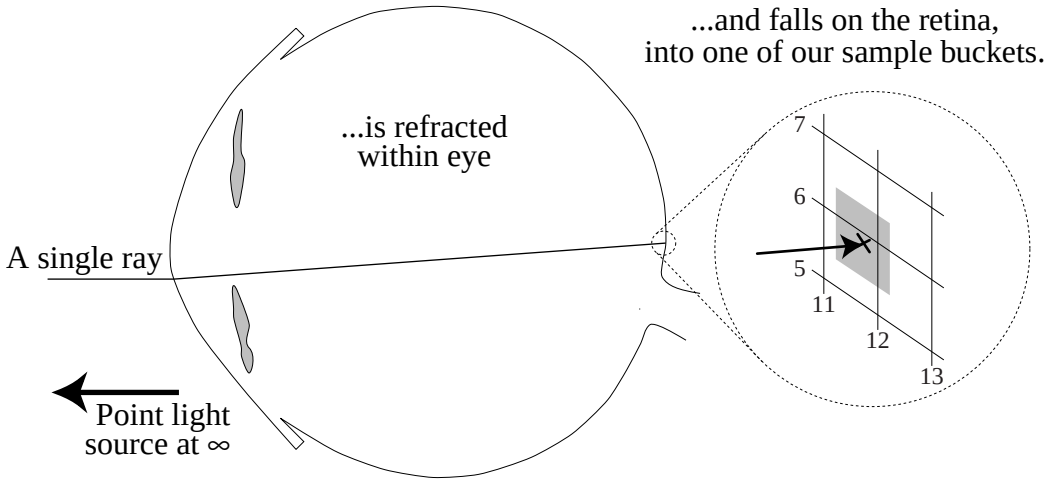

Figure 6.4: A refracted ray lands in one of the sample buckets on our retinal plane.

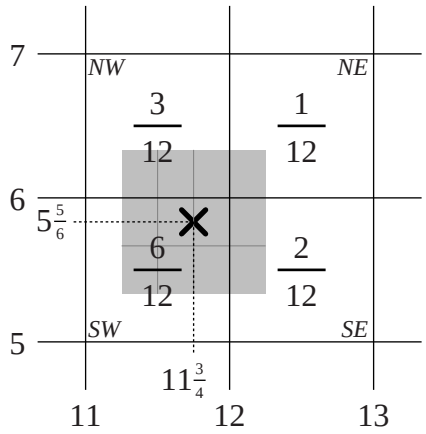

Figure 6.5: The distribution of an off-center ray contributes energy into several neighboring samples. This top-down view demonstrates what happens when a ray lands in a sample labeled SW at the point $(11\frac{3}{4},\ 5\frac{5}{6})$, shown as a cross. One-fourth of the unit cube (representing the unit ray contribution) is east of the line $X = 12$ and one-third is north of the line $Y = 6$, so the neighbors here receive the appropriate number of $\frac{1}{12}ths$ of the cube corresponding to the overlap. Sample SW gets 6, NW gets 3, SE gets 2, and NE gets only 1 of the 12 $\frac{1}{12}ths$ contribution.

hits off-center. The ray lands at the cross in sample SW, at the point $(11\frac{3}{4}, 5\frac{5}{6})$, and the distributing unit cube overlaps samples labeled *SW*, *SE*, *NW* and *NE*. One-fourth of the cube is east of the line $X = 12$ and one-third is north of the line $Y = 6$, which makes calculations in this example quite easy. Sample *SW* receives $\frac{6}{12}$ or $\frac{1}{2}$, *NW* receives $\frac{3}{12}$ or $\frac{1}{4}$, *SE* receives $\frac{2}{12}$ or $\frac{1}{6}$, *NE* receives a scant $\frac{1}{12}$ of the original unit ray contribution.

The problem with this sample distribution technique is that it creates *aliasing* artifacts. Let us assume there are two eyes, A and B, which are both ideal linear systems as described in Section 3.2.4 and that focus all incoming light rays onto one point. With A, that point is in the center of a sample (as shown in Figure 6.6), but with B that point is in the corner of a sample grid (as shown in Figure 6.7). The $\overline{\text{PSF}}$ in both cases should reflect this refractive perfection accordingly, and in fact A does exactly that — its center sample has a height of one. However, with eye B, there are four neighboring central samples who each have a height of one-quarter. Any algorithm that searches purely on the basis of the Strehl_g ratio (the maximum height of the $\overline{\text{PSF}}$) will always choose A over B, even though both eyes have identical refractive properties.

To solve this aliasing problem, we smooth our histogram with a post-processing step. That is, we anti-alias by convolving the initial PSF with a simple 2×2 window where each slot is simply $\frac{1}{4}$, and use the resulting smoothed PSF for all search algorithms which optimize for maximum intensity. Table 6.1 shows a graphical representation of our smoothing filter. After smoothing, both eyes A and B have equal maximum amplitude.

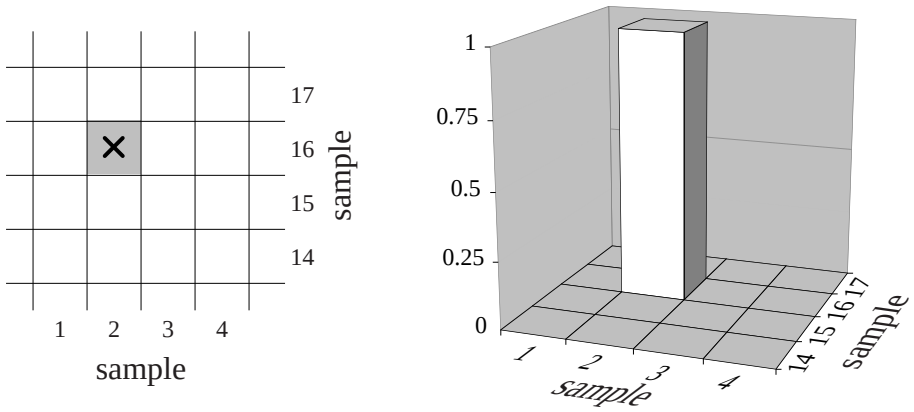

Figure 6.6: The $\overline{\text{PSF}}$ for ideal eye A. All light is focused to the center of sample (2,16) as indicated by the cross, so the entire sample receives all the energy from the rays. The Strehl$_g$ ratio for this eye is one, as it should be.

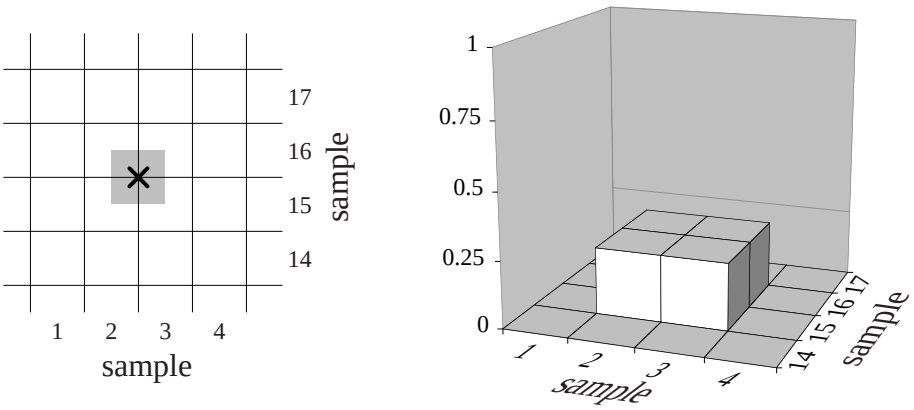

Figure 6.7: The $\overline{\text{PSF}}$ for ideal eye B. All light is focused to the intersection of four samples, at the lower-right of sample (2,16) as indicated by the cross, so the four neighboring samples share the energy from the rays. All four receive equal one-quarter energy distributions, and the Strehl$_g$ ratio for this eye is one-quarter.

1/4	1/4
1/4	1/4

Table 6.1: The 2×2 post-processing smoothing filter we apply to the PSF for our optimization.

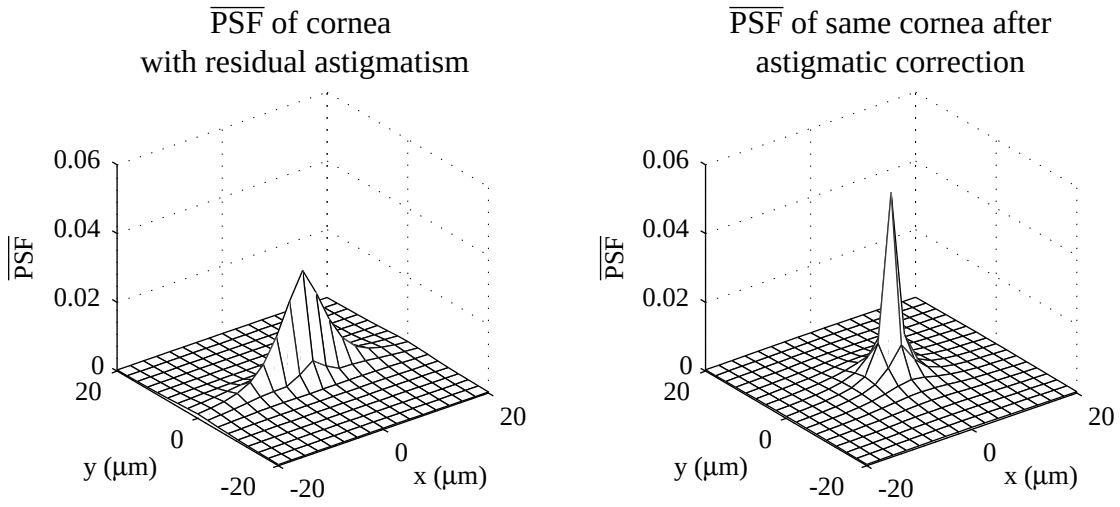

Figure 6.8: The $\overline{\text{PSF}}$ of an astigmatic cornea before and after our cylinder correction.

Spectacle Correction Optimization

If the cornea is not rotationally symmetric, there will be some astigmatism and the PSF distribution will be smeared along the cylinder direction. To correct for this, we place an infinitely thin virtual cross-cylinder contact lens in front of the cornea. Figure 6.8 shows the $\overline{\text{PSF}}$ of an astigmatic cornea before and after our correction.

This lens affects the direction of the incoming parallel light slightly to reduce the aberration. The incoming unit ray P is modified as shown in equation 6.3 below and then renormalized. J_0 and J_{45} are the cross cylinder correction terms (oriented at 0° and 45° respectively) as mentioned in Section 2.3.2:

$$\begin{aligned} P_x &= P_x + 2J_0P_x + J_{45}P_y \\ P_y &= P_y - 2J_0P_y + J_{45}P_x \end{aligned}$$

$$P_z \quad = \quad P_z \tag{6.3}$$

We use a constrained minimization (Matlab's built-in function `constr`) to search for the optimal J_0 and J_{45} values which produce the best focus. What indeed constitutes the "best focus" is discussed in the following subsection. Our Jackson cross cylinder terms compensate for any residual corneal astigmatism, and the average refractive power is handled by the focusing distance to the retina. More specifically, we also include R, the distance from the apex of the cornea to the retinal plane as a parameter in our optimization. The constraints we place on these three variables are the following:

$$\begin{aligned} 20\text{mm} \leq \quad & R \quad & \leq 40\text{mm} \\ -5\text{D} \leq \quad & J_0 \quad & \leq 5\text{D} \\ -5\text{D} \leq \quad & J_{45} \quad & \leq 5\text{D} \end{aligned} \tag{6.4}$$

We found our minimization to be quite sensitive to initial conditions. It would often settle on a *local minima* if its starting position was not close to the final solution. To correct for this, we took a three-pronged approach, which worked quite well.

Multiple Scans Whenever possible, we use several scans of the same patient's data, allowing us to correlate with previous solutions.

Progressively Larger Pupils We begin with a very small pupil (diameter $\frac{1}{2}$ mm) and iterate through larger pupils by steps of $\frac{1}{2}$ mm until we reach our desired diameter. We feed the previous iteration's solution for (J_0, J_{45}, R) as the initial condition into the current step.

Multiple Resolution PSF We use a multiple resolution approach to make sure most rays land in the PSF in the initial steps of our optimization. We enlarge our PSF by a factor of 128, so instead of being our usual patch 0.6425 mm on a side, it is now 82.24 mm on a side. This *coarse* resolution search then progresses until it has found an optimization in which most rays fall into one large sample. Then we immediately turn on the normal *fine* resolution search using that course solution as the initial condition.

Primary and Secondary Focus

In summary, given a cornea and a pupil diameter, we search for the best focus while varying three variables: the retinal distance R, and the two cross cylinder corrective terms, J_0 and J_{45}. What is a "best focus"? Hopefully whatever mathematical notion we designate would correlate well with clinical evidence. We have chosen the maximum height of the smoothed PSF to be the metric we optimize. If the location of this peak intensity on our retinal plane is (x_p, y_p), the 3D location of the best focus is the point (x_p, y_p, R).

One of the fundamental problems with monocular diplopia is that the patient sees two points when fixating at a single, distant light source. The second point is often out of focus, and off-center in the visual field. In these cases, our goal is to determine the location of this secondary focus. We begin by highlighting all rays whose retinal intersection lies within a fixed radius, say 10 microns, of the primary focus. We remove these principal-focus rays from the calculation and then do a search for the next-best focus using all remaining rays, while keeping the spectacle correction terms fixed.

6.2.2 Modulation Transfer Function

One other common technique to measure the performance of an optical system is to analyze the modulation transfer function (MTF) [117]. It describes the contrast transfer as a function of spatial frequency [94]. The MTF is the modulus, or absolute value of the complex-valued *optical transfer function* (OTF):

$$\mathrm{MTF}(u,v) = |\mathrm{OTF}(u,v)| \tag{6.5}$$

where the OTF is simply the Fourier transform $\mathcal{F}$ of the normalized PSF, or $\overline{\mathrm{PSF}}$:

$$\mathrm{OTF}(u,v) = \mathcal{F}(\overline{\mathrm{PSF}}(x,y)) = \int_{-\infty}^{\infty}\int_{-\infty}^{\infty} \overline{\mathrm{PSF}}(x,y) e^{-j2\pi(f_x x + f_y y)}\, dx\, dy. \tag{6.6}$$

We average the MTF surface radially about its center to generate a curve as a function of spatial frequency. We will examine the MTF curves for five pupil sizes and four corneas in Section 6.3.1 and plot the curves for all of the corneas in Chapter 8.

6.2.3 Corneal PSF

The goal of the corneal point spread function (corneal PSF) visualization is to create a representation that reflects how well each area of the cornea contributes to a good focus on the retina. It also provides a multidimensional display, allowing for correlations between corneal shape and corneal acuity to be drawn. In truth, it is really a corneal representation, but its connection to retinal displays is so strong, we include it here.

We begin with a simple corneal shape display of Gaussian curvature from Section 2.1.5. However, instead of our usual cylinder vector field, we overlay contour lines of

equal retinal distance from the primary focus, at intervals of $\frac{1}{2}$, 1, and 2 minutes. That is, for every ray that pierced the particular corneal location, we determine where it intersects the retinal plane and determine its distance to the primary focus. In the case of monocular diplopia, we use the secondary focus to overlay yet another set of retinal distance contour lines, this time calculated from the other focus. We recall that one minute on the cornea translates to a distance of approximately 5 μm.

The colormap we use is smooth and not contoured (i.e., not quantized) since we want the contour lines to be highlighted in this display; a quantized colormap with its inherent color contour lines may obscure and be misleading. However, to make the differences in the Gaussian curvature more apparent, we choose a rainbow colormap with its several contrasting hues rather than our standard hot colormap.

6.3 Results

In this section, we present some of our results using these visualizations. We show the effect of pupil size on a small subset of corneas, and highlight the monocular diplopic cornea, as the cornea PSF representation is quite revealing. Chapter 8 contains the results of running all 12 corneas we described in Chapter 3 through all of our visualizations, including the three mentioned in this Chapter.

6.3.1 Effect of Pupil Size

When pupil size decreases, aberrations are reduced but diffraction effects begin to limit visual acuity. As we mentioned, our computational model ignores these diffraction

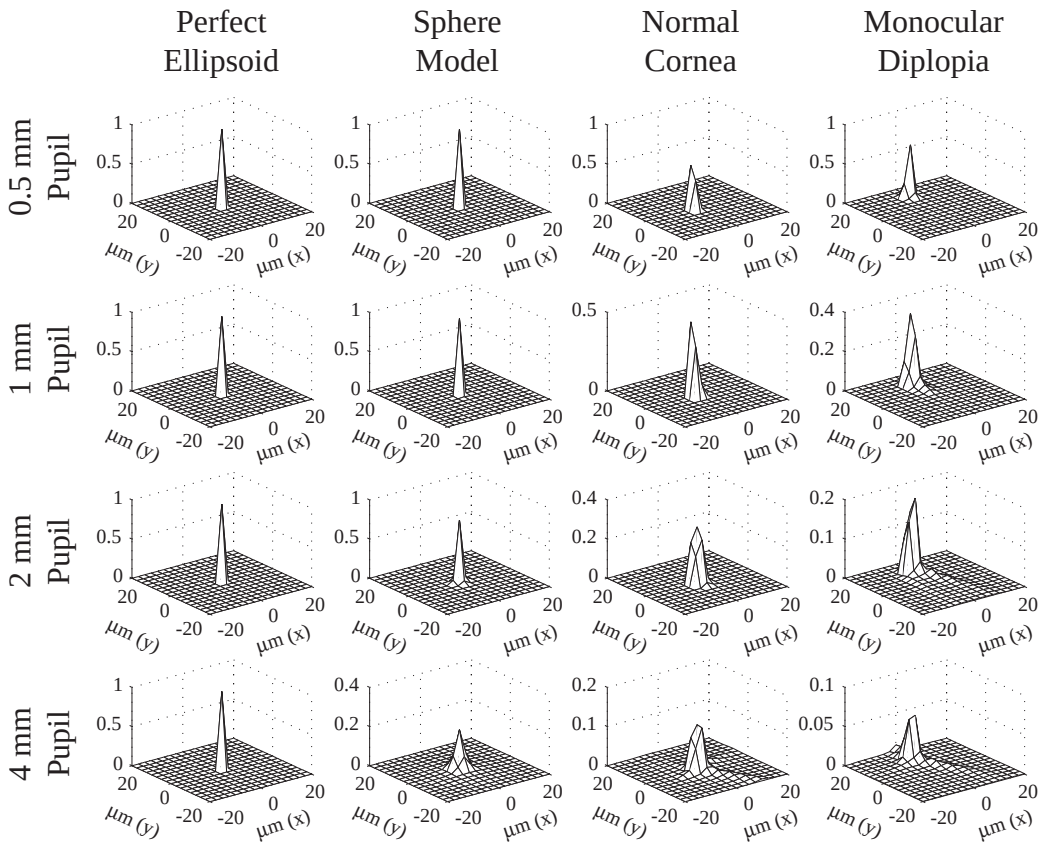

Figure 6.9: A matrix of $\overline{\text{PSF}}$s for four different pupil diameters (top to bottom): $\frac{1}{2}$, 1, 2, and 4 mm and four different corneas (left to right): perfect ellipsoid, sphere model, normal cornea and one with monocular diplopia. The x- and y-range is the same for every eye and pupil, -20 μm to 20 μm. We allowed the z-height to be auto-ranging.

effects and thus our corneas all converge to ideal optical systems as the pupil size approaches a pin hole. In this section, we will look at five pupil diameters: $\frac{1}{2}$, 1, 2, 4 and 8 mm and how their size affects the $\overline{\text{PSF}}$ and MTF for several eyes, both real and simulated. We will explore four corneal datasets, two simulated and two real: the perfect ellipsoid from Section 3.2.4, the spherical model from Section 3.2.1, the normal eye from Section 3.4.1 and the monocular diplopic eye from Section 3.4.5.

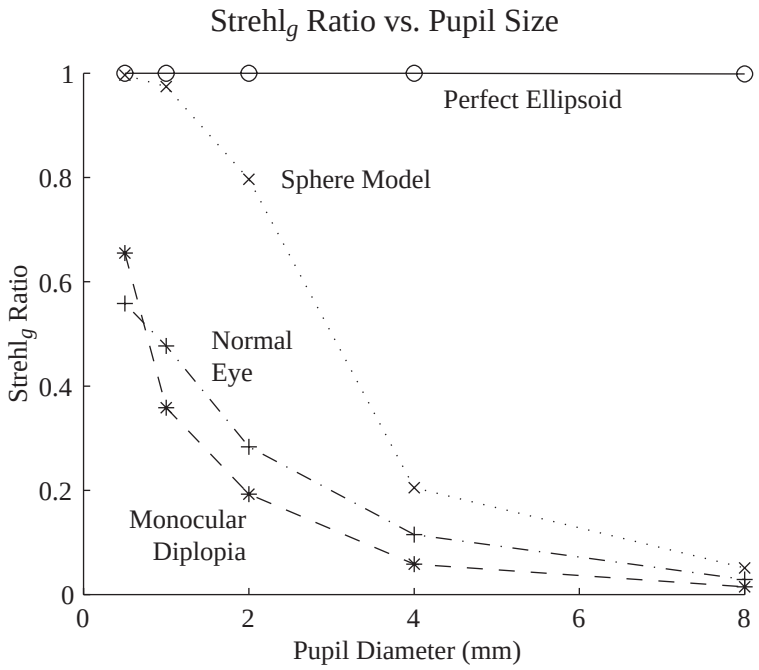

Figure 6.10: A plot of Strehl$_g$ ratio vs. pupil size for four different corneas (from best to worse performing): perfect ellipsoid model, sphere model, the normal eye and the monocular diplopia. Note that this last cornea actually performed better than the normal eye with a $\frac{1}{2}$ mm pupil.

Normalized Point Spread Function

Let us examine Figure 6.9 — pay careful attention to the different Strehl$_g$ ratios measured on the z-axes, as all the graphs are auto-ranging. We lock our x- and y-limits for each graph to the same range, -20 μm to 20 μm. We also include a plot of Strehl$_g$ ratio vs. pupil size in Figure 6.10.

As expected, the perfect ellipsoid maintains its perfection (Strehl$_g$ ratio of 1) even as we increase our pupil diameter to 4. The sphere model starts to falter at 2 mm, and by 4 mm has fallen to 20%. However, it remains rotationally symmetric and has no significant trailing energy.

Our normal cornea, even with a $\frac{1}{2}$ mm pupil, just barely peeks above 50%. It

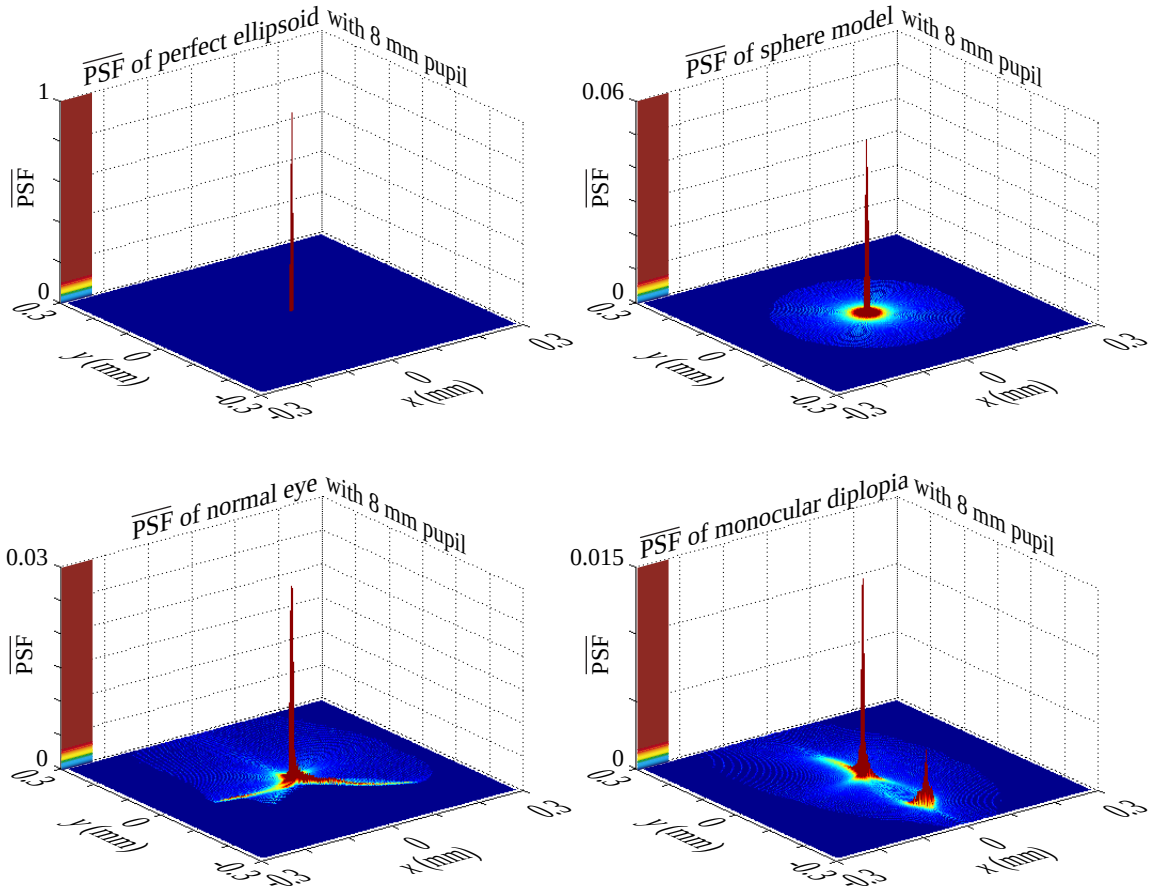

Figure 6.11: Color $\overline{\text{PSF}}$s from 8 mm pupils for four different corneas (clockwise from top left): perfect ellipsoid model, sphere model, monocular diplopia and the normal eye.

drops to 20% at 2 mm, and is all the way down to 10% with a 4 mm pupil. We can see a small tail of energy in the negative y-direction with the 4 mm pupil; we will investigate this more closely in Figure 6.11. With a $\frac{1}{2}$ mm pupil, the monocular diplopic eye has a peak which starts about 15 μm above the center (in the y-direction), but surprisingly, has acuity a little better than the normal eye. It begins to fall off very quickly, and by 4 mm is half as effective as the normal eye. There also appears to be small energy tails in the positive and negative y-direction.

Figure 6.11 plots enlarged and colored versions of the $\overline{\text{PSF}}$s with an 8 mm pupil. It

is at this diameter where things really become interesting. We widened the x- and y-limits to almost 10 times that of Figure 6.9; now, each ranges from -300 μm (-0.3 mm) to 300 μm (0.3 mm). The z-axes are still auto-ranging; otherwise, the perfect ellipsoid would dwarf out the others, at over 30 times the intensity. We compress the colormap to only the lower 5% of this peak value so any residual distribution of light surrounding the primary peak stands out.

We see the perfect ellipsoid in the upper left holding firm with a Strehl$_g$ ratio of 1. Our sphere model in the upper-right is the next best with 6%, a symmetric distribution and a radial spray of stray energy due to spherical aberration. In the lower-left, we see our normal eye with a Strehl$_g$ Ratio of 3%, half that of the sphere model. There are two stray threads of light energy, one toward the left (negative x-direction), and one toward the lower right. The spray of peripheral rays continues above and away from these threads in a pretty even distribution. We discuss the monocular diplopia eye in Section 6.3.2 as it is so unusual.

Modulation Transfer Function

In Figure 6.12, we overlay the MTF curves for all five pupil sizes on one chart for each of the four eyes we have been investigating. What is not surprising is that the perfect ellipsoid maintains a height of one for each of its pupil diameters; we know the Fourier transform of an impulse is unity. The Sphere model begins at near perfection for the smallest two pupils, but falls off quickly as the diameter begins to grow. Our normal and monocular diplopic eye are quite similar, except for the slight scaling. There is no evidence of the second focus in the latter cornea, perhaps due to our radial averaging.

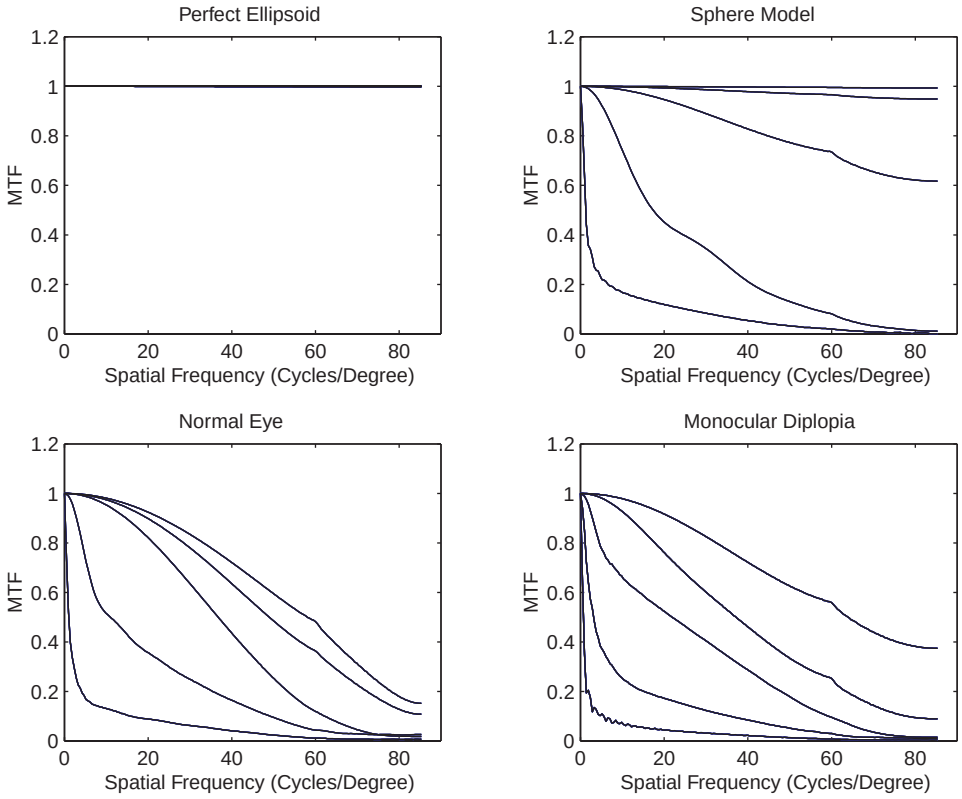

Figure 6.12: MTF curves for five different pupil diameters (in mm): $\frac{1}{2}$, 1, 2, 4 and 8 and four different corneas (clockwise from top left): perfect ellipsoid model, sphere model, monocular diplopia and the normal eye. We plot all five curves at once on each diagram; the $\frac{1}{2}$ mm pupil curve is always closest to unity, the 1 mm pupil curve right below that, and so on.

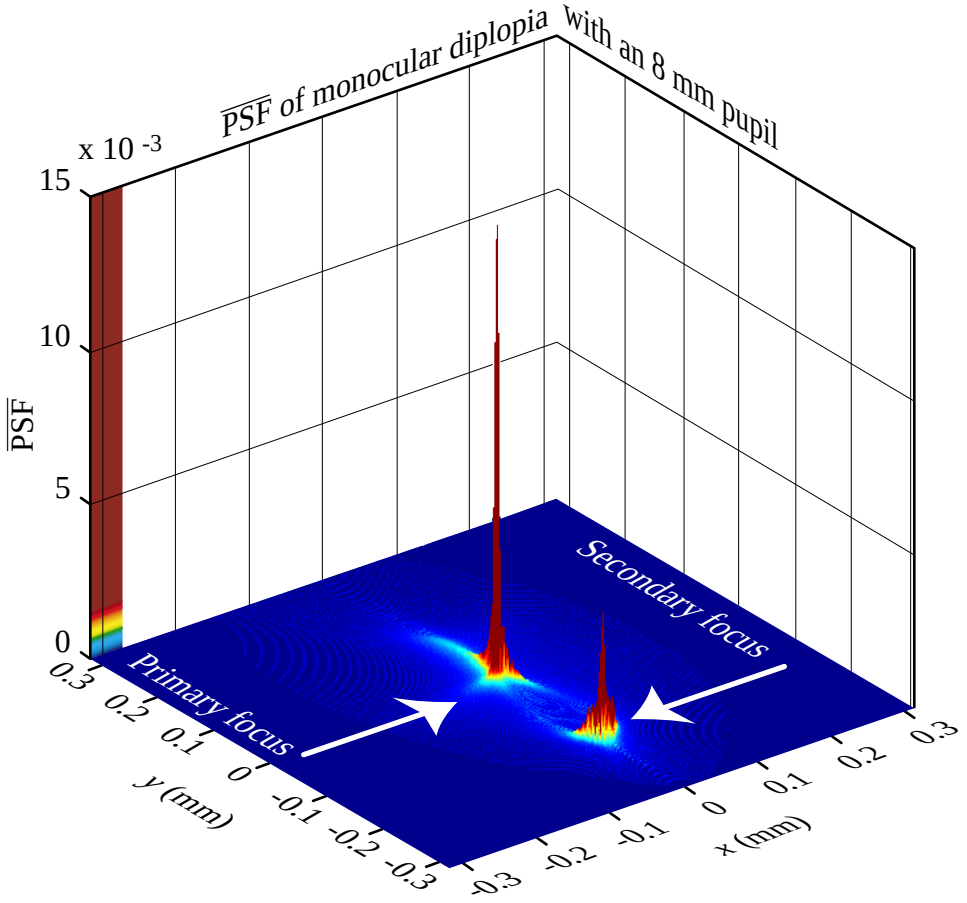

Figure 6.13: The $\overline{\text{PSF}}$ for the monocular diplopic eye with an 8 mm pupil. The primary focus is indicated by the energy peak in the center of the figure. The patient's perceived dual image is caused by the second peak approximately 0.2 mm below the first. This maps to the area of reduced curvature in the upper cornea on the corneal PSF image in Figure 6.14.

6.3.2 Monocular Diplopia

In this section we focus on the very interesting dual-peak $\overline{\text{PSF}}$ function for the monocular diplopic cornea in the lower-right of Figure 6.11. We would like to determine what corneal region causes the second focus. In Figure 6.13 we magnify the $\overline{\text{PSF}}$ to examine its features.

The primary focus does not have very much strength, with only a 1.5% Strehl$_g$

ratio, half that of the normal eye. The peak itself is roughly symmetric, with a little more distribution in the y-direction. There is a remarkably strong *second focus*, almost $\frac{1}{3}$ as high as the primary one, and located 0.2 mm below it. This correlates well with the patient's perceived ghost image (measured at 0.8° above her main focus) and other analysis of this data [108].

Let us now turn our attention to the corneal PSF in Figure 6.14 to see what regions of the cornea contribute to these foci. The large yellow central region is the primary focus, and the size of the 2 minute circle is quite large. There are two inner regions labeled $\frac{1}{2}$ minutes; this is because the innermost retinal distance climbs back above $\frac{1}{2}$ min.

Two dominant shape features stand out in the corneal PSF map. There is a large red region of high curvature (47 D) in the upper-central area. Above that is an even larger region of low curvature (40 D). We see it is this low curvature region that is behind our secondary focus, and ghost image. The area within our secondary focus contour lines (especially within $\frac{1}{2}$ min) is smaller than that of the primary focus, which we expect, since the corresponding energy in Figure 6.13 is much less. As shown here, the corneal PSF visualization is quite an effective tool for determining the source of the secondary ghost image.

6.4 Conclusion

In this chapter, we described several retinal representations meant to capture the optical quality of the eye from the receiving end — the retina. We presented two familiar visualizations, the point spread function (PSF) and the modulation transfer function (MTF).

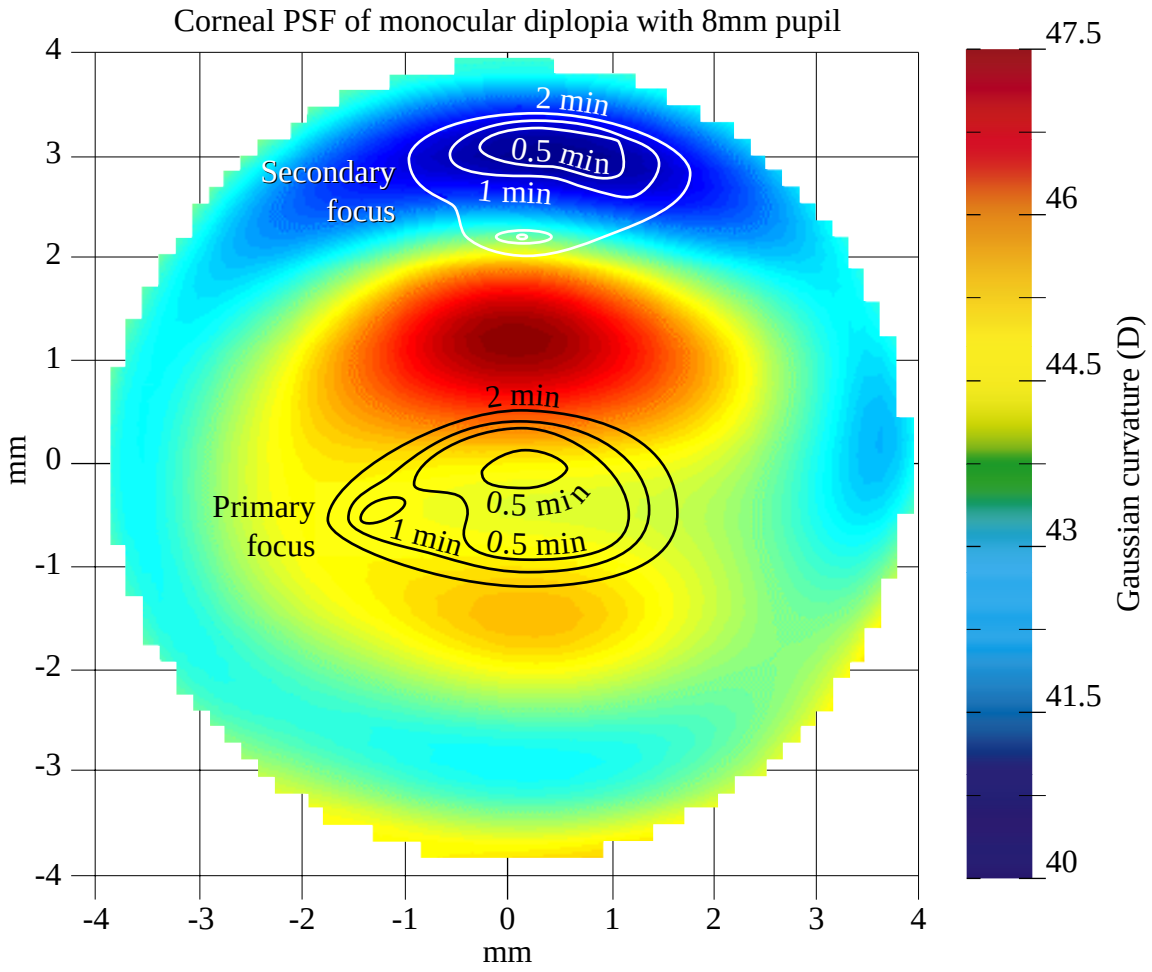

Figure 6.14: The corneal PSF for the monocular diplopic eye with an 8 mm pupil. The primary focus is generated by the central oval region. The patient's perceived dual image is created by the area of reduced curvature in the upper central cornea, which causes the second $\overline{\text{PSF}}$ peak in Figure 6.13.

We introduced a novel multidimensional representation, the corneal PSF, which allowed us to see the direct connections between corneal shape and optical acuity. This is our first set of computational models which took the pupil size into effect. As our model did not consider diffraction effects, we showed how the corneas approached ideal optical systems as we reduced our pupils to a pinhole. Finally, we isolated a particular corneal condition, monocular diplopia, and showed how revealing the corneal PSF could be for determining the corneal location and cause of the second image.

Chapter 7

See What You See : Simulating Corneal Visual Acuity

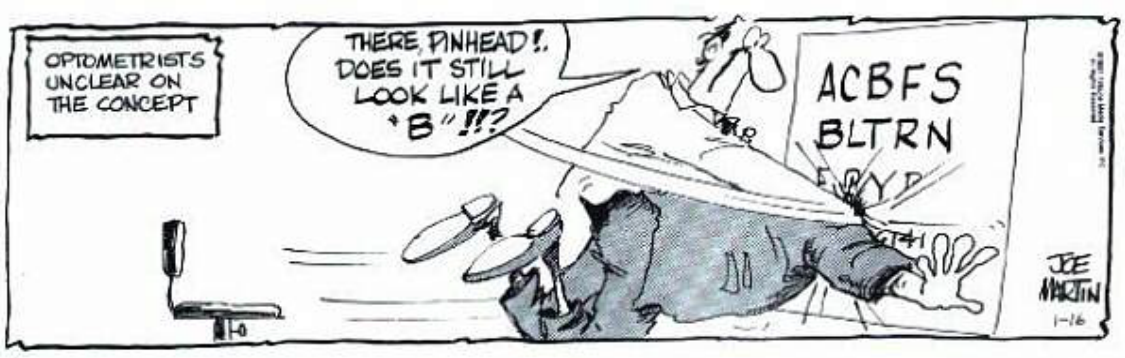

— Mr. Boffo © 1997 Joe Martin, Inc. Reprinted with permission of Universal Press Syndicate. All rights reserved.

7.1 Introduction

Our goal with this work is to simulate the corneal contribution to visual acuity. In the previous chapter we showed retinal representations of corneal acuity, but these fail to capture what the patient actually sees. We utilize a modified Snellen eye chart and

a sample outdoor scene as our input, and image how they would be seen with different patient's corneas and pupil sizes to achieve a fairly accurate first-person representation of visual acuity.

7.2 Methods

The use of ray tracing to determine the PSF and the resulting retinal blur for images such as Snellen charts is not new. Section 2.4.3 discusses several prominent researchers who have created sophisticated models and optical bench software tools using ray tracing for evaluation of optical performance.

We choose to implement the technique as part of our software suite to provide the final stage of visualization, the simulation of optical acuity through the cornea in question. In this section we'll discuss the process of calculating the $\overline{\text{PSF}}$, calibrating it with an image, and convolving them together to form the final blurred result.

It is important to note the assumptions and limitations of this technique for the simulation of visual acuity. First, it assumes that all incoming light is parallel, having arrived from optical infinity. Thus, we can only simulate what a patient would see while looking at something reasonably far away. Second, the computational model described in Section 3.1 is very simplistic and does not take other components of the eye into account, like the lens, vitreous humor or corneal layers. This means the many effects they induce (e.g., ciliary bloom and lens glare) are completely ignored. Third, the pupil only expands to large diameters in extremely low light situations, so simulating the aberrations with an 8 mm pupil on a daylight scene is quite artificial. Finally, as all of our $\overline{\text{PSF}}$ construction

uses ray tracing and geometric optics, we ignore the important effects of diffraction, which is the limiting acuity factor for small pupils.

7.2.1 Normalized Point Spread Function

We begin with the normalized point spread function, $\overline{\text{PSF}}$, a computed histogram of retinal energy from a distant point source of light as discussed in Section 6.2.1. This serves as the "impulse response" of the patient's optical system. As we mentioned, we sample the retina at half-minute (2.5 micron) intervals; this will be important in the following section on image calibration.

7.2.2 Image Calibration

When we wish to apply a filter to an image, it is critical that the parameters of the filter be tuned to the spatial frequencies of the image. Our filter is the $\overline{\text{PSF}}$, which is sampled at half-minute intervals, producing a fine grid of retinal energy distribution.

Again, we are given (or synthetically generate) an input image, and our goal is to create a first-person simulation. There are two alternatives, simulating the eye in the camera's place, or simulating the patient viewing the image from afar. Each of these will affect the calibration differently, and we discuss this in the following sections.

Eye is the Camera

This is perhaps the most effective and convincing simulation, and the one we use to simulate the patient seeing an eye chart in Section 7.3.1. Here we place the eye where our camera was when the scene was captured on film as in Figure 7.1. Before we can accurately

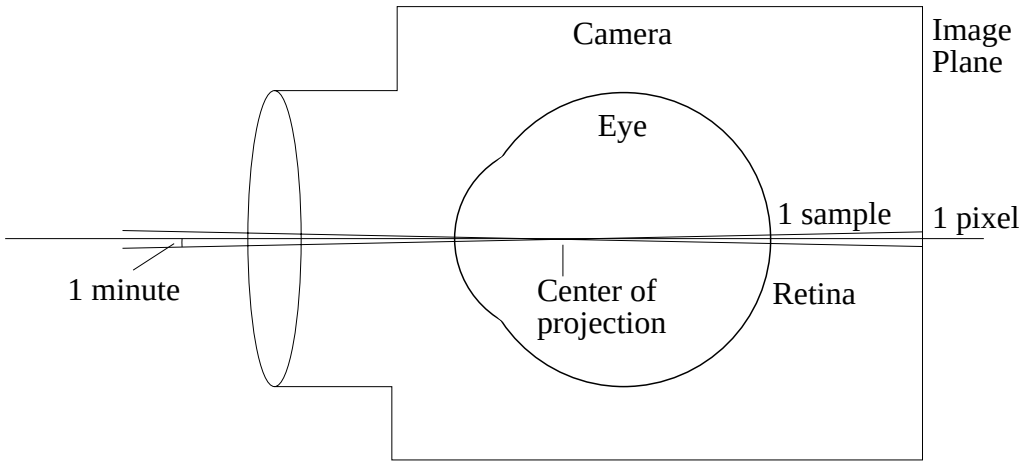

Figure 7.1: Simulation of an eye viewing an image exactly as it was seen by the camera. The centers of projection are aligned and the image is scaled so that one pixel on the image maps to one sample on the $\overline{\text{PSF}}$.

simulate the blur the patient would see, we must assure that they are calibrated together, as described below.

A photograph of a scene is taken, or one is synthetically generated. Real or virtual camera information is recorded, e.g., lens, field of view, center of projection, image plane distance, etc. The image is then digitized (or rendered) at the same spatial frequency as our filter.

If we have control over the digitization and camera information, we simply tune our sampling resolution to the correct value. If we do *not* have camera information, but *do* have objects in our scene whose distance to the camera and size we know accurately, we can still adjust our sampling as follows. We want one pixel to be thirty seconds of arc. If an object is at a distance d from our camera, this means (using the simple geometry from Figure 7.2) that:

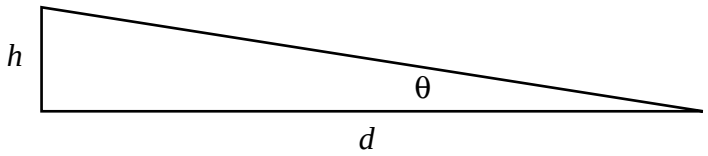

Figure 7.2: Simple geometry controls the relationship between an object's distance (d), its image size (h) and the angle it subtends (θ). That relationship is captured by the expression $h = d \tan \theta$.

$$h_1 = d \tan \theta = d \tan \left(\frac{1}{2} \frac{1}{60} \frac{\pi}{180} \right) \approx d \; 1.45444 \times 10^{-4} \tag{7.1}$$

where h_1 represents the distance in object space that we need for one pixel. If an object's size is h, then it should be $\frac{h}{h_1}$ pixels high.

If we do not have either camera or object size and distance information, we have no way to estimate how finely to sample our scene. When we do have this information, but the image has already been digitized, then there are three options. If the image is sampled at calibration density, we're done. If the image is sampled finer than that, then an intelligent bicubic interpolation can be used to reduce the image size without significant loss. However, if the image is sampled more coursely than calibration, we're in trouble. We either have to reduce the size of our filter or increase the size of our image. Either technique will result in unacceptable artifacts.

If there is no calibrating camera or object information, and the image has already been digitized, we cannot reliably put the eye in the camera. We could, however, simulate what the patient would see if they were to visualize the digitized photo on a computer monitor; this is discussed next.

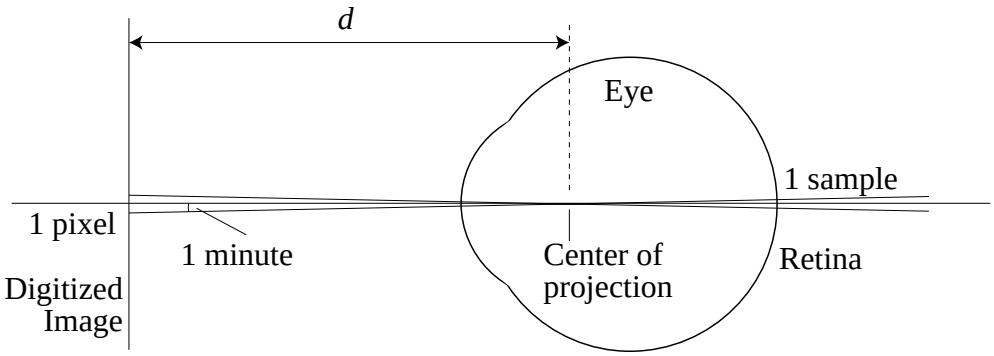

Figure 7.3: Simulation of an eye viewing a projected digitized image from afar. The eye's center of projection is placed at a distance d and the image is scaled so that one pixel on the digital image maps to one sample on the $\overline{\text{PSF}}$.

Patient Views Projected Digital Image

This technique, as shown in Figure 7.3, allows us to simulate what the patient would see looking at an image from a fixed distance. It is most useful when we do not have object information necessary for eye-is-the-camera calibration.

When images are viewed on monitors in a what-you-see-is-what-you-get (WYSIWYG) fashion, they are represented at 72 dots per inch (DPI). This means one pixel is $\frac{1}{72}$ inch. Plugging in this value for h_1 in Equation 7.1, we know the distance d must be:

$$d = \frac{h_1}{\tan\left(\frac{1}{2}\frac{1}{60}\frac{\pi}{180}\right)} \approx 95.5 \text{ inches} \approx 8 \text{ feet}. \tag{7.2}$$

Therefore, if we perform our filtering on an unmodified input image, the result would be what a person would see viewing the picture on a monitor from a distance of approximately 8 feet. This is the technique we employ with our outdoor scene from Section 7.3.2.

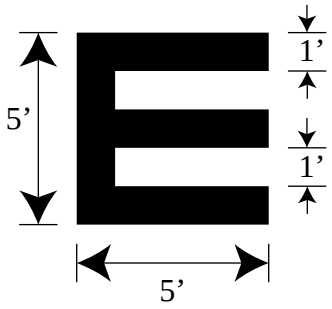

Figure 7.4: A typical Snellen letter.

7.2.3 Measuring Visual Acuity

Visual acuity is the measurement of the eye's ability to resolve the form and detail of an object. It is most commonly determined by testing the ability of the patient to read standard letters at a fixed distance [10, 25].

Snellen Notation

In 1862 Snellen devised a system for measuring acuity which has since become a fundamental clinical technique for acuity assessment [25]. The smallest detail of an object an eye can see is called the *minimum angle of resolution* (MAR) of the eye. The *Snellen fraction* is the reciprocal of the MAR. The test is usually performed at 20 ft (6 m), an acceptable approximation to optical infinity.

On a typical chart, letters are scaled so that each will subtend an angle of 5 minutes at a given distance. The details of the letters themselves make an angle of 1 minute of arc, as shown in the classic "E" in Figure 7.4. The letters are then labeled by this distance, e.g., the "20-foot" letter makes a total angle of 5 minutes at a distance of 20 feet. The classic fraction is recorded as the ratio of the testing distance and the label of the smallest

MAR	*Snellen decimal notation*	*Snellen fraction*
0.5	2	20/10
1	1	20/20
2	1/2	20/40
4	1/4	20/80
8	1/8	20/160
⋮	⋮	⋮

Table 7.1: The relationship between MAR and Snellen notations.

letter a patient can resolve. Thus, if a patient at 20 feet is only able to read the "100 foot" letter, their vision would be classified as "20/100". Table 7.1 shows the relationship between MAR and Snellen notation. A historical note: one minute of arc became a standard in the days of early astronomers who determined it to be the minimum angular separation for two different stars to be perceived as distinct [25].

Simulated Snellen Eye Chart

Tumbling E charts like the one shown in Figure 7.5 are often used for preliterate children. We choose to use a modified version of this instead of a standard Snellen chart since rendering the letter "E" to an image requires no anti-aliasing as would letters with curved edges. We are able to create Es down to 5×5 pixels with no loss.

Our test acuity image is shown in Figure 7.6, which has been calibrated so that each pixel is thirty seconds. This is the spacing between the bars of the smallest E, used for testing 20/10 acuity. We include Es which double in size up to 20/160. We add a fan pattern to test for astigmatism, whose direction is determined by the bars perceived as least blurred.

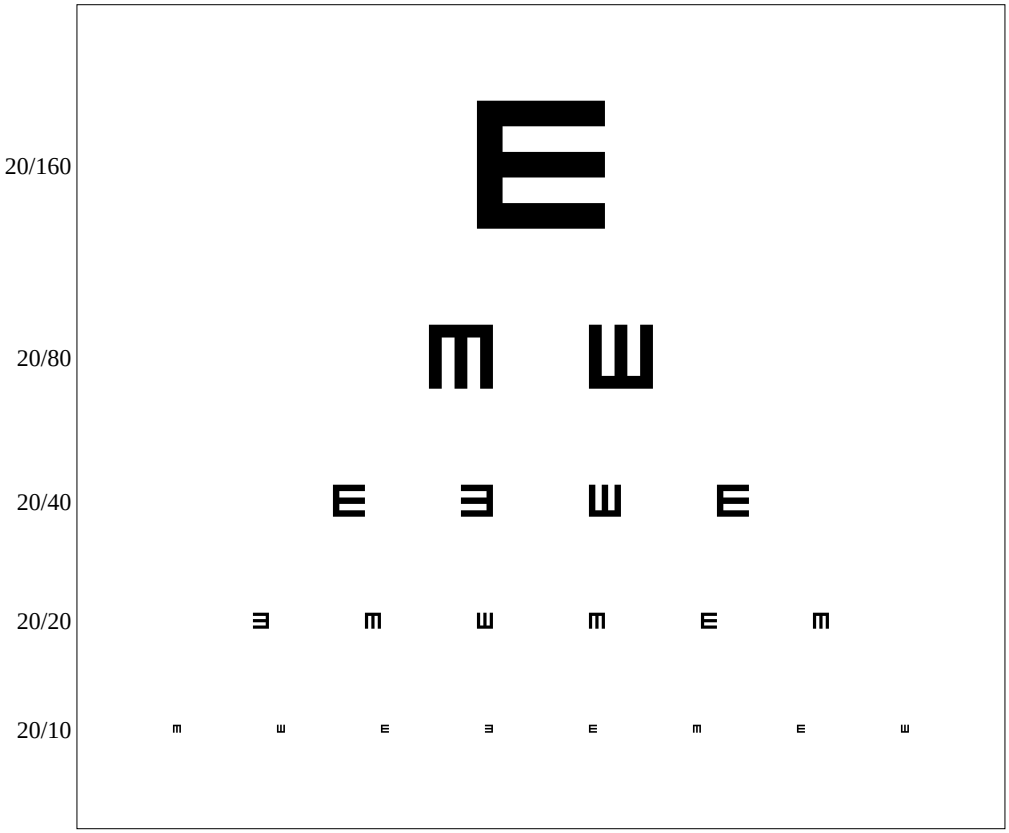

Figure 7.5: A typical acuity chart with tumbling Es used for acuity assessment of preliterate children. This chart is especially useful for us since rasterization requires no anti-aliasing as would a chart with curved-edge letters.

Figure 7.6: The image we use for our acuity simulation. The size of the Es ranges from 20/10 on the left to 20/160 on the right. The fan pattern on the far right is used to test for astigmatism.

Figure 7.7: The image we use for our outdoor scene simulation, a photograph of U. C. Berkeley's Campanile courtesy of Paul Debevec.

Outdoor Scene

As shown in Figure 7.7, the input image is a crisp low dynamic range digital photograph of U. C. Berkeley's Campanile tower, courtesy of Paul Debevec. It has clearly defined edges and a full-range luminance histogram. The simulations we present are what a patient would see when looking at the full 250×500 pixel image on a 72-dpi computer screen at a distance of 8 feet. The blur is identically computed for each of the R, G and B channels in the image, so there is no chromatic aberration in the simulation. There was no digital processing done on the input image; every pixel was simply copied from the original PhotoCD, down to the small smudge on the right of the tower.

7.2.4 Convolution

Now that we have our input images and $\overline{\text{PSF}}$ "impulse response" distribution, we simply need to convolve them together to form the blurred output images. We make use of the *convolution theorem* which tells us the convolution in the spatial domain can

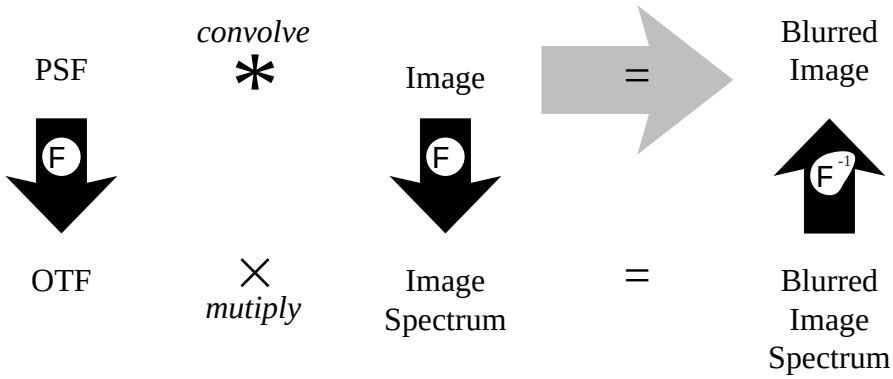

Figure 7.8: Instead of convolving the $\overline{\text{PSF}}$ with our image (shown in grey), we multiply their Fourier transforms and return the inverse Fourier transformation (shown in black).

be obtained by taking the inverse Fourier transform of the products of the spectra in the frequency domain, as shown in Figure 7.8. That is,

$$\begin{aligned} \text{Image}_{\text{blur}}(x,y) &= \overline{\text{PSF}}(x,y) * \text{Image}(x,y) \\ &= \mathcal{F}^{-1}\left\{\mathcal{F}\left\{\overline{\text{PSF}}(x,y)\right\} \times \mathcal{F}\left\{\text{Image}(x,y)\right\}\right\} \end{aligned} \tag{7.3}$$

where $\mathcal{F}$ is the Fourier transform and $\mathcal{F}^{-1}$ is the inverse Fourier transform [34].

7.3 Results

We compile the results of simulating all of the corneas with pupil sizes of 2, 4 and 8 mm viewing both our test images in Section 8.7, and discuss the overall results in the following sections.

7.3.1 Snellen Eye Chart

As anticipated, the corneas have much better vision with small pupils than with large. The regular corneas (those without PRK, keratoconus or monocular diplopia) have excellent spectacle-corrected vision with no astigmatism even up to 8 mm; acuity is estimated to be between 20/10 and 20/40. The problem eyes have acute loss of contrast and acuity, sometimes even with small pupils. A telltale ghost image forms with our 8 mm monocular diplopia eye, situated about $\frac{4}{3}^{\circ}$ above the primary image. Overall acuity ranges at around 20/80 for the PRK and diplopic eye to worse than 20/160 for our keratoconic eye.

7.3.2 Outdoor Scene

The aberrations that we witnessed with the simulated Snellen chart were more mild than with our outdoor scene, since our scene did not have a comparable degree of contrast and sharp edges, and thus was more forgiving. In general, it was harder to differentiate the blur from different corneas, as the results all seemed to converge with large pupils. The most striking feature was the "muddying" of the scene, as everything in the interior of the tower blurred to a dark grey. The ghost image was not as distinct for the diplopic eye as it had been for our Snellen chart.

7.4 Conclusion

We presented a technique for the simulation of first-order visual acuity using a precomputed normalized point spread function of the eye. We utilized two sample input

images: a modified tumbling E Snellen chart with an astigmatic test fan, and a sample full-color outdoor scene. Our results showed a fair approximation of visual acuity, with expected increased blur and loss of contrast for larger pupils as peripheral aberrations became more dominant.

Chapter 8

Visualizations

> Never compare your results with those of other visualization techniques.
> — *Number 8 in "Fourteen ways to say nothing with scientific visualization" [31]*

> At the heart of quantitative reasoning is a single question: *Compared to what?* Small multiple designs, multivariate and data bountiful, answer directly by visually enforcing comparisons of changes, of the differences among objects, of the scope of alternatives. For a wide range of problems in data presentation, small multiples are the best design solution.
> — *Edward R. Tufte [104]*

These quotes capture the heart of this chapter. Our goal here is to "bring it on home", and display all twelve simulated and real corneas listed in Chapter 3 using (as a reference) every shape display technique in Section 2.1 and every acuity visualization method described in Chapters 5, 6, and 7.

Since there are too many corneas (12!) to view on a single page, we separate them into two classifications: six "regular" and six "problem" corneas. For each classification, we display all the corneas vertically and all the visualizations horizontally in *small multiples* [103] in a matrix. We then provide analysis, explaining interesting and revealing features of the data. The template for regular and problem corneas is shown in Tables 8.1

Regular corneas	Viz_1	Viz_2	$\cdots$	Viz_n
Sphere* (Sec. 3.2.1)				
Perfect Ellipsoid* (Sec. 3.2.4)			$\cdots$	
Ellipsoid Model of "Normal"* (Sec. 3.2.2)				
"Normal" (Sec. 3.4.1)				
Ellipsoid Model of Astigmatism* (Sec. 3.2.3)			$\cdots$	
Astigmatism (Sec. 3.4.2)				

Table 8.1: The template for visualizations of the regular corneas. The section in which each cornea is described is listed in parentheses. Viz_i stands for the ith Visualization of the series. The model corneas indicated by * are purely analytic and did not require fitting by our polynomial.

Problem corneas	Viz_1	Viz_2	$\cdots$	Viz_n
Model of PRK† (Sec. 3.3.1)			$\cdots$	
PRK (Sec. 3.4.3)				
Model of Keratoconus† (Sec. 3.3.2)			$\cdots$	
Keratoconus (Sec. 3.4.4)				
Model of Monocular diplopia* (Sec. 3.3.3)			$\cdots$	
Monocular diplopia (Sec. 3.4.5)				

Table 8.2: The template for visualizations of the problem corneas. The section in which each cornea is described is listed in parentheses. Viz_i stands for the ith Visualization of the series. The model corneas indicated by * are purely analytic and did not require fitting by our polynomial. Those corneas indicated by † were generated by sampling an analytic shape to derive a high density point cloud, which was then fit by our polynomial.

and 8.2.

The data range of the corneas is the domain $r < 4$ mm, and for these images we have sampled the corneas in a Cartesian grid at 20×20 resolution, generating 400 points. Roughly $\frac{\pi}{4}$ or 78% of those samples fall within our valid range. With our retinal representations, we use a sampling rate of 200×200 to compute our PSF.

The real data for the keratoconic, astigmatic and normal eye have some points on their periphery that the reconstruction process flags as unstable, so we remove them from computation. As a result, these corneas have a non-circular border.

Figure 8.1: Our quantized 8-level "hot" colormap: black → red → yellow → off-white.

8.1 Color Reproduction

There is a fair bit of image degradation with the color printing process. For many of the images in the simulation sections in this chapter, good reproduction is critical. As mentioned earlier, we provide online full-size copies of all color figures at the following web address: `http://www.cs.berkeley.edu/~ddgarcia/CWhatUC/` .

8.2 Colormaps

Each matrix element (a particular visualization of a particular cornea) will have its own independent colormap [31]. The color roughly corresponds to a "hot" color spectrum: black → red → yellow → off-white as shown in Figure 8.1. We choose bright green as the color for our overlaid vector fields, as it contrasts well with these colors. Since the values are auto-ranging, it is imperative the reader take careful note of the limits on the colorbars, as two visualizations which may seem to be the same might indeed be quite different.

The colormap will be quantized at eight regular increments to show contour lines of equal values. However, we do use a continuous rainbow colormap in Section 8.5 because we want to simultaneously illustrate mean sphere and retinal distance to the best focus. If we use our standard quantized colormap, the inherent contour lines overwhelm the retinal distance contours.

We believe the optimal way to visualize data is to use a single reference, fixed colormap with which all clinicians would be familiar. This eliminates the numerous calibration problem with auto-ranging maps. Environments like this are *data-centric*, in that it is the data the clinicians care most about, and the visualizations are simply different ways to inspect them.

This chapter is *visualization-centric*, in that our primary goal is to highlight our novel and revealing visualization techniques using our twelve model and real corneas simply as a reference. One reason we did not use a common colormap for each cornea is that sometimes our reconstructed data contains spurious values near the periphery where the fitting was least constrained. In addition, our representation often has questionable normal vectors in the center leading to unstable axial power calculations. The combination of these two sometimes leads to maps whose data ranges are quite extreme. If we choose the highest and lowest ranges for all the maps of a particular cornea and generate one common colormap, then the values from these spurious results lead to large ranges. This washes out all the other maps, losing information. With independent colormaps, the worst case is that only a single map is washed out.

8.3 Shape Representations

Regular Eyes

The shape representations for the regular eyes show that the first four eyes are roughly rotationally symmetric. The sphere has a constant curvature of 43.5 D everywhere, with zero cylinder (thus no vectors in the rightmost map), as it should. The perfect ellipsoid

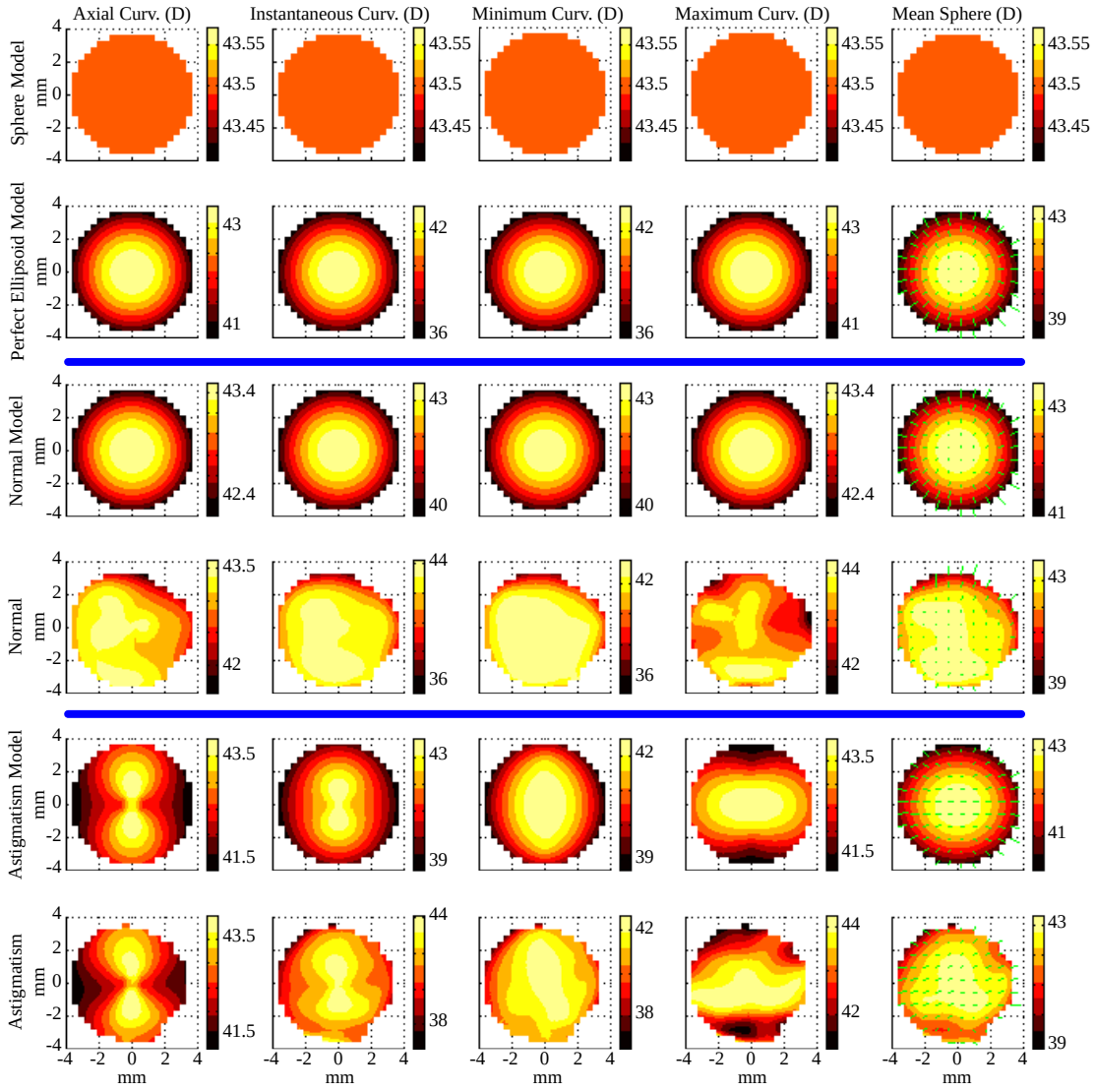

Figure 8.2: Shape representations for the six regular eyes. From left to right we display axial, instantaneous, minimum, and maximum power and mean sphere, all measured in diopters (D).

and normal model have exactly the same form, just with different values. They both have identical paraxial values, which is how they were defined. Ignoring the scale, it is quite interesting how similar all the curvature maps are for these two eyes. Our cylinder vector fields indicate that the minimum curvature direction always points away from the center. The normal eye has a paraxial curvature of 43.5 D, with no evidence of any astigmatism.

The astigmatic real and model cornea have almost identical axial curvature signatures. The figure-8 indicates that the 1.5 D of astigmatism is with-the-rule. Both eyes have horizontal paraxial minimum curvature vectors, supporting this assessment.

Problem Eyes

We know PRK is characterized by a flattening in the central zone as a result of the laser ablation. The two PRK eyes do exactly that, and in fact have almost identical mean sphere maps, except the curvature in our model's transition zone is about 5 D higher. The curvature field lines are mostly zero in the ablation zone but peripherally lie in the circumferential direction. The true ablation is a bit off-center to the left, which is captured by our model.

Keratoconus usually manifests itself as a region of locally high curvature, which is easiest seen in the mean sphere map. The "cone" in this particular data is rotationally symmetric, and minimum curvature lines flow away from its apex. Our polynomial representation does not fit acutely asymmetric shapes well, and we see that with the real keratoconus data. In the upper-right of our maximum curvature plot we see a tilted V-shaped region of high curvature and an inner region of low curvature. We believe this is purely a by-product of our limited surface constraints; other analyses of the same eye using

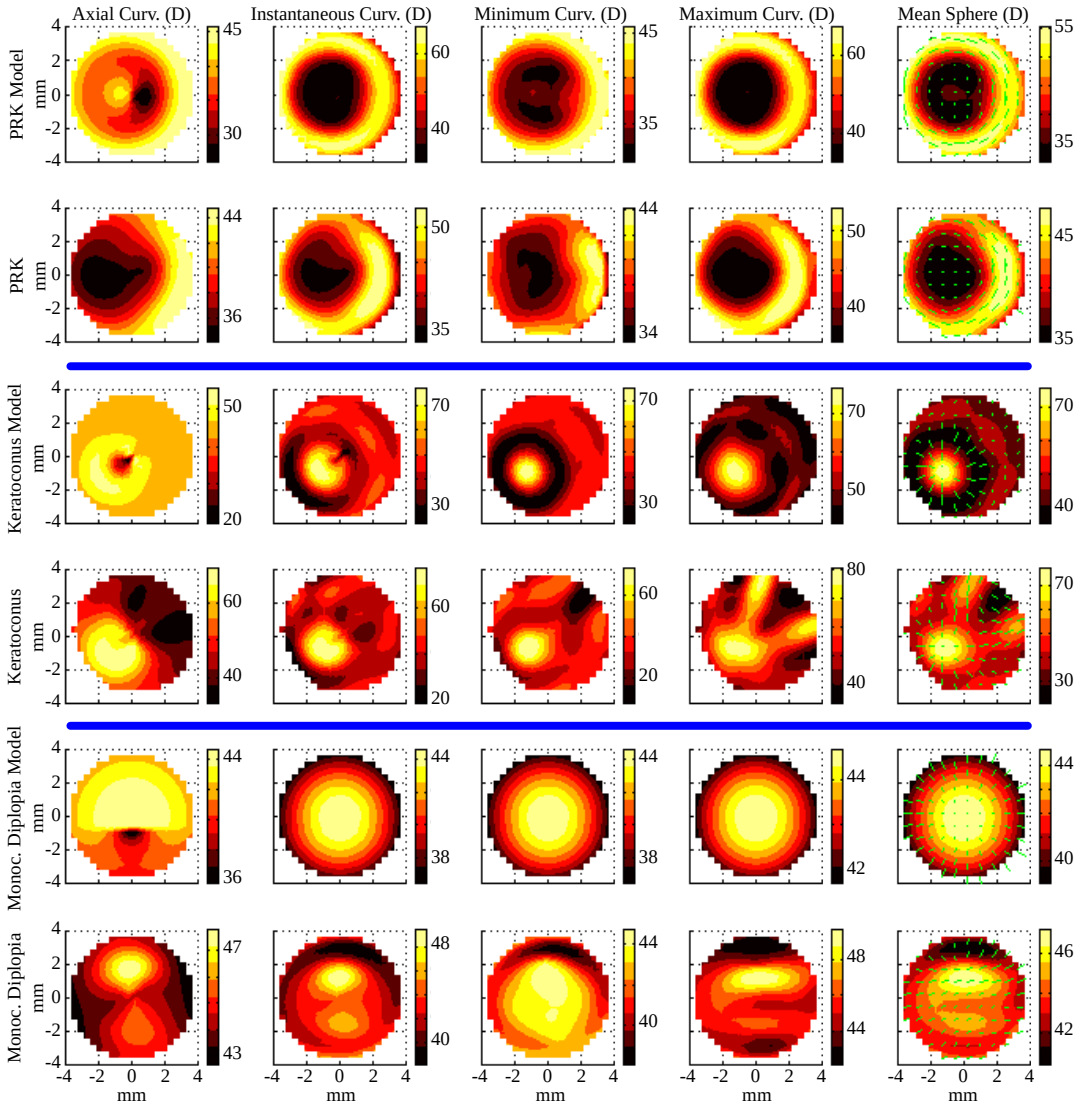

Figure 8.3: Shape representations for the six problem eyes. From left to right we display axial, instantaneous, minimum, and maximum power and mean sphere, all measured in diopters (D).

different representations do not have this anomaly. In addition, we have found that a poor fit results in an unstable central gradient. This affects our calculations of paraxial surface normals, which often produce incorrect (extreme high and low) results with axial-based calculations. We see this with the keratoconic eye model, whose paraxial axial curvature values swing wildly. These fitting issues will cause problems with our retinal representations, as we will see.

The parameters of the monocular diplopia model were not customized to match the real data's mean sphere, as the others were, but to simulate the dual focus retinal distribution. Thus, the actual shape is quite different and curvature calculations do not appear at all to match that of the real data. In fact, most of them look like the perfect ellipsoid from Figure 8.2; this is quite appropriate since we built our model out of two perfect ellipsoids, one central and one displaced.

The asymmetric figure-8 for the real diplopia tells us that the center of the data is not the region of highest curvature. We see this in our maximum curvature map, which has a steep wide region just above the center. It is interesting to note that none of the shape displays for the monocular diplopia data even hints that the corneas produce such unusual energy distributions on the retina.

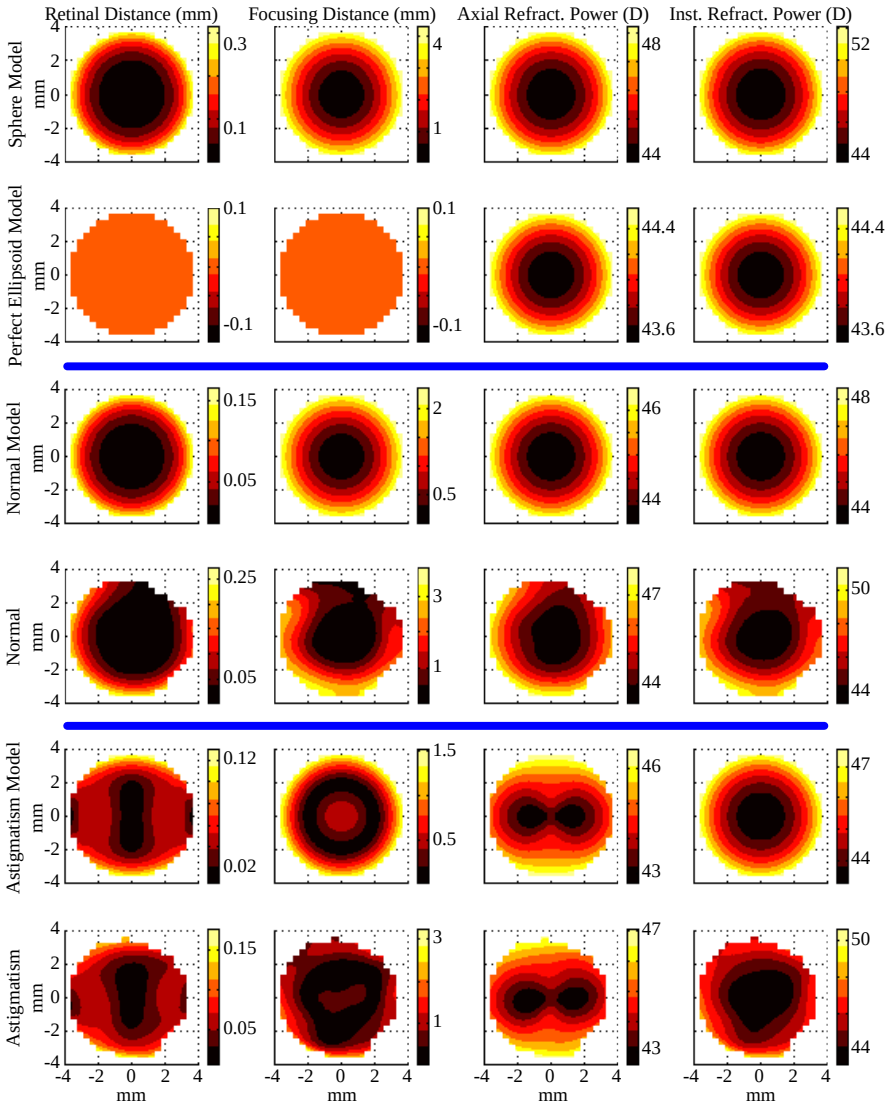

Figure 8.4: Corneal paraxial focus refractive power representations for our six regular eyes. From left to right is retinal and focusing distance (measured in mm), axial refractive power and instantaneous mean refractive power (measured in diopters).

8.4 Corneal Representations of Refractive Power

8.4.1 Refractive Power

Regular Eyes

The normal eye and its models are all rotationally symmetric, with the exception of the real data which extends its region of good focus upward. All the eyes focus well in the center, as measured by the retinal and focusing distance. The perfect ellipsoid has all light focus at one point, so it is no surprise that both distance calculations are zero.

The axial refractive power maps for the astigmatic eyes show the characteristic figure-8 pattern, but this time it is horizontally aligned; we saw this in Figure 5.3. It is important to note that the instantaneous mean refractive power does not have the classic figure-8 pattern of its curvature counterpart, even for asymmetric eyes like these. The retinal distance map for the model and real eye are surprisingly alike; we attribute this to careful parameter tweaking as well as a recognition that ellipsoid models capture the refractive power of regular eyes very well.

Problem Eyes

The retinal distance in the ablation zone for our PRK model is not as good as for the real eye. We attribute this to a poor fit since we modeled the central ablation zone with a sphere which should not have the crescent-shaped retinal distance feature. The rest of the representations for the PRK eyes have approximately the same characteristic shape, with the exception of axial refractive power. As mentioned in Section 8.3, we find that central axial curvature and refractive power calculations for corneas that are fit with our

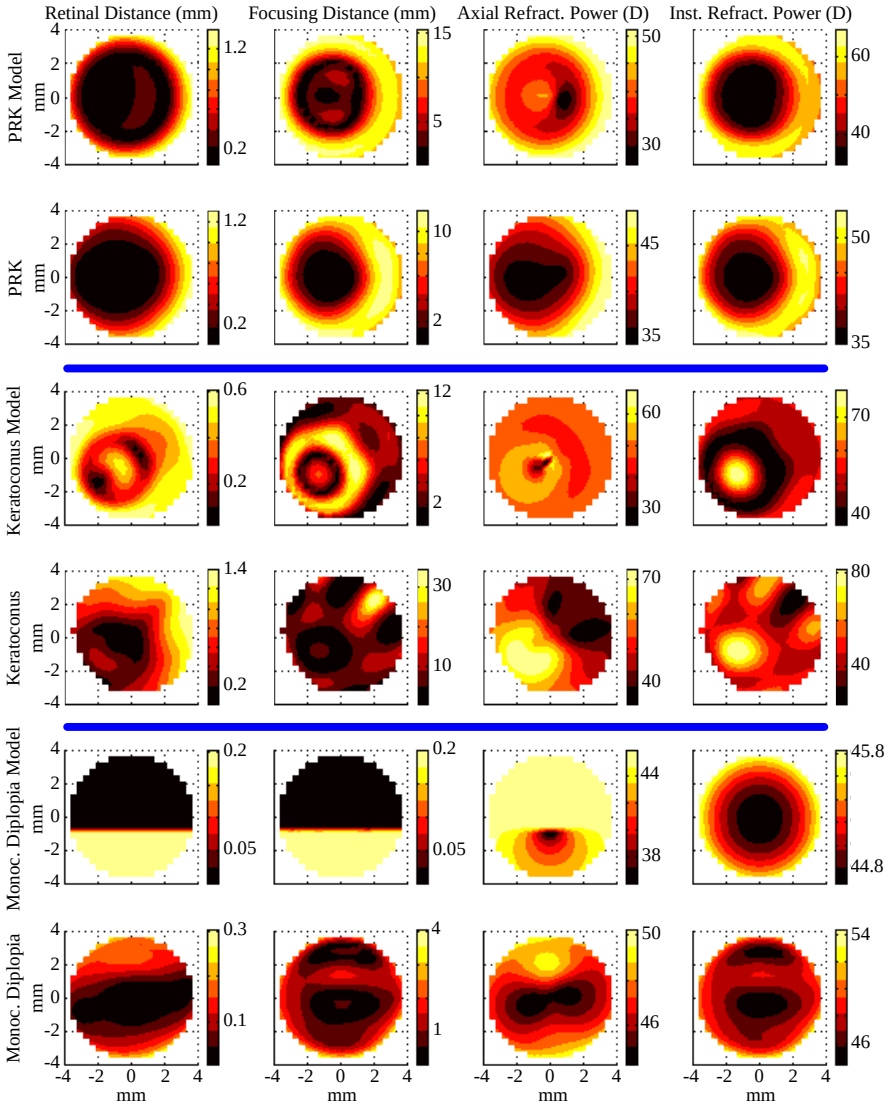

Figure 8.5: Corneal paraxial focus refractive power representations for our six problem eyes. From left to right is retinal and focusing distance (measured in mm), axial refractive power and instantaneous mean refractive power (measured in diopters).

polynomial are often not trustworthy; we will see this with both the PRK and keratoconus models.

The instantaneous map of the keratoconus model is quite similar to that of mean sphere from Figure 8.3. The extreme values in the retinal and focusing distance maps for both eyes is a hint that these eyes have poor optical acuity, since there is no large region of good focus (zero distance) as there is in all the other eyes. In fact, the only region of good focus for the model is the lower-right and upper-left, which are absent for small pupils. We expect to see extremely low Strehl_g ratios. This will be confirmed in Section 8.5.

Our model of monocular diplopia consists of two coincident perfect ellipsoids. The central one responsible for the primary focus has zero retinal and focusing distance measures, which we see in the upper region of the plots. The one responsible for the secondary focus converges all light to another point, which means it has constant non-zero retinal and focusing distance. The instantaneous map is similar to the curvature maps from Section 8.4 in that it conceals the bimodal refraction properties of the shape. The axial map would seem to indicate that the upper ellipsoid is constant, but as we see from the large color range and from Figure 8.4, its slight increase away from the center is hidden by the colormap quantization.

The most revealing map for the real monocular diplopia data is the focusing distance map, which shows us two large regions of good focus. The first is a large, flat oval in the center and the second is a flatter oval at the top. That the retinal distance is quite different for those two areas tells thus that these two regions focus to different places on the retina, approximately 0.2 mm apart. We will see exactly that with the 8 mm pupil in

Section 8.5.

8.4.2 Wavefront Angle and Height

Regular Eyes

If we examine the wavefront angle and height of the regular corneas, we see much the same as we saw with refractive power. The perfect ellipsoid wavefront is a plane wave, and its zero maps confirm that. For the other three normal eyes, these maps help illustrate clear spherical aberration, as the peripheral wavefront leads and is sloped more than our paraxial wavefront.

Since we correct for cylinder, our astigmatism wave angle maps are roughly symmetric, and our height maps show the wavefront ahead of our central reference ray vertically and trailing horizontally in a saddle shape.

Problem Eyes

The maps for the PRK eyes show that the ablation zone has a circular region of small angles, although much of the information may be washed out because of the large colormap ranges caused by peripheral values.

The keratoconus model has a tilted thin strip of low slope, and a wavefront which trails the central region in the periphery. The real keratoconus seems to have a central region of equal slope and a tilted wavefront which trails in the upper right and leads in the lower left.

The monocular diplopia model has zero angle and height for the principal ellipsoid and a constant, non-zero wave angle for the second ellipsoid. The wavefront height trails

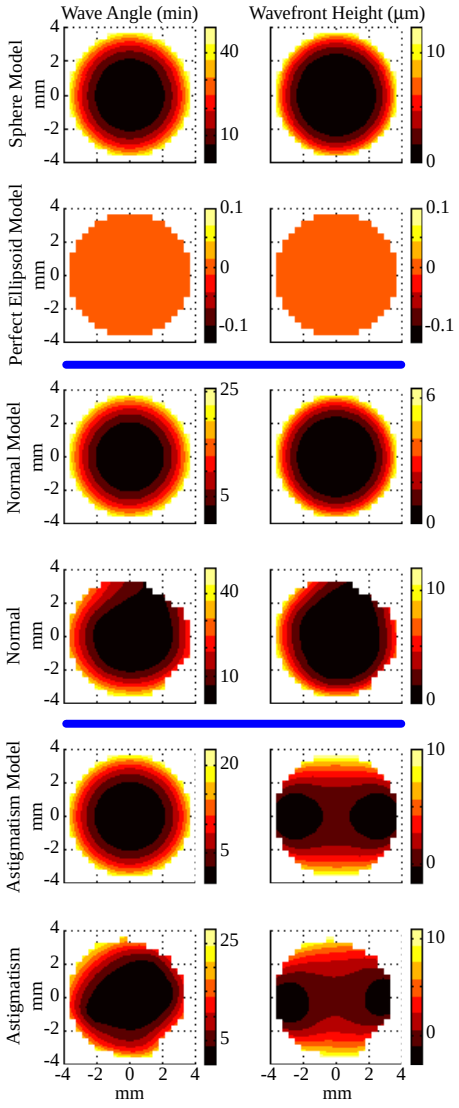

Figure 8.6: Corneal wavefront angle and height representations for our six regular eyes. The wavefront angle is measured in minutes and the height in microns.

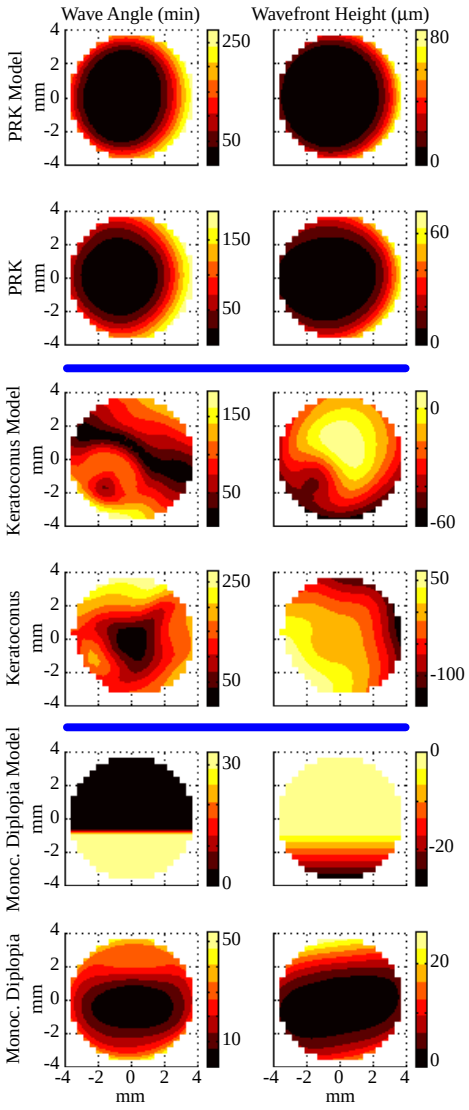

Figure 8.7: Corneal wavefront angle and height representations for our six problem eyes. The wavefront angle is measured in minutes and the height in microns.

away; adding prism to the shape creates a more vertically symmetric U-shaped (in height) map. The real data has a large oval region of low slope and low wavefront height, and values increase with vertical distance.

8.4.3 Wavefront Curvatures

Regular Eyes

Recall we calculate the wavefront by sending rays out from our best focus, refracting them out of the cornea and our cylindrical correction lens and determining where they lay on the entrance pupil in object space. We generate a point cloud and fit it as we would fit a cornea. This means that the problems of fitting we have seen for shapes is compounded twice! For this reason, it is best to take this class of visualizations with a "grain of salt".

Examining the wavefronts of the regular eyes, we see a plane wave with zero curvature for the perfect ellipsoid, as expected. The sphere and normal eyes show more curvature peripherally. The astigmatic eyes have a horizontal figure-8 axial and instantaneous signature, and interesting complementary minimum and maximum curvatures. The resulting mean sphere is almost circular.

Problem Eyes

The PRK eyes have the same form that we have seen already, low curvature in the middle and high in the periphery. The keratoconic eyes also have the same pattern that we have seen, but the axial power maps suffer from unstable central normals.

The poor fitting continues to plague the monocular diplopia model; it should be identical to the perfect ellipsoid in the upper-half of the map. However, in order to fit the

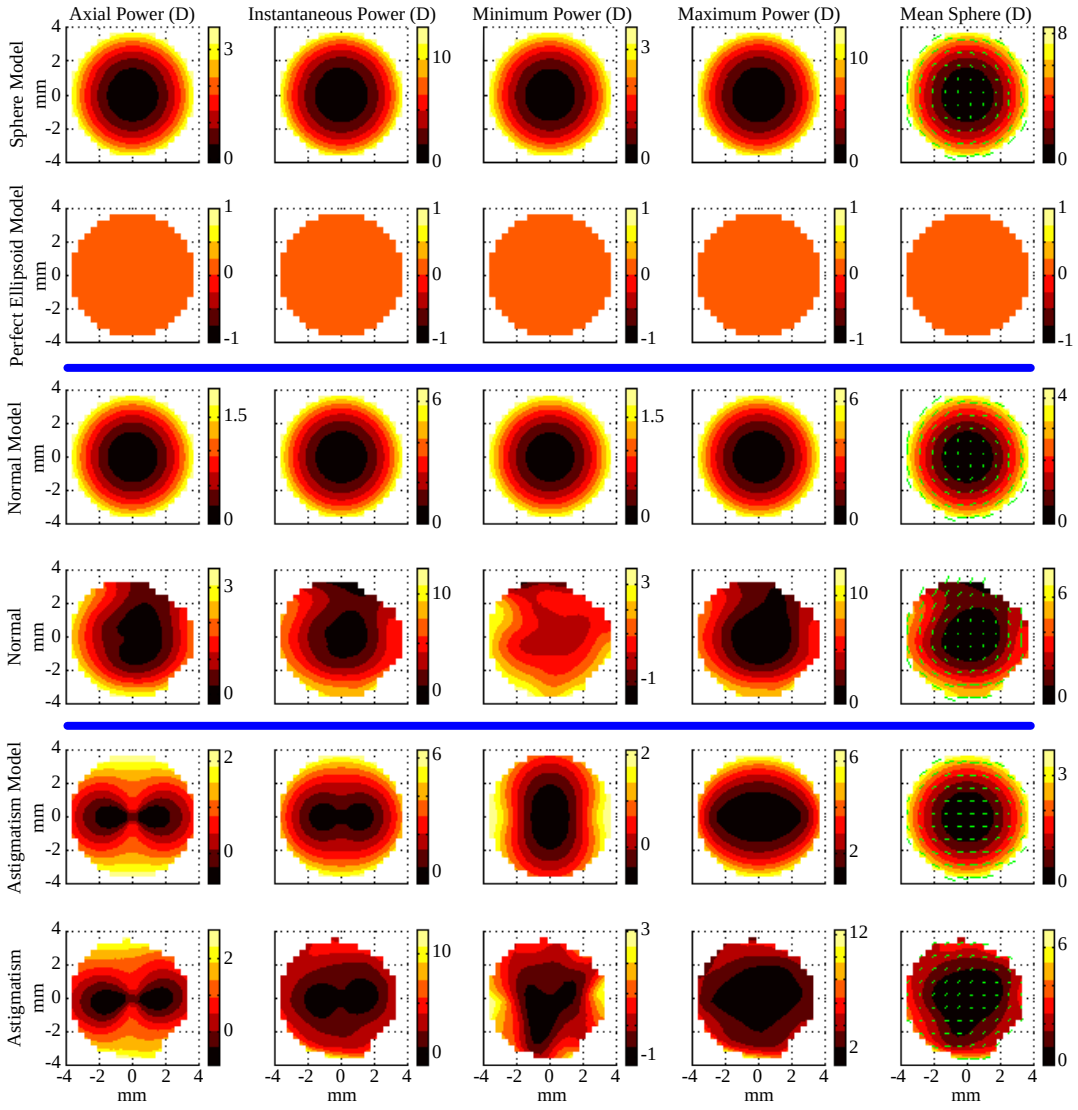

Figure 8.8: Corneal wavefront curvature representations for the six regular eyes. From left to right we display axial, instantaneous, minimum, and maximum power and mean sphere, all measured in diopters (D).

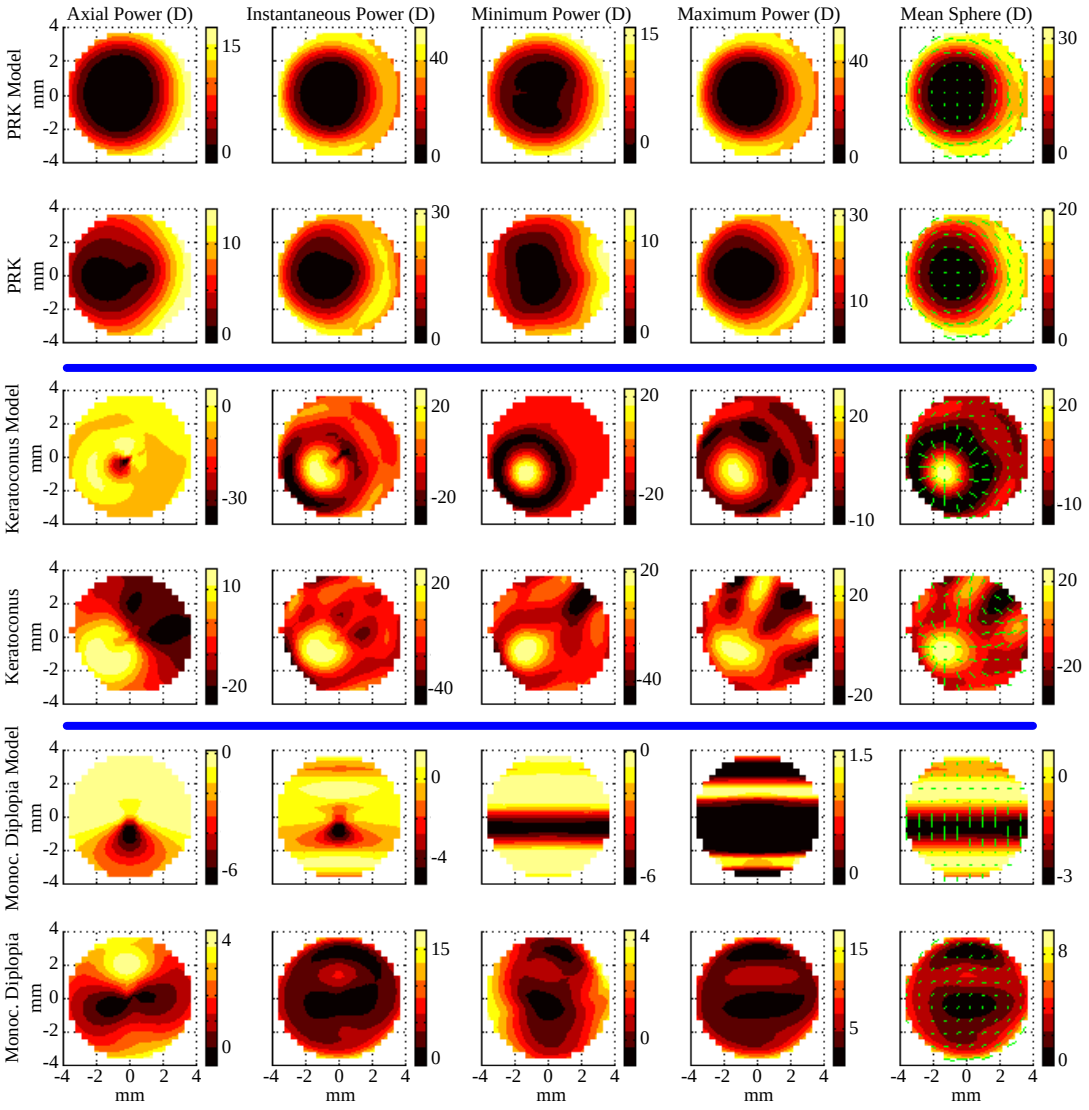

Figure 8.9: Corneal wavefront curvature representations for the six problem eyes. From left to right we display axial, instantaneous, minimum, and maximum power and mean sphere, all measured in diopters (D).

lower half, it has a horizontal wave of high curvature which is most evident in the max. power map. The real diplopia has two central regions of low wavefront curvature which correspond to the areas that generate the two foci.

8.5 Retinal Representations of Refractive Power

In these visualizations, we display the corneal PSF with 2, 4 and 8-minute contours alongside two views each of the two retinal representations, the $\overline{\text{PSF}}$ and MTF. We show these last two maps in three dimensions in addition to a top view of the $\overline{\text{PSF}}$ and a radially averaged cross-section of the MTF. We scaled the $\overline{\text{PSF}}$ by 100 so that its units are a percentage of all the rays; note that sometimes its distribution is so pencil-thin that it does not show up on the overhead view. We also squeeze its colormap down so that the entire map is defined between the range of [0, 0.03]. This is so that single stray rays show up brightly and can be counted; a linear colormap would mask this energy. Any peak higher than 0.03% will be given the colormap's maximum value, dark red.

We choose to keep the data in the same small multiple array for consistency; another solution would have been to cluster them by eye type and pupil size as in Table 8.3. This would have provided a more direct view of how the pupil parameter affected acuity, but would not have allowed the revealing cornea-to-cornea comparisons employed throughout this chapter.

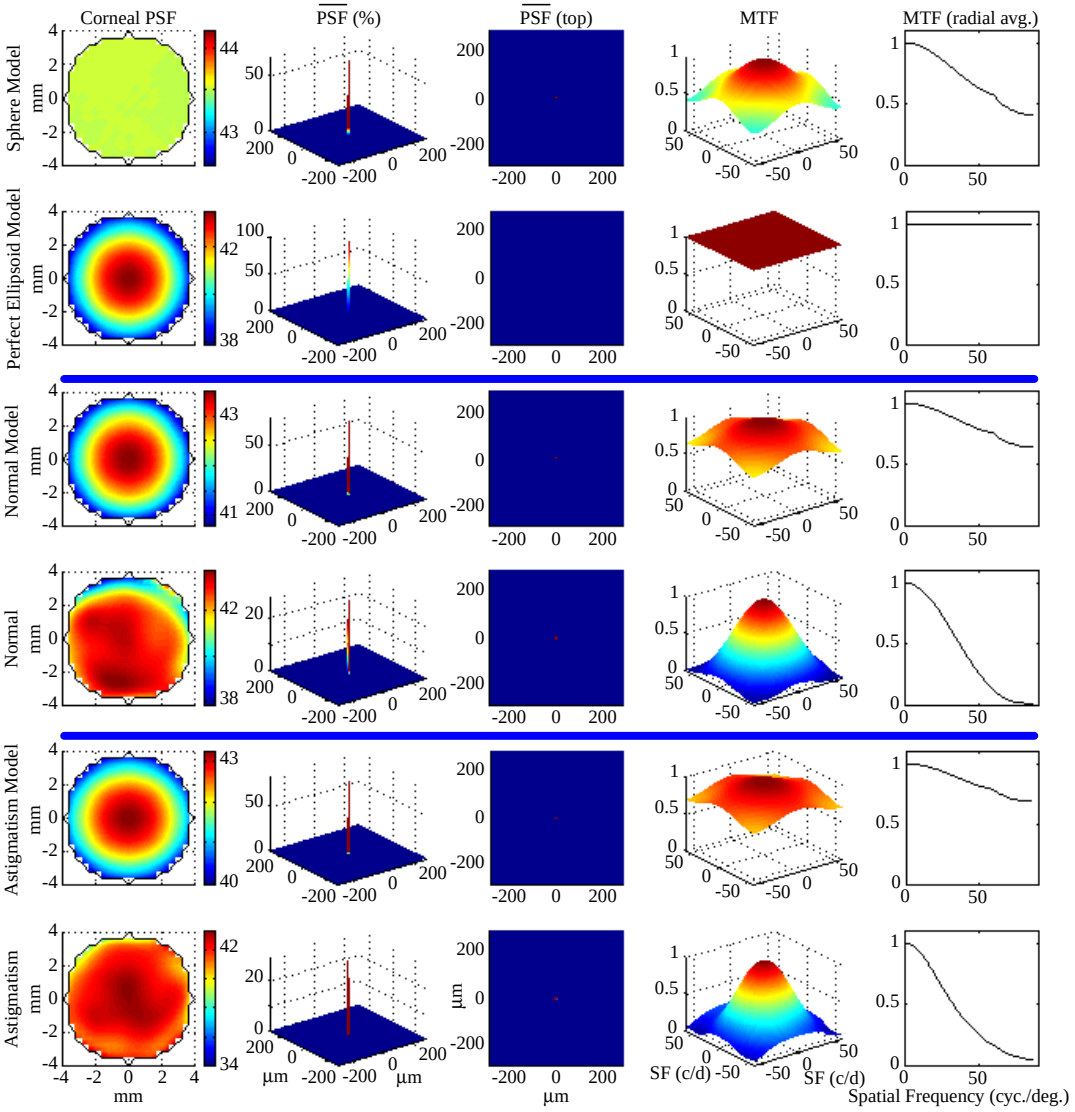

Figure 8.10: Retinal representations for the six regular eyes with a 2 mm pupil. The leftmost display is the corneal PSF in which the color represents mean sphere (measured in diopters) and the contour lines represent the 2, 4 and 8 minute distance to the best focus on the retina. The next two visualizations are a three dimensional and overhead view of the $\overline{\text{PSF}}$. The rightmost two representations are views of the MTF, one a three dimensional view and one a radial average about the center.

2 mm 4 mm 8 mm	Model of *Particular real cornea*
2 mm 4 mm 8 mm	*Particular real cornea*

Table 8.3: An alternate template for visualizations with varied sized pupils. This would allow analysis of how pupil size affected acuity, but would sacrifice consistency and would not provide immediate comparison with other corneas in the same classification.

8.5.1 2 mm Pupil

Regular Eyes

The corneal PSF for the sphere shows constant mean sphere and a very tight focus. Not surprisingly, there is an extremely good focus for all these eyes as evidenced by a tight $\overline{\text{PSF}}$ and an MTF that falls off very slowly. The second row perfect ellipsoid has an ideal $\overline{\text{PSF}}$ that is so pencil-thin that it is not even visible on the overhead view.

Problem Eyes

The model PRK has a focus that is quite a bit off-center, due to some central horizontal prism. The real PRK eye has a reasonable central peak, but a crescent-shaped area of focus on the corneal PSF. The keratoconus eyes have equally terrible $\overline{\text{PSF}}$ distributions, with coma-like tails that extend significantly away from the main focus. These are both due to central prism terms as well.

With the monocular diplopia model, we can see the beginnings of a second focus starting already. This is not really what happens with the true cornea which only has a small trace of a tail starting to appear. As we widen the pupil, we will see the $\overline{\text{PSF}}$ for

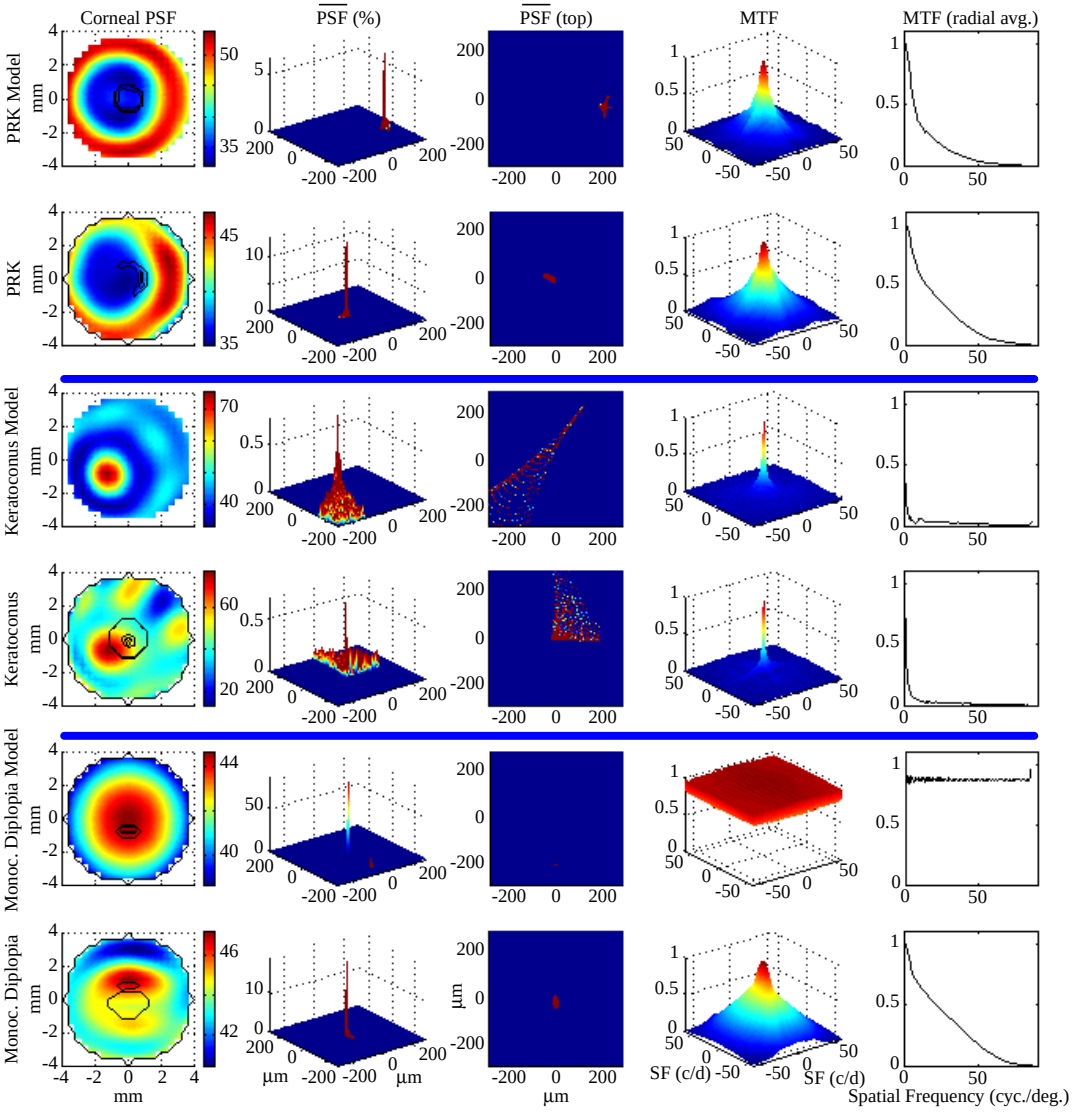

Figure 8.11: Retinal representations for the six problem eyes with a 2 mm pupil. The leftmost display is the corneal PSF in which the color represents mean sphere (measured in diopters) and the contour lines represent the 2, 4 and 8 minute distance to the best focus on the retina. The next two visualizations are a three dimensional and overhead view of the $\overline{\text{PSF}}$. The rightmost two representations are views of the MTF, one a three dimensional view and one a radial average about the center.

these eyes begin to look more similar.

8.5.2 4 mm Pupil

Regular Eyes

All of the eyes (except the perfect ellipsoid) have begun to show signs of spherical aberration, with $\overline{\text{PSF}}$s that have some quite evident spread. The MTFs have also begun to fall off more sharply.

Problem Eyes

The PRK eyes both have quite a bit of spread now, with coma effects taking energy from the central peak. The keratoconic eyes have the same problem, only worse, as their Strehl_g ratios barely exceed 0.5%. The monocular diplopia corneas are still quite different, with the second peak being quite evident with our model but only a large tail with the true cornea.

8.5.3 8 mm Pupil

Regular Eyes

Now the pupil is wide open, with a diameter of 8 mm. We see several interesting effects. The most glaring of which is that the perfect ellipsoid remains perfect. The sphere, normal and astigmatic model have different degrees of radially symmetric distributions. Recall that we apply a corrective cylinder lens, which is why the highly asymmetric astigmatism ellipsoid has a symmetric distribution. The shape of the corneal PSF contour lines

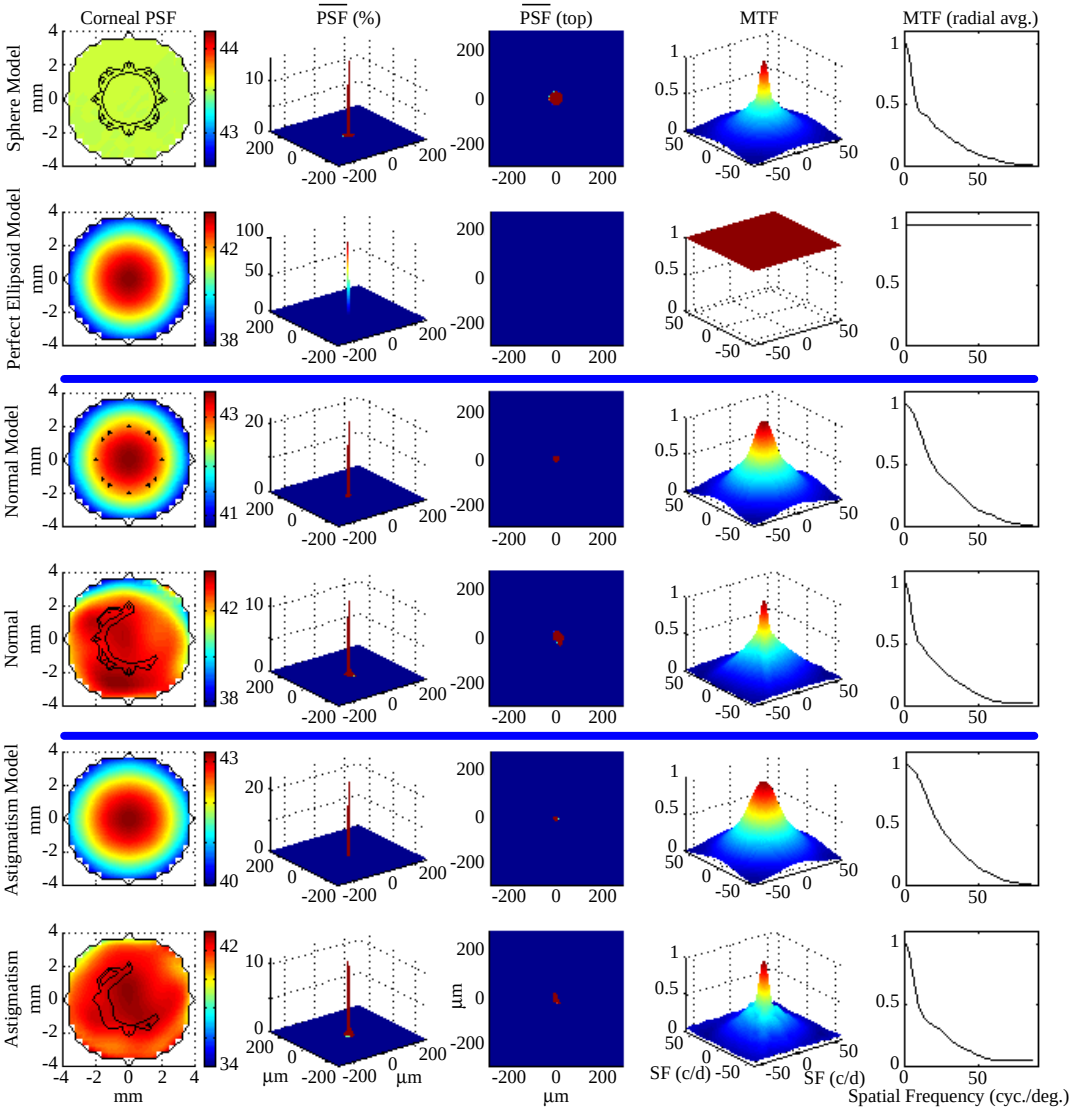

Figure 8.12: Retinal representations for the six regular eyes with a 4 mm pupil. The leftmost display is the corneal PSF in which the color represents mean sphere (measured in diopters) and the contour lines represent the 2, 4 and 8 minute distance to the best focus on the retina. The next two visualizations are a three dimensional and overhead view of the $\overline{\text{PSF}}$. The rightmost two representations are views of the MTF, one a three dimensional view and one a radial average about the center.

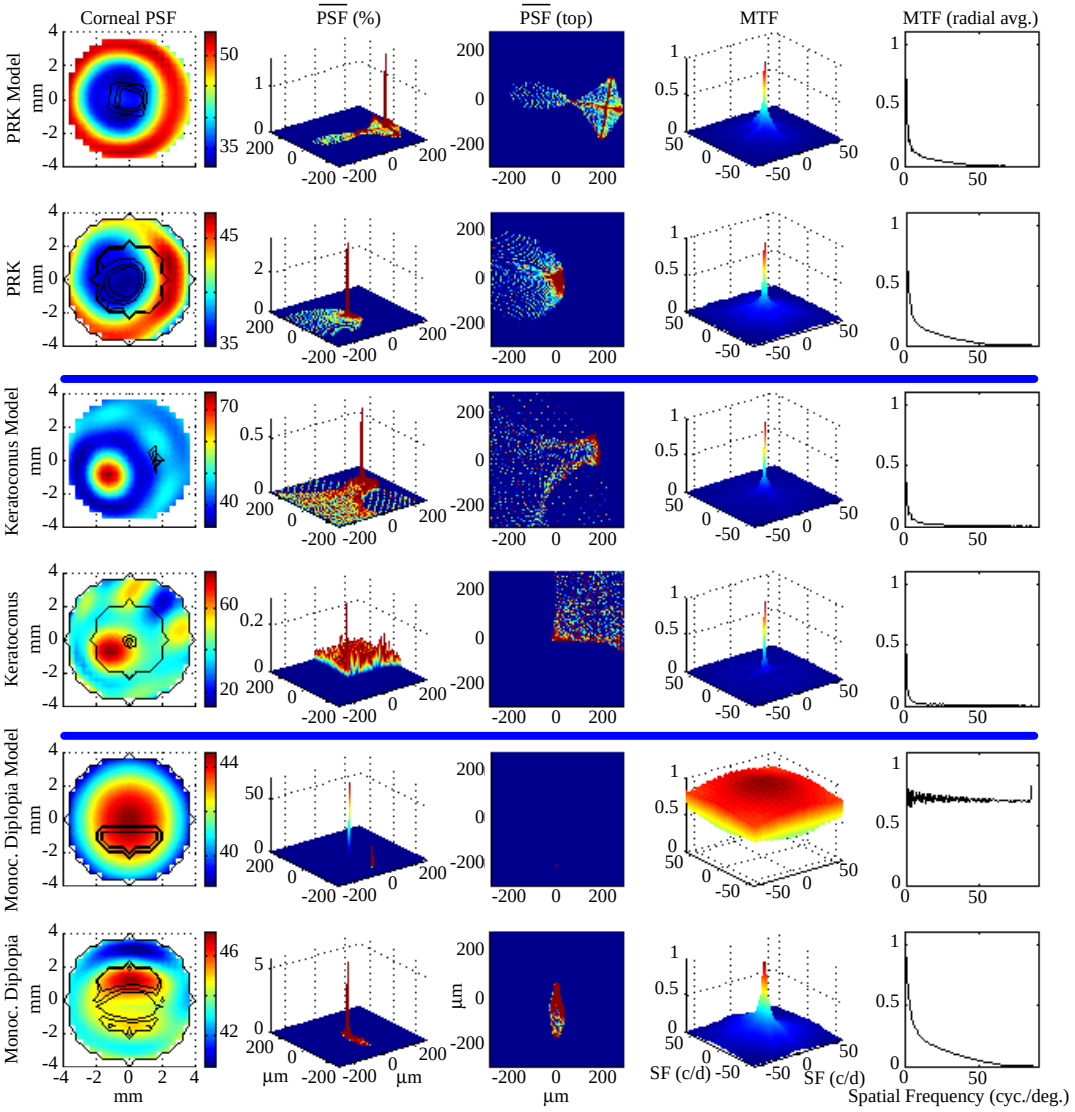

Figure 8.13: Retinal representations for the six problem eyes with a 4 mm pupil. The leftmost display is the corneal PSF in which the color represents mean sphere (measured in diopters) and the contour lines represent the 2, 4 and 8 minute distance to the best focus on the retina. The next two visualizations are a three dimensional and overhead view of the $\overline{\text{PSF}}$. The rightmost two representations are views of the MTF, one a three dimensional view and one a radial average about the center.

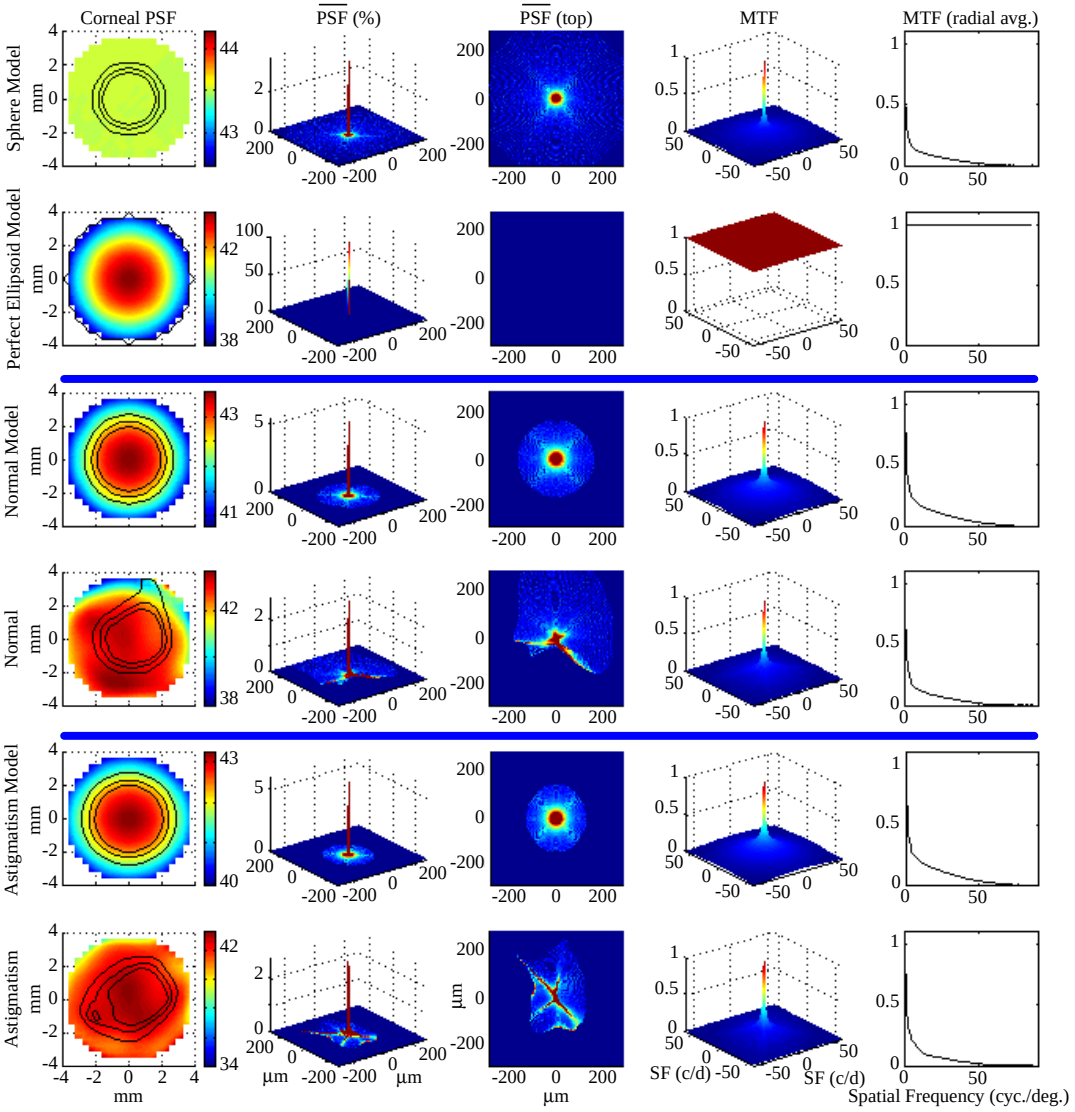

Figure 8.14: Retinal representations for the six regular eyes with an 8 mm pupil. The leftmost display is the corneal PSF in which the color represents mean sphere (measured in diopters) and the contour lines represent the 2, 4 and 8 minute distance to the best focus on the retina. The next two visualizations are a three dimensional and overhead view of the $\overline{\text{PSF}}$. The rightmost two representations are views of the MTF, one a three dimensional view and one a radial average about the center.

corresponds to the images we saw in Section 8.4. The $\overline{\text{PSF}}$ distribution has some spread in the upper area but not in the lower. The astigmatic real eye has an interesting fractal distribution, but still maintains a Strehl$_g$ ratio as good as the normal eye after sphero-cylindrical correction.

Problem Eyes

The $\overline{\text{PSF}}$ distributions are beginning to look very Jackson Pollock-esque, with light energy being splattered all about. Both the PRK corneas have a much smaller region of good focus than the regular eyes, with half the Strehl$_g$ ratios at 1%.

The keratoconus model shows something very curious. The best focus is generated by regions in the periphery of the cornea, nowhere near the cone. The $\overline{\text{PSF}}$ distribution is significantly scattered, and only 0.5% of all the rays contribute to the central peak. The real keratoconic eye has an acuity almost 10 times worse than the normal eye, with a Strehl$_g$ ratio of 0.2%. The area of the eye which contributes to the best focus is the flat peripheral area in the lower-right (with regard to the viewer).

The monocular diplopic model eye has two $\overline{\text{PSF}}$ peaks located in the same area as the real eye (one centrally, and one 0.2 mm below the other) and with the same relative strengths. The areas of good focus are the entire top half, which all focuses to the primary peak, and the entire bottom half, which all focuses to the secondary peak. We have seen and analyzed the corneal PSF and $\overline{\text{PSF}}$ for the true diplopic eye in Section 6.3.2; what is new here is the revealing overhead view of the $\overline{\text{PSF}}$ and the MTF.

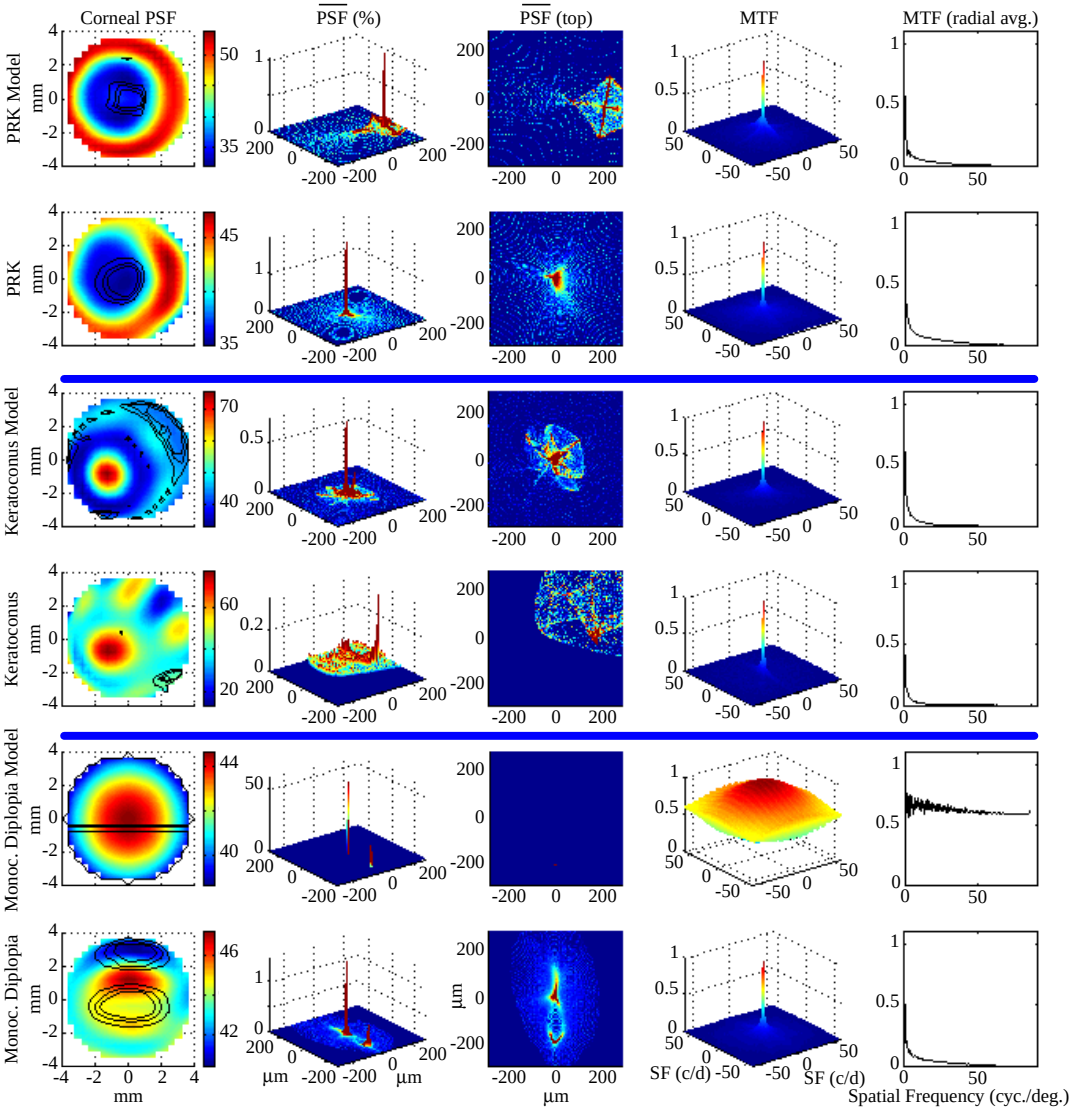

Figure 8.15: Retinal representations for the six problem eyes with an 8 mm pupil. The leftmost display is the corneal PSF in which the color represents mean sphere (measured in diopters) and the contour lines represent the 2, 4 and 8 minute distance to the best focus on the retina. The next two visualizations are a three dimensional and overhead view of the $\overline{\text{PSF}}$. The rightmost two representations are views of the MTF, one a three dimensional view and one a radial average about the center.

8.6 Eye Chart Simulation

We use as a reference a modified tumbling E chart with a fan test to measure acuity and residual astigmatism [10, 25] as mentioned in Section 7.2.3. The finest resolution E we use is 20/10, in which the level of detail (LOD) based on spacing between the lines in the E is 1/2 minute, the same as the $\overline{\text{PSF}}$ sampling. The Es tumble by 90° increments and increase in size up to 20/160 in which the LOD is 8 minutes. The fan test has 19 lines which are 40×1 minutes in size and positioned in 10° increments.

The original image can be seen by examining any of the perfect ellipsoid simulations, as this ideal optical system adds no distortion to its input. This is true for all three pupil sizes we consider. It is important to remember that all of the eyes have *best spectacle correction* applied for each pupil size, as described in Section 6.2.1. That is, we subtract away any astigmatism with simulated Jackson cross-cylinder lenses and move the retinal plane to find a best focus. This last operation is crucial in that it adds no spherical aberration to the system. Thus, as we will see, even the astigmatic eyes show no evidence of astigmatism in the fan test. We estimate acuity for the eyes by finding the largest E whose direction can be still be determined reliably. On the whole, any aberrations evident with small pupils increase in severity with larger pupils.

8.6.1 2 mm Pupil

Regular Eyes

The perfect ellipsoid produces aberration-free output, as expected. This is also true for the astigmatism and normal model. The sphere model has a small amount of blur,

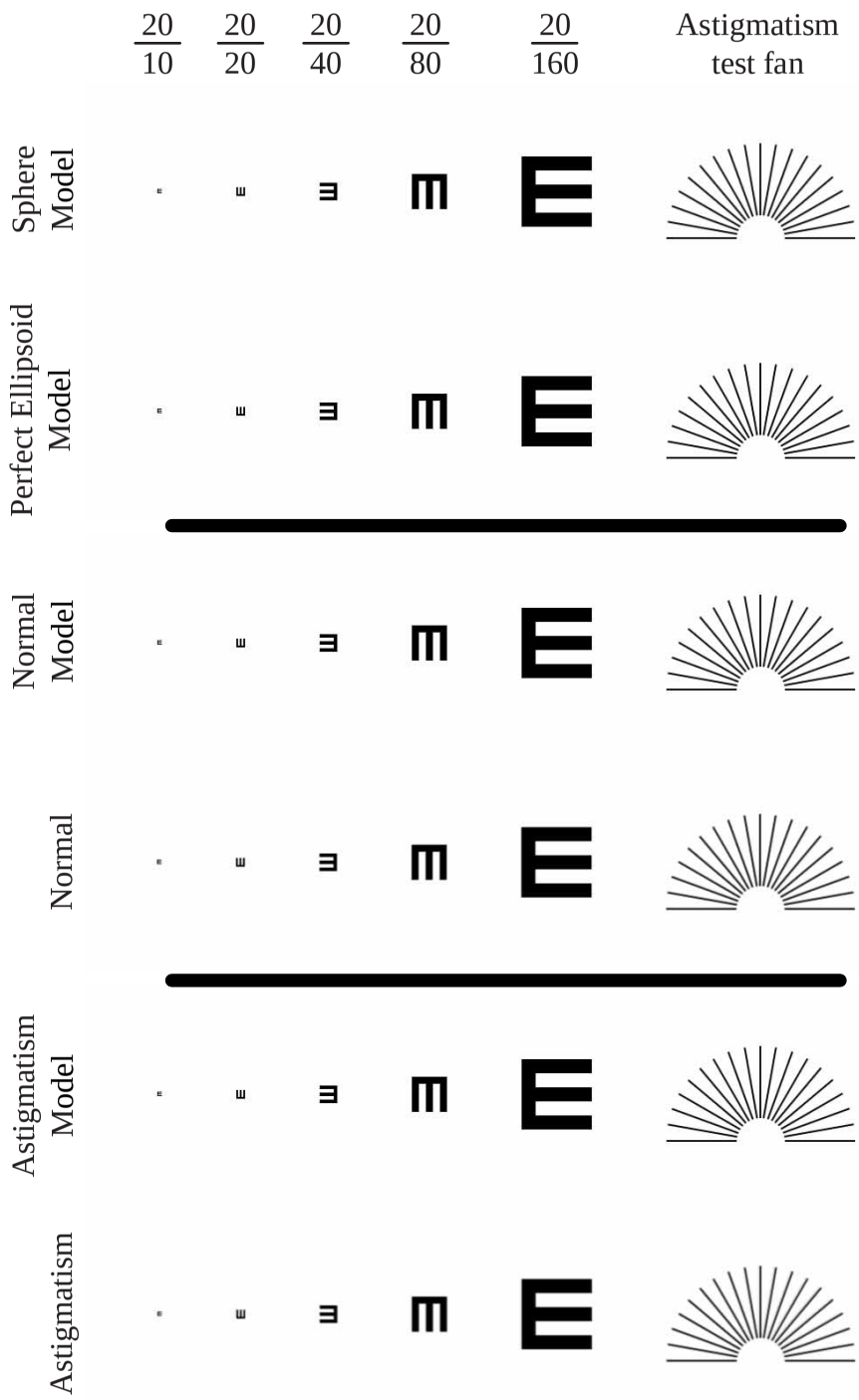

Figure 8.16: Representations of tumbling Es blurred as they would by the regular eyes with a 2 mm pupil. The size of the letters from left to right are: 20/10, 20/20, 20/40, 20/80 and 20/160. We also include a fan test for gauging astigmatism.

but the acuity is still virtually 20/10. The normal and astigmatic eye have the most blur, which probably brings them to 20/15. None of the eyes exhibits any noticeable astigmatism.

Problem Eyes

The PRK model eye, with its central prism, shifts the image to the right by about $\frac{4}{3}^\circ$ (the width of the 20/160 E). There is also some mild vertical and horizontal streaking, but acuity is roughly 20/20. The real PRK eye has a much smaller amount of coma, to the left and upper region; estimated acuity is 20/15 here.

The keratoconus model completely smears the image across the visual field; estimated acuity is extremely poor. We attribute this to significant prism and aberration due to the fitting, as we have mentioned. The real keratoconic eye has streaking downward and to the right with high loss of contrast. Acuity for this eye is estimated at 20/80.

The diplopia model creates a second perfectly focused second image that is $\frac{4}{3}^\circ$ above the first on the visual field, as we intended. This does not yet approach what happens with the real eye, whose vision is still quite good, with only a slight upward smear. The fan test confirms this, as the 90° ring is the clearest. Acuity for the model is 20/10 and about 20/15 for the real eye.

8.6.2 4 mm Pupil

Regular Eyes

The partial ordering of the eyes with regard to amount of blur remains the same as for the 2 mm case. The perfect ellipsoid is still aberration-free, followed by the astigmatism and normal model with equal amounts of mild blur. The sphere, normal eye and astigmatic

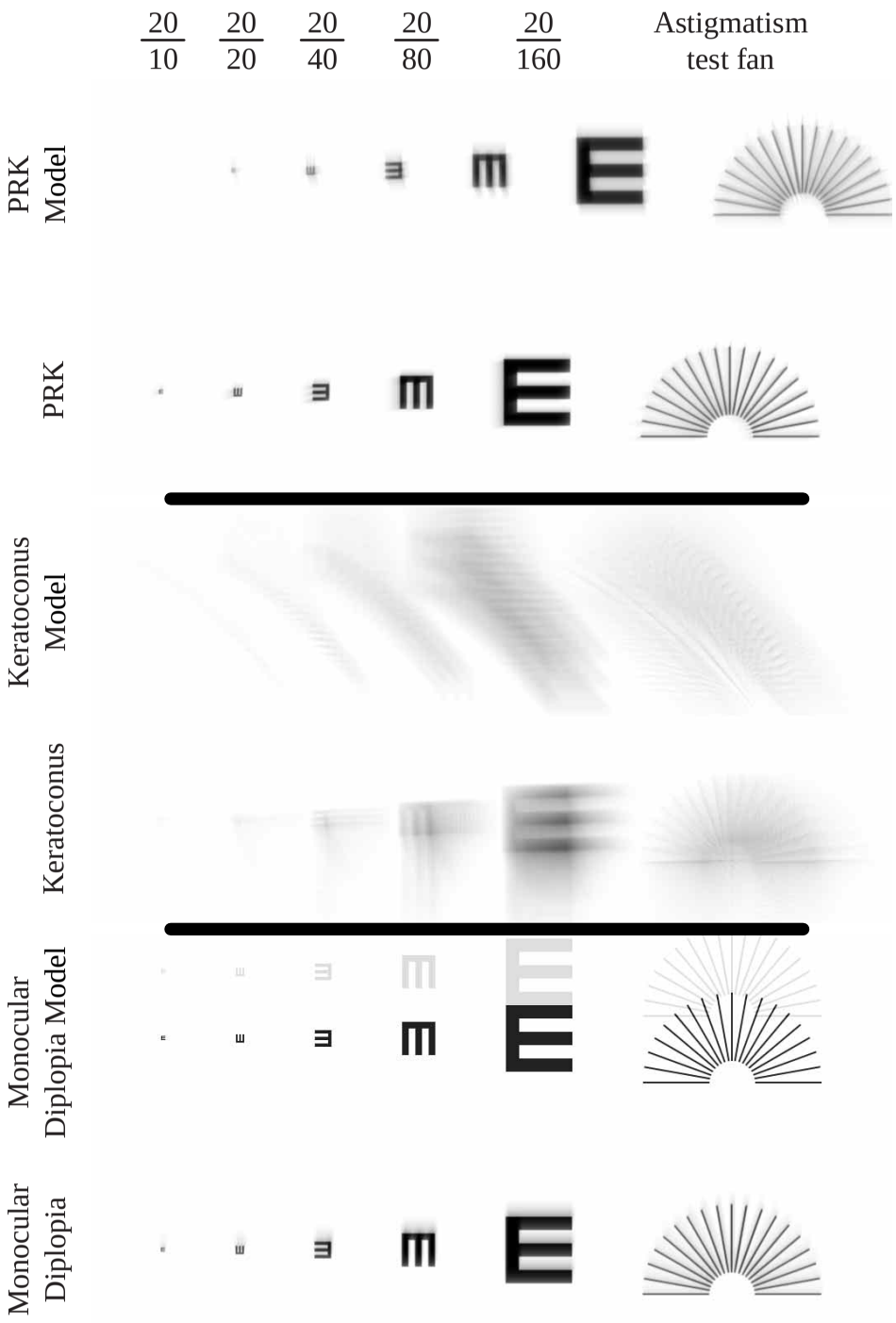

Figure 8.17: Representations of tumbling Es blurred as they would by the problem eyes with a 2 mm pupil. The size of the letters from left to right are: 20/10, 20/20, 20/40, 20/80 and 20/160. We also include a fan test for gauging astigmatism.

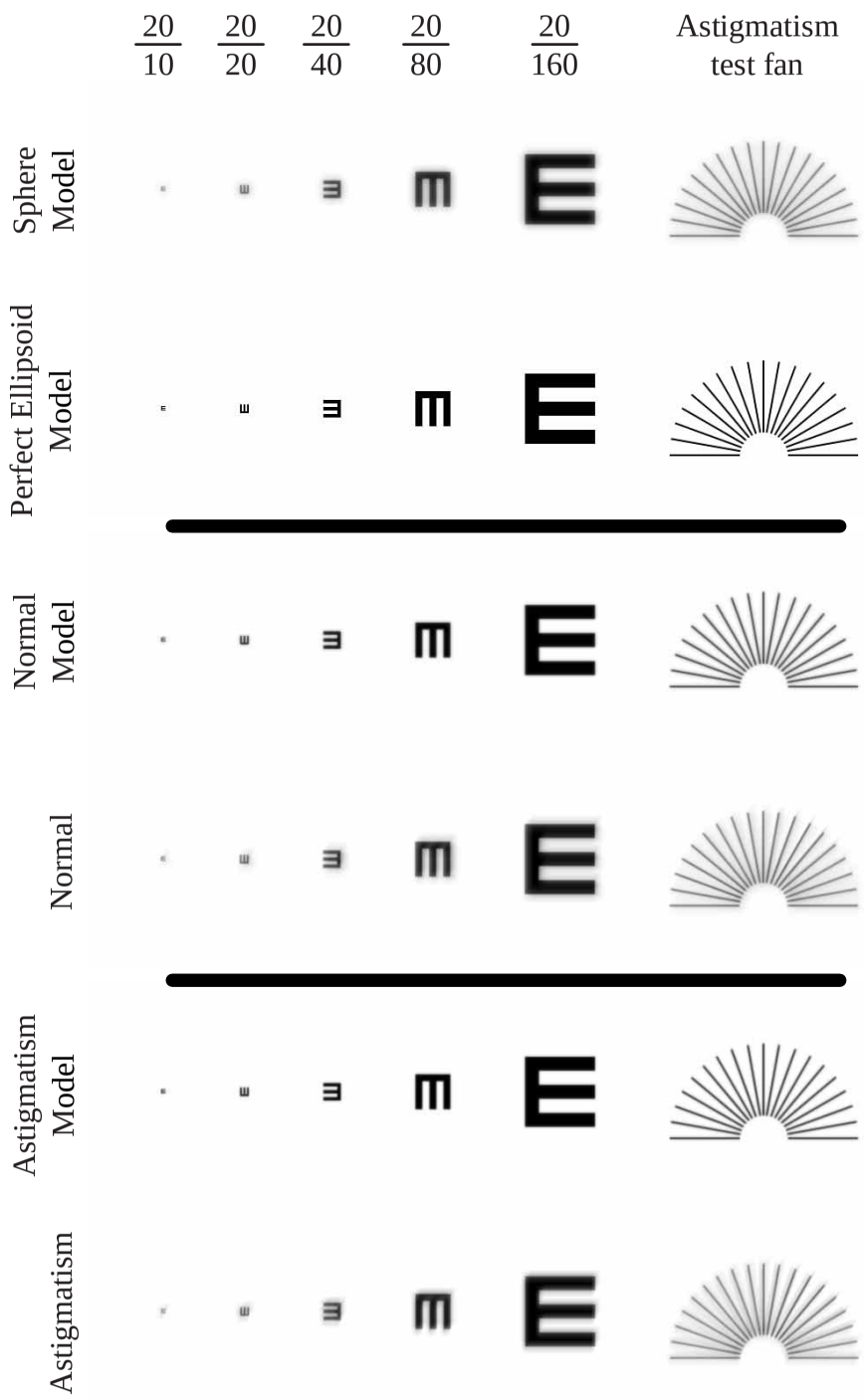

Figure 8.18: Representations of tumbling Es blurred as they would by the regular eyes with a 4 mm pupil. The size of the letters from left to right are: 20/10, 20/20, 20/40, 20/80 and 20/160. We also include a fan test for gauging astigmatism.

eye all show roughly similar amounts of slightly more blur. None of the eyes exhibits any noticeable astigmatism effects, and all have acuity at roughly 20/20 or better.

Problem Eyes

There is significant loss of contrast for the PRK eyes, with the same degradation we saw at 2 mm; acuity is reduced to 20/40. The keratoconic eyes continue to have extreme smearing and contrast loss; both have acuity worse than 20/160. The diplopic model has shifted more energy to its secondary image, which is darker than at 2 mm. The real diplopia has more vertical coma and loss of contrast, but acuity still remains at 20/20.

8.6.3 8 mm Pupil

Regular Eyes

All of the imperfect eyes have approximately equal blur effects. The real eyes have a touch more asymmetry, but on the whole, contrast is reduced and acuity falls in the range of 20/20 to 20/40 for all eyes.

Problem Eyes

The PRK eyes have more acute loss of contrast with acuity between 20/40 and 20/80. The keratoconic model eye has vision which actually improves at 8 mm! This tells us there are areas outside of 4 mm which contribute to the focus; we saw this in the corneal PSF maps. The keratoconic real eye still has acuity worse than 20/160.

Our patience has paid off with the monocular diplopia model. It now forms a quite good approximation to the real eye, with the ghost image situated directly over the

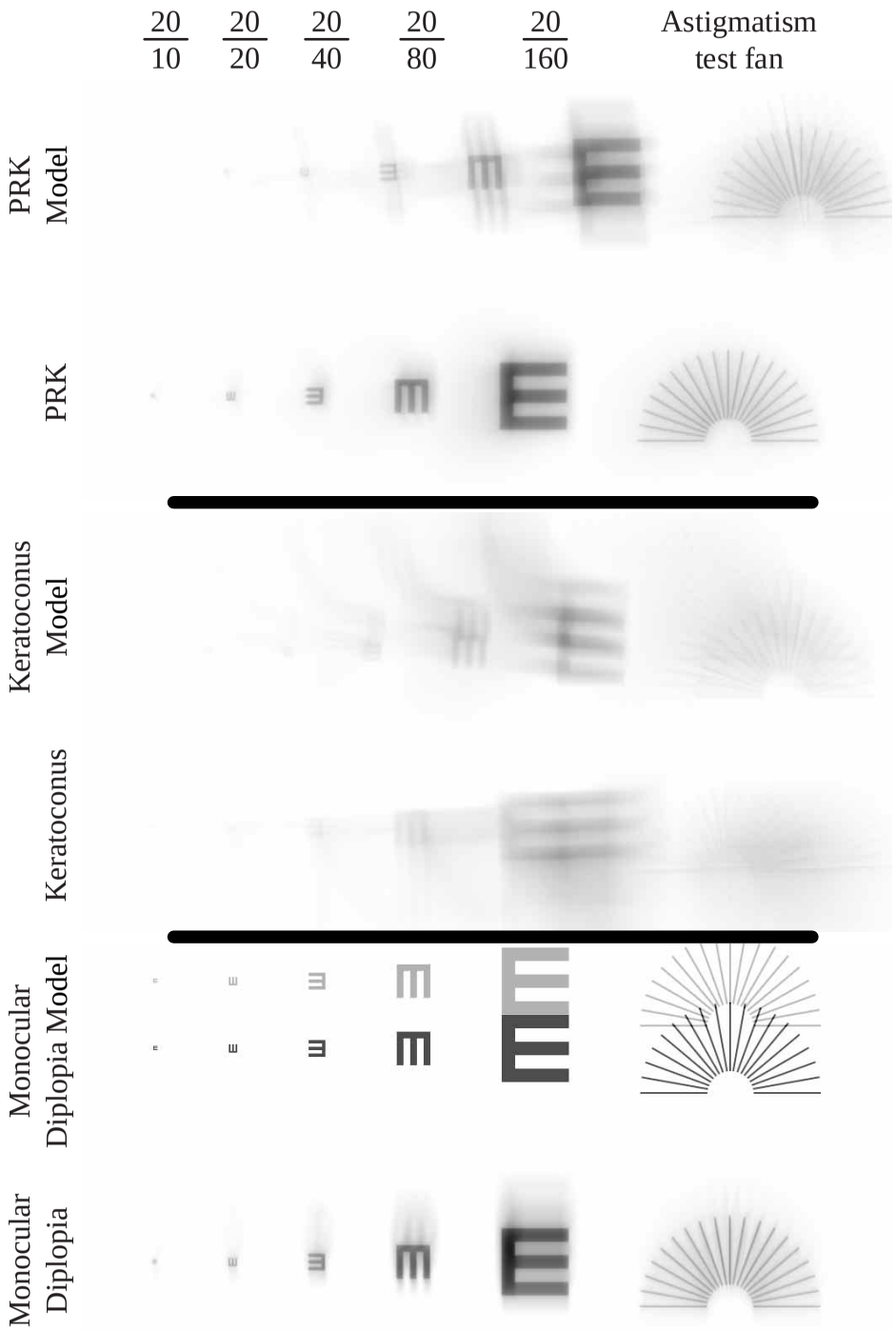

Figure 8.19: Representations of tumbling Es blurred as they would by the problem eyes with a 4 mm pupil. The size of the letters from left to right are: 20/10, 20/20, 20/40, 20/80 and 20/160. We also include a fan test for gauging astigmatism.

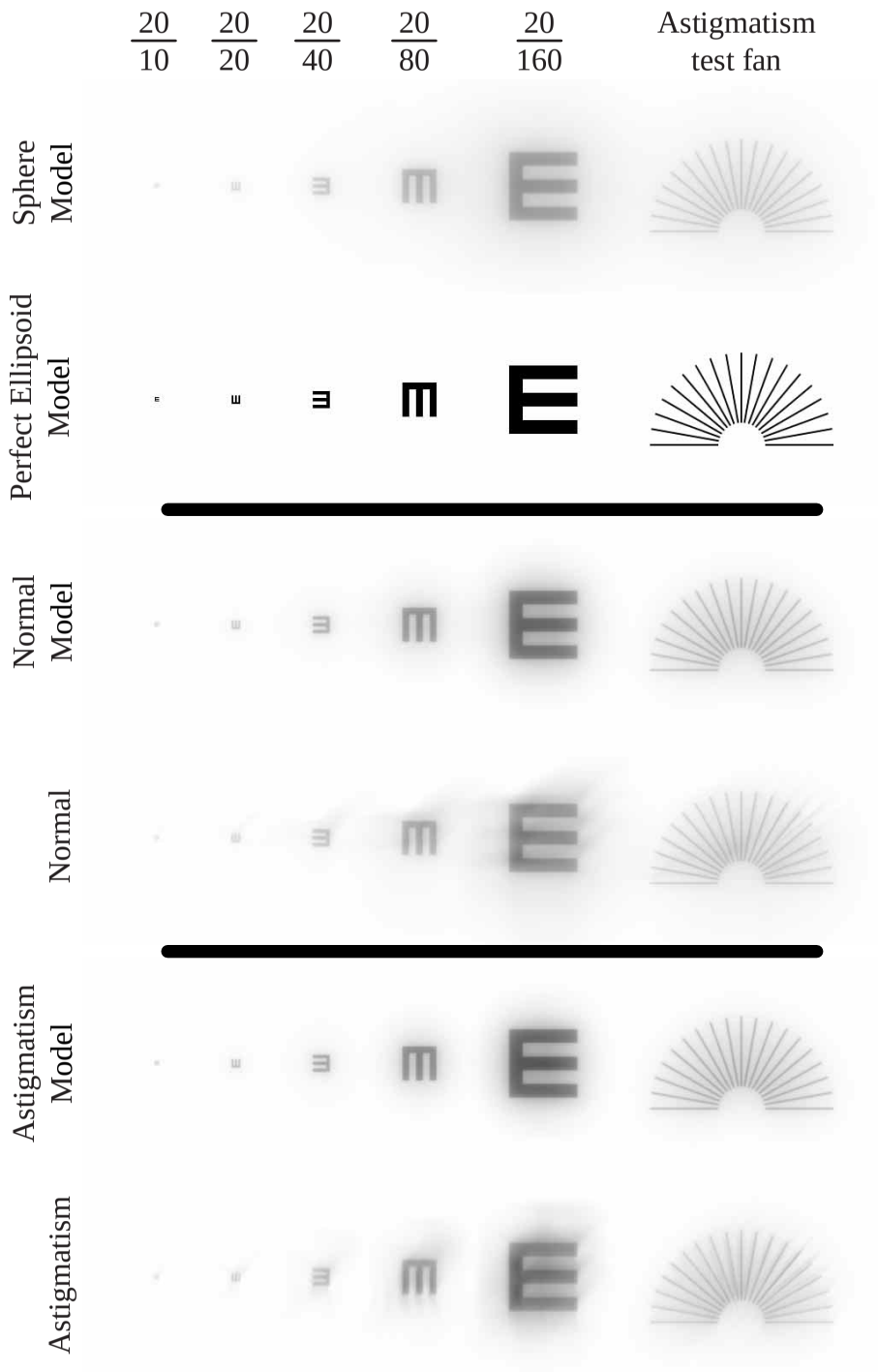

Figure 8.20: Representations of tumbling Es blurred as they would by the regular eyes with an 8 mm pupil. The size of the letters from left to right are: 20/10, 20/20, 20/40, 20/80 and 20/160. We also include a fan test for gauging astigmatism.

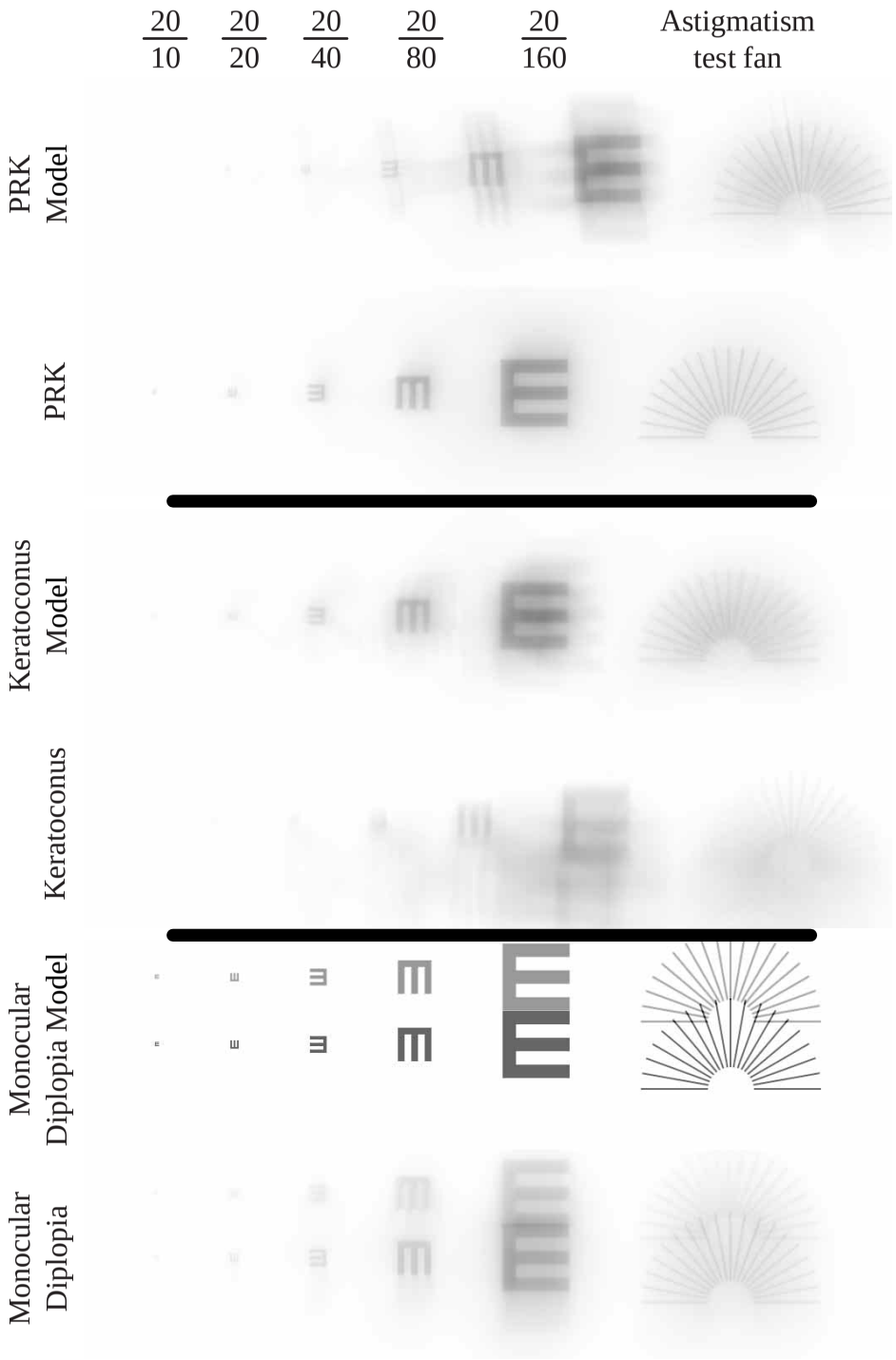

Figure 8.21: Representations of tumbling Es blurred as they would by the problem eyes with an 8 mm pupil. The size of the letters from left to right are: 20/10, 20/20, 20/40, 20/80 and 20/160. We also include a fan test for gauging astigmatism.

primary image, and with the same range of relative intensity. What differentiates the real eye is the slight blur and loss of contrast from the natural eye aberrations. Acuity for the model is 20/10 and around 20/80 for the patient.

8.7 Outdoor Scene Simulation

As discussed in Section 7.2.3, our image is a digitized photograph of U. C. Berkeley's Campanile tower, courtesy of Paul Debevec. Note that there is bound to be some image degradation in the printing process; full-color versions are available on the **CWhatUC** web site as mentioned in Section 8.1.

The aberrations that we saw in Section 8.6 are exactly reproduced here, even though this image does not have the degree of contrast. In addition, this image provides no immediate way to quantify aberrations, so our analysis in this section will be more brief. The perfect ellipsoid representation is an exact copy of the input, so it is useful to use as a reference.

8.7.1 2 mm Pupil

Regular Eyes

There is a small degree of blur from the real eyes, but it is hardly noticeable.

Problem Eyes

The PRK model blurs and shifts the tower to the right, and the real eye adds a small amount of blur. The keratoconus model smears the image to the point of unintelligi-

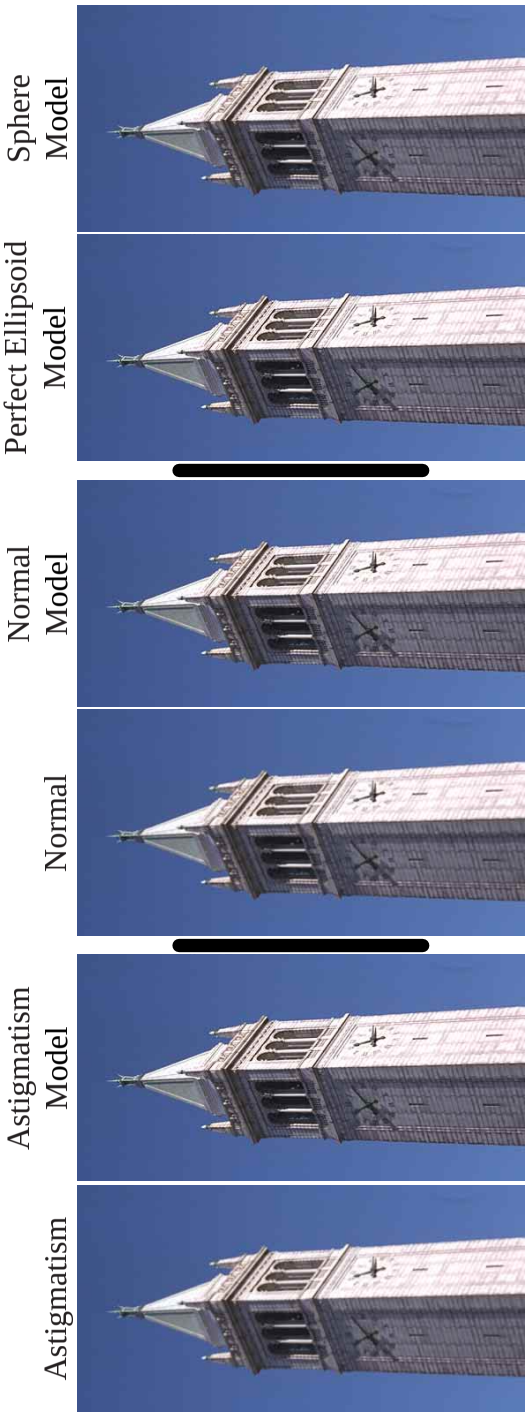

Figure 8.22: A representation of an outdoor scene blurred as it would by the regular eyes with a 2 mm pupil. Photograph of U. C. Berkeley's Campanile courtesy of Paul Debevec.

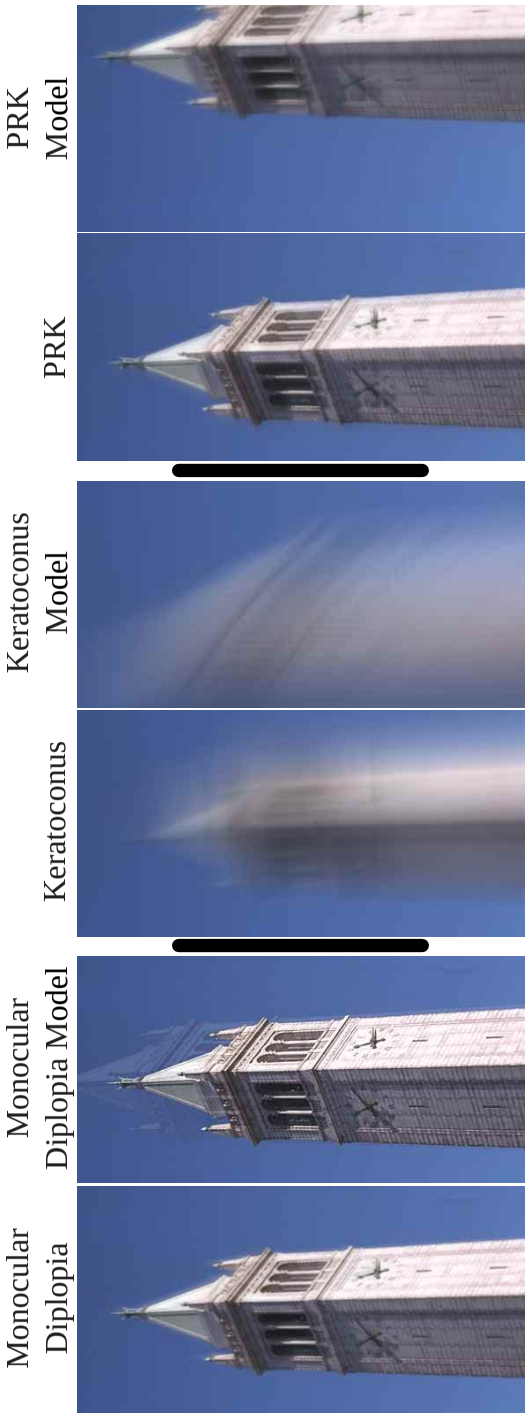

Figure 8.23: A representation of an outdoor scene blurred as it would by the problem eyes with a 2 mm pupil. Photograph of U. C. Berkeley's Campanile courtesy of Paul Debevec.

bility, whereas the real eye shows blur and loss of contrast. The diplopic model has a faint ghost image above the primary image, whereas the real diplopic eye simply blurs the tower slightly.

8.7.2 4 mm Pupil

Regular Eyes

No surprise here; the perfect ellipsoid is perfect, the real eyes and the sphere show the most blur, and the other models show somewhat less blur.

Problem Eyes

The PRK eyes have decreased contrast, the keratoconic eyes can hardly see the tower anymore, the diplopic model has a stronger ghost image and the real diplopia has more haze and coma.

8.7.3 8 mm Pupil

Regular Eyes

The imperfect eyes all look very similar, with apparently equal amounts of haze and blur.

Problem Eyes

As with the regular eyes, the blur induced by all the eyes is much harder to distinguish. Of the PRK and keratoconics, the real keratoconic eye appears to have the worst vision. The real and model diplopia have similarly placed ghost images, but the

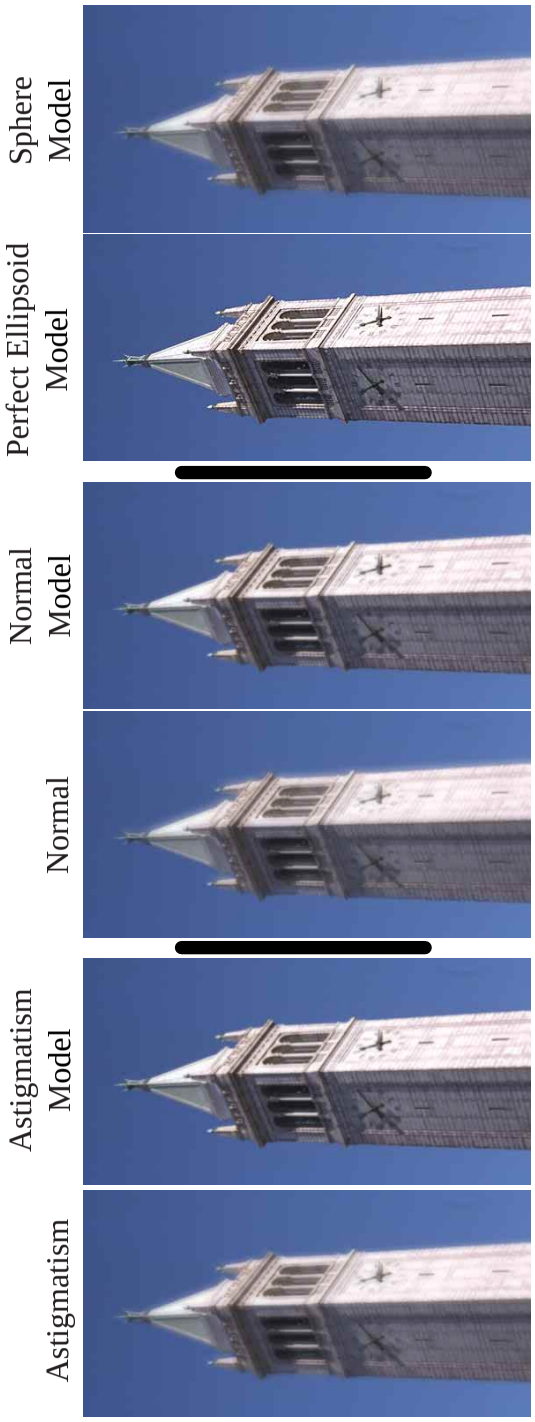

Figure 8.24: A representation of an outdoor scene blurred as it would by the regular eyes with a 4 mm pupil. Photograph of U. C. Berkeley's Campanile courtesy of Paul Debevec.

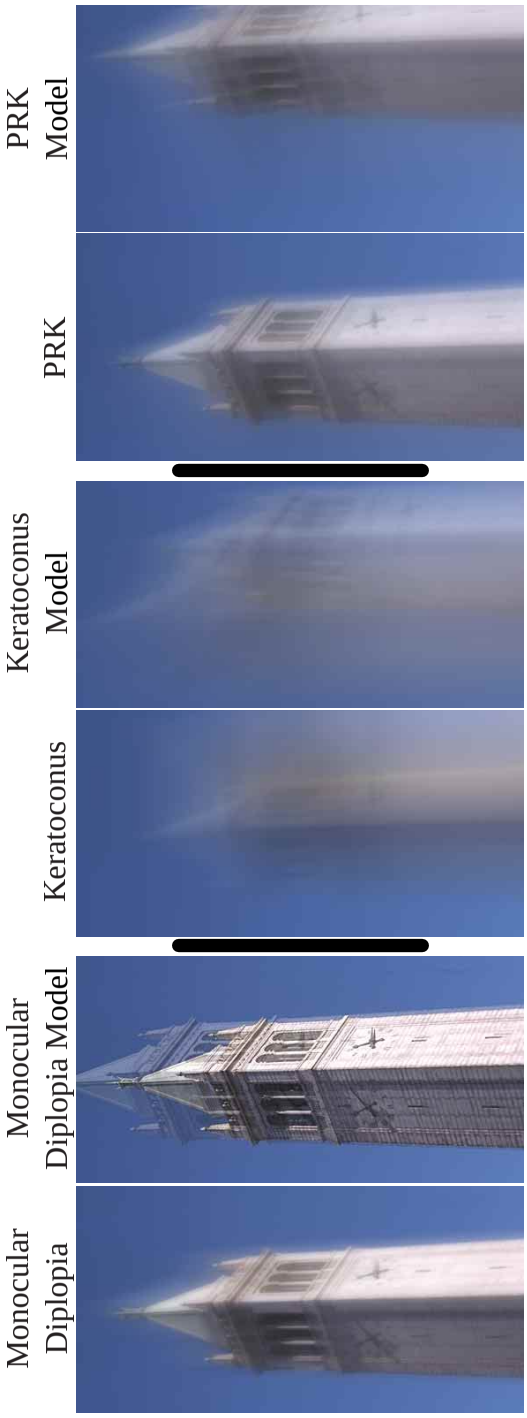

Figure 8.25: A representation of an outdoor scene blurred as it would by the problem eyes with a 4 mm pupil. Photograph of U. C. Berkeley's Campanile courtesy of Paul Debevec.

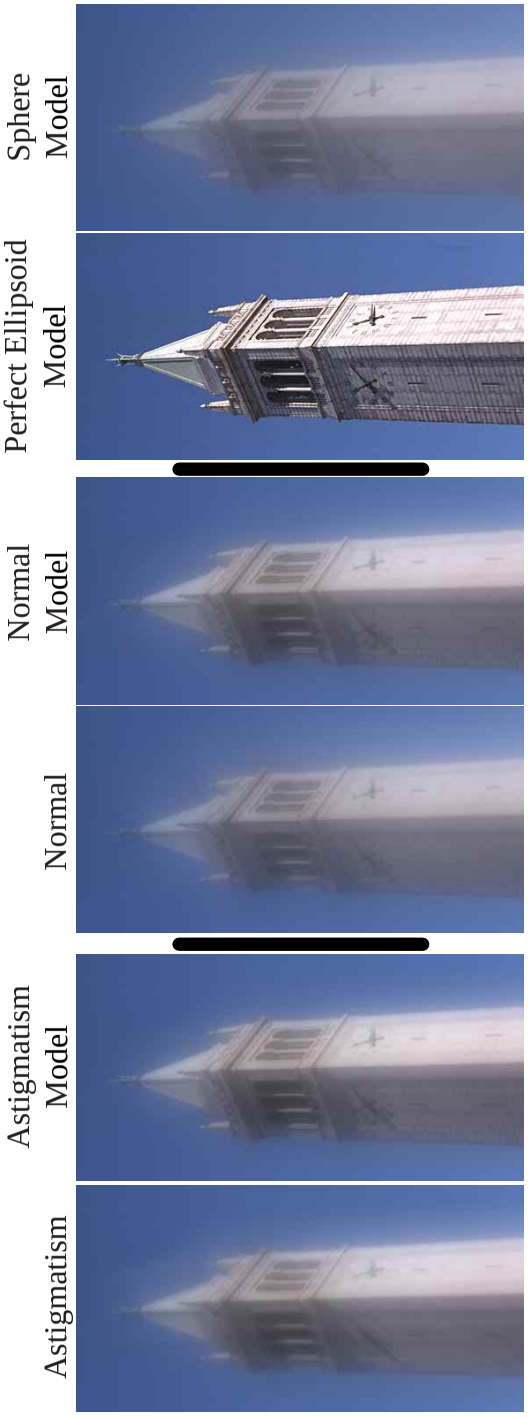

Figure 8.26: A representation of an outdoor scene blurred as it would by the regular eyes with an 8 mm pupil. Photograph of U. C. Berkeley's Campanile courtesy of Paul Debevec.

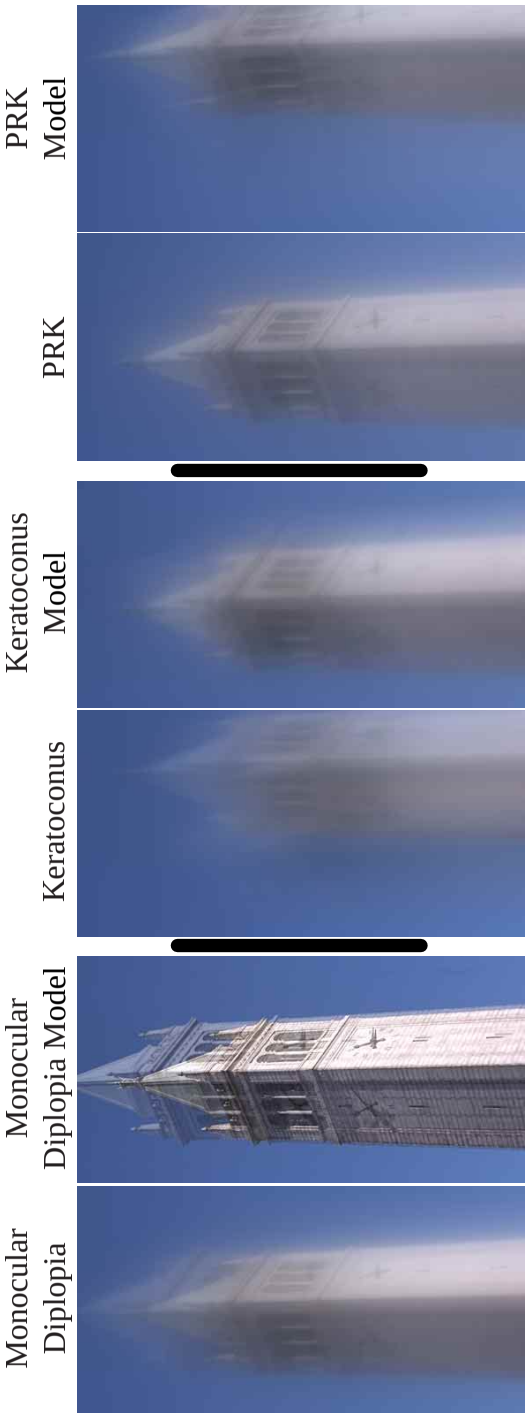

Figure 8.27: A representation of an outdoor scene blurred as it would by the problem eyes with an 8 mm pupil. Photograph of U. C. Berkeley's Campanile courtesy of Paul Debevec.

model's image is crisp, whereas the real eye's image is blurred, with significant contrast loss.

Chapter 9

Conclusion

In this dissertation, we presented **CWhatUC**, a collection of software tools that operate on reconstructed and simulated corneas. The software employs novel metrics for evaluating acuity based in fundamentals of wave optics and ray tracing. The three major contributions of this work are in prediction, visualization and simulation of the corneal contribution to visual acuity.

9.1 Prediction

Existing metrics for prediction of visual acuity often fail for patients who have undergone the refractive surgeries PRK and PARK. High contrast visual acuity (HCVA), for most of them, is quite good, and is the selling point most surgeons advertise. However, low contrast visual acuity is a much truer metric, since glare due to peripheral aberrations is often not measured when the pupil is small in HCVA tests. The acuity indices provided by existing corneal topographers are not a good predictor for this cross-section of patients.

Our contribution is a new metric, *wavefront coherence area*, which we show had much better correlation for the 62 test eyes, and thus is very promising as a predictor of low-contrast visual acuity.

9.2 Visualization

We presented five novel visualizations which can help clinicians evaluate corneal visual acuity performance. Four are considered *corneal* representations: *axial refractive power*, *instantaneous mean refractive power*, *focusing distance* and *retinal distance*. They pseudo-color the cornea based on the various refractive error metrics. The fifth, *Corneal PSF*, is a very revealing *retinal* representation which provides a tool for connecting which areas of the cornea are contributing to the best focus, as well as how tight that focus is. We showed how effective it was for determining the cause of monocular diplopia.

9.3 Simulation

Our simulation tool began as the core component (and reason for the name of) **CWhatUC**. It makes use of Fourier impulse-response and convolution techniques to create a first-order approximation of what the patient would actually see. When used in conjunction with surgical simulations, it has a strong potential to provide a patient with an estimate of his or her post-refractive surgical vision. As we showed, it could also be used to explore how glare and pupil size affect acuity.

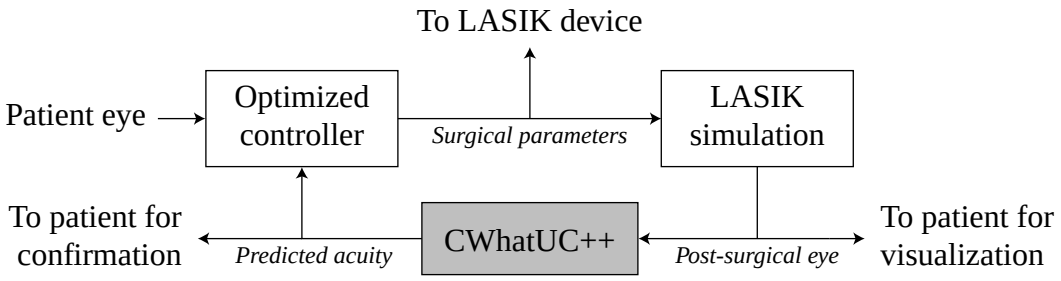

Figure 9.1: When customized LASIK procedures and accurate surgical simulations become commonplace, **CWhatUC++** could be used in a feedback loop to optimize for visual acuity. Patients would have the opportunity to see the predicted corneal shape and overall acuity before they decided to undergo the procedure.

9.4 Future Directions

To perform a perfectly correct visual acuity simulation would involve modeling the eye's structure and all layers of tissue and substance (cornea, aqueous humor, gradient index of refraction lens and vitreous humor) that the light must pass through to reach the retina [80]. In addition, one would have to model the physical effects of the eye: glare, scattering (causing halos and bloom) and the Stiles-Crawford effect [99]. These would be a function of the patient's age, capturing the optical and neural changes that occur. A next-generation system based on ideas from **CWhatUC** but which incorporates these effects we will call **CWhatUC++**.

Customized refractive surgery has the potential of being the "killer app" for **CWhatUC++**. Future LASIK procedures will allow very fine control, with hundreds of parameters available rather than simply ablation diameter and laser pulse count [36]. If a surgical simulation existed that accurately modeled the corneal response, **CWhatUC++** could be utilized in a feedback loop as shown in Figure 9.1 to optimize for the parameters that gave maximal visual acuity. "Guaranteed 20/10" vision, anyone?

9.5 Summary

In summary, this work attempted to provide tools to gain some insight into the acuity contributions of the cornea. There is a long way to go to fully understand and model the wonderfully rich and complex human visual system. It is hoped that other bioengineering collaborations among experts from the fields of computer graphics and vision science will continue to bear fruit.

Bibliography

[1] F. H. Adler. *Physiology of the Eye, 4th edition.* Mosby Company, St. Louis, MO, 1965.

[2] Pablo Artal, Javier Santamaría, and Julian Bescoós. Retrieval of wave aberration of human eyes from actual point-spread-function data. *J. Opt. Soc. Am. A*, 5:1201–1206, 1988.

[3] T. Y. Baker. Ray tracing through non-spherical surfaces. *Proc. Phys. Soc.*, 55:361, 1943.

[4] Brian A. Barsky, Stanley A. Klein, and Daniel D. Garcia. Gaussian power, mean sphere, and cylinder representations for corneal maps with applications to the diagnosis of keratoconus. *Invest. Ophthalmol. Vis. Sci*, 37:558, 1996.

[5] Brian A. Barsky, Stanley A. Klein, and Daniel D. Garcia. Gaussian power with cylinder vector field representation for corneal topography maps. *Optom. Vis. Sci*, 74(11):917–925, 1997.

[6] Brian A. Barsky, Robert B. Mandell, and Stanley A. Klein. Corneal shape illusion in keratoconus. *Invest. Ophthalmol. Vis. Sci*, 36(Suppl.):5308, 1995.

[7] John P. Beale Jr. *No More Glasses (Or Contact Lenses).* Doctors' Ophthalmic Press, San Francisco, CA, 1986.

[8] James M. Beck, Rida T. Farouki, and John K. Hinds. Surface analysis methods. *IEEE Computer Graphics and Applications*, 6(12):18–36, 1986.

[9] Michael W. Belin, David Litoff, Salvins J. Strods, Steven S. Winn, and Richard S. Smith. The par technology corneal topography system. *Refractive and Corneal Surgery*, 8:88–96, 1992.

[10] Peter D. Bergenske and Lynn E. Konkel. Training staff to measure visual acuity. *Optometric Economics*, pages 46–51, Fall 1996.

[11] Frans J. J. Blommaert, Henny G. M. Heynen, and Jacques A. J. Roufs. Point spread functions and detail detection. *Spatial Vision*, 2(2):99 – 115, 1987.

[12] Max Born and Emil Wolf. *Principles of optics, 7th Edition.* Cambridge University Press, Cambridge, UK, 1980.

[13] Douglas Brenner. Modeling the cornea with the topographic modeling system videokeratoscope. *Optom. Vis. Sci*, 74(11):895–898, 1997.

[14] britannica.com. *Encyclopædia Britannica Online : Optics : Lens Aberrations.* http://www.britannica.com /bcom/eb/article/5/0,5716,115155+29,00.html.

[15] Lucio Buratto. *Corneal Topography : The Clinical Atlas.* SLACK Incorporated, Thorofare, NJ, 1996.

[16] Jon J. Camp, Leo J. Maguire, Bruce M. Cameron, and Richard A. Robb. A computer model for the evaluation of the effect of corneal topography on optical performance. *Am. J. Ophthalmol.*, 109:379–386, 1990.

[17] Jon. J. Camp, Leo J. Maguire, and Richard A. Robb. An efficient ray tracing algorithm for modeling visual performance from corneal topography. In *First Conference on Visualization in Biomedical Computing*, pages 279–285, Atlanta, GA, May 22–25 1990. The Institute of Electrical and Electronics Engineers, Inc., IEEE Computer Society Press.

[18] Charles Campbell. Corneal aberrations, monocular diplopia, and ghost images: Analysis using corneal topographical data. *Optom. Vis. Sci*, 75(3):197–207, 1998.

[19] James Casey. *Exploring Curvature*. Vieweg, Germany, 1996.

[20] Jacob A. Corbin, Stanley A. Klein, and Corina van de Pol. Measuring effects of refractive surgery on corneas using taylor series polynomials. In *Proceedings of Ophthalmic Technologies IX*, San Jose, CA, January 23–29 1999. SPIE International Symposium on Biomedical Optics.

[21] A. M. de Beus and S. E. Brodie. Towards intrinsic representations of the corneal surface. *Invest. Ophthalmol. Vis. Sci*, 35(Suppl):2197, 1994.

[22] Paul E. Debevec and Jitendra Malik. Recovering high dynamic range radiance maps from photographs. In *Proceedings of ACM SIGGRAPH 1997*, pages 369–378, Los Angeles, CA, August 3–8 1997. SIGGRAPH, Association of Computer Machinery, Inc.

[23] Steven A. Dingeldein and Stephen D. Klyce et al. Quantitative descriptors of corneal shape derived from computer-assisted anaylsis of photokeratographs. *Refractive and Corneal Surgery*, 5(6):372–378, 1989.

[24] Manfred P. Docarmo. *Differential Geometry of Curves and Surfaces.* Prentice-Hall, Englewood Cliffs, NJ, 1976.

[25] J. Boyd Eskridge, John F. Amos, and Jimmy D. Bartlett. *Clinical Procedures in Optometry.* J. B. Lippincott Company, Philadelphia, PA, 1991.

[26] Richard P. Feynman, Robert B. Leighton, and Matthew Sands. *The Feynman Lectures on Physics, Volume I.* Addison-Wesley, Reading, MA, 1963.

[27] James D. Foley, Andries van Dam, Steven K. Feiner, and John F. Hughes. *Computer Graphics : Principles and Practice, 2nd Edition.* Addison-Wesley Publishing Co., Reading, MA, 1990.

[28] Grant R. Fowles. *Introduction to Modern Optics.* Dover Publications, Inc., New York, NY, 1989.

[29] Daniel D. Garcia, Brian A. Barksy, and Stanley A. Klein. Cwhatuc: A visual acuity simulator. In *Proceedings of Ophthalmic Technologies VIII, SPIE International Symposium on Biomedical Optics*, pages 290–298, San Jose, CA, January 24–30 1998. SPIE.

[30] Daniel D. Garcia, Corina van de Pol, Stanley A. Klein, and Brian A. Barsky. Wavefront coherence area for predicting visual acuity of post-prk and post-park refractive

surgery patients. In *Proceedings of Ophthalmic Technologies IX, SPIE International Symposium on Biomedical Optics*, San Jose, CA, January 23–29 1999. SPIE.

[31] Al Globus and Eric Raible. Fourteen ways to say nothing with scientific visualization. *IEEE Computer*, pages 86–88, July 1994.

[32] Michael J. Goggin, Paul Kenna, and Frank Lavery. Haze following photorefractive and photoastigmatic refractive keratectomy with the nidek ec5000 and the summit excimed uv200. *Journal of Cataract and Refractive Surgery*, 23(1):50–53, 1997.

[33] Michael J. Goggin and Paul Kenna et al. Photoastigmatic refractive keratectomy for compound myopic astigmatism with a nidek laser. *Journal of Refractive Surgery*, 13(2):162–166, 1997.

[34] Rafael C. Gonzalez and Richard E. Woods. *Digital Image Processing.* Addison-Wesley, Reading, MA, 1992.

[35] Joseph W. Goodman. *Introduction to Fourier Optics.* McGraw-Hill, Inc., San Francisco, CA, 1968.

[36] Christine Gorman. Should you get the laser eye fix? *Time Magazine*, 154(15):58–66, October 11 1999.

[37] J. E. Greivenkamp, J. Schweigerling, J. M. Miller, and M. D. Mellinger. Visual acuity modeling using optical raytracing of schematic eyes. *Am. J. Ophthalmol.*, 120:227–240, 1995.

[38] R. W. Gubisch. Optical performance of the human eye. *J. Opt. Soc. Am.*, 57(3):407–415, 1967.

[39] Hans Hagen, Stefanie Hahmann, Thomas Schreiber, Yasuo Nakajima, Bukard Wördenweber, and Petra Hollemann-Grundstedt. Surface interrogation algorithms. *Computer Graphics and Applications*, 12(5):53–60, 1992.

[40] David Halliday and Robert Resnick. *Physics, part two.* John Wiley and Sons, Inc., New York, NY, 1978.

[41] Mark A. Halstead, Brian A. Barsky, Stanley A. Klein, and Robert B. Mandell. A spline surface algorithm for reconstruction of corneal topography from a videokeratograph reflection pattern. *Optom. Vis. Sci*, 72:821–827, 1995.

[42] Mark A. Halstead, Brian A. Barsky, Stanley A. Klein, and Robert B. Mandell. Reconstructing curved surfaces from specular reflection patterns using spline surface fitting of normals. In *Proceedings of ACM SIGGRAPH 1996*, New Orleans, LA, August 4–9 1996. SIGGRAPH, Association of Computer Machinery, Inc.

[43] Mark Arthur Halstead. *Efficient Techniques for Surface Design Using Constrained Optimization.* PhD thesis, Department of Computer Science, University of California at Berkeley, Berkeley, CA, May 1996.

[44] Eugene Hecht. *Optics, Second Edition.* Addison-Wesley Publishing Co., 1990.

[45] Richard P. Hemenger, Alan Tomlinson, and Katherine Oliver. Corneal optics from videokeratographs. *Ophthal. Physiol. Opt.*, 15(1):63–68, 1995.

[46] P. S. Hersh and R. D. Stulting et al. Results of phase iii excimer laser photorefractive keratectomy for myopia. *Ophthalmology*, 104(10):1535–1553, 1997.

[47] H. Hopkins. *Wave theory of aberrations.* Oxford Univ. Press, 1950.

[48] Bradford Howland and Howard C. Howland. Subjective measurement of high-order aberrations of the eye. *Science*, 193:580–582, 1976.

[49] Howard C. Howland, Jan Buettner, and Raymond A. Applegate. Computation of the shapes of normal corneas and their monochromatic aberrations from videokeratometric measurements. In *Vision Science and Its Applications. 1994 Technical Digest Series. Volume 2*, volume 2, pages 54–57. Optical Society of America, Washington, DC, 1994.

[50] Howard C. Howland and Bradford Howland. A subjective method for the measurement of monochromatic aberrations of the eye. *J. Opt. Soc. Am.*, 67(11):1508–1518, 1977.

[51] Howard C. Howland, Richard H. Rand, and Sharon R. Lubkin. A thin-shell model of the cornea and its application to corneal surgery. *Refract. Corneal Surg.*, 8:183–186, 1992.

[52] J. K. Ijspeert, T. J. T. P. Van Den Berg, and H. Spekreijse. An improved mathematical description of the foveal visual point spread function with parameters for age, pupil size and pigmentation. *Vision Res.*, 33(1):15–20, 1993.

[53] Internet Media Services. *The Vision Correction Website : Laser Eye Surgery : rk / prk / lasik.* http://www.lasersite.com/.

[54] Victoria Interrante. Illustrating surface shape in volume data via principal direction-driven 3d line integral convolution. In *Proceedings of ACM SIGGRAPH 1997*, pages 109–116, Los Angeles, CA, August 3–8 1997. SIGGRAPH, Association of Computer Machinery, Inc.

[55] Michael P. Keating. *Geometric, Physical and Visual Optics.* Butterworths-Heinemann, Stoneham, MA, 1988.

[56] Peter R. Keller and Paul P. van Saarloos. Perspectives on corneal topography: a review of videokeratoscopy. *Clin. Exp. Optom*, 80(1):18–30, 1997.

[57] Miles V. Klein. *Optics.* John Wiley & Sons, New York, NY, 1970.

[58] Stanley A. Klein. Axial curvature and the skew ray error in corneal topography. *Optom. Vis. Sci*, 74:931–944, 1997.

[59] Stanley A. Klein. Corneal topography reconstruction algorithm that avoids the skew ray ambiguity and the skew ray error. *Optom. Vis. Sci*, 74:945–962, 1997.

[60] Stanley A. Klein. Optimal corneal ablation for eyes with arbitrary hartmann-shack aberrations. *J. Opt. Soc. Am. A*, 15(9):2580–2588, 1998.

[61] Stanley A. Klein and Daniel D. Garcia. Alternative representations of aberrations of the eye. In *Presented at Vision Science and Its Applications Meeting*, Santa Fe, NM, Februrary 11–14 2000.

[62] Stanley A. Klein and Robert B. Mandell. Shape and refractive powers in corneal topography. *Invest. Ophthalmol. Vis. Sci.*, 36:2096–2109, 1995.

[63] Stanley A. Klein, Robert B. Mandell, and Brian A. Barsky. Representing corneal shape. In *Vision Science and Its Applications*, volume 1, pages 37–40, Washington, DC, 1995. Technical Digest Series, Optical Society of America.

[64] Stephen D. Klyce. Computer-assisted corneal topography, high resolution graphic presentation and analysis of keratoscopy. *Ophthalmol. Vis Sci.*, 25:1426–1435, 1984.

[65] Douglas D. Koch, G. N. Foulks, and T. Moran. The corneal eyesys system: accuracy, analysis and reproducibility of first generation prototype. *Refract. Corneal Surg.*, 5:424–429, 1989.

[66] Craig Kolb, Don Mitchell, and Pat Hanrahan. A realistic camera model for computer graphics. In *Proceedings of ACM SIGGRAPH 1995*, pages 317–324, Los Angeles, CA, August 6–11 1995. SIGGRAPH, Association of Computer Machinery, Inc.

[67] M. Koomen, R. Tousey, and R. Scolnick. The spherical aberration of the eye. *J. Opt. Soc. Am.*, 39(5):370–376, 1949.

[68] J. H. Krachmer, R. S. Feder, and M. W. Belin. Keratoconus and related noninflammatory corneal thinning disorders. *Surv. Ophthalmol.*, 28(4):293–322, 1984.

[69] Roger Kumpf. Multivariate corneal visualization in the eyeview system. Master's thesis, Department of Computer Science, University of California at Berkeley, Berkeley, CA, May 1995.

[70] J. E. A. Landgrave and Jesús R. Moya-Cessa. Generalized coddington equations in ophthalmic lens design. *J. Opt. Soc. Amer.*, 12(8):1637–1644, 1996.

[71] Junzhong Liang. *A New Method to Precisely Measure the Wave Aberrations of the Human Eye with a Hartmann-Shack Wavefront Sensor*. PhD thesis, Department of Mathematics, Universität Heidelberg, Heidelberg, Germany, December 1991.

[72] Norberto López-Gil and Howard C. Howland. Measurement of the eye's near infrared wave-front aberration using the objective crossed-cylinder aberroscope technique. *Vision Research*, 39:2031–2037, 1999.

[73] H. Lubatschowski and O. Kermani et al. A scanning and rotating slit arf excimer laser delivery system for refractive surgery. *Journal of Refractive Surgery*, 14(2 Suppl):s186–191, 1998.

[74] Klaus Ludwig, Peter Schäeffer, Herbert Gross, Theo Lasser, and Anselm Kampik. Mathematical simulation of retinal image contrast after photorefractive keratectomy with a diaphragm mask. *Journal of Refractive Surgery*, 12:248–253, 1996.

[75] Leo. J. Maguire and W. D. Bourne. Corneal topography of early keratoconus. *Am. J. Ophthalmol.*, 108:107–112, 1989.

[76] Leo J. Maguire, Jon J. Camp, and Richard A. Robb. Informing interested parties of changes in the optical performance of the cornea caused by keratorefractive surgery — a ray tracing model that tailors presentation of results to fit the lefel of sophistication of the audience. In *SPIE Vol. 1808 Visualization in Biomedical Computing 1992*, pages 601 – 609, Chapel Hill, NC, October 13 – 16 1992. SPIE — The International Society for Optical Engineering, SPIE.

[77] Leo J. Maguire, Ralph W. Zabel, Paula Parker, and Richard L. Lindstrom. To-

pography and raytracing analysis of patients with excellent visual acuity 3 months after excimer laser photorefractive keratectomy for myopia. *Refract. Corneal Surg.*, 8:122–128, March/April 1991.

[78] Virendra N. Mahajan. *Optical Imaging and Aberrations.* SPIE Optical Engineering Press, Bellingham, WA, 1998.

[79] Richard J. Mammone, Martin Gersten, Dennis J. Gormley, Richard S. Koplin, and Virginia L. Lubkin. 3-d corneal modeling system. *IEEE Trans. Biomedical Eng.*, 37:66–73, 1990.

[80] Robert B. Mandell. *Contact Lens Practice, 4th Edition.* Charles C. Thomas, Springfield, IL, 1988.

[81] Robert B. Mandell. The enigma of the corneal contour. *the CLAO Journal*, 18(4):267–273, 1992.

[82] Robert B. Mandell, Stanley A. Klein, C. H. Shie, Brian A. Barsky, and Zijiang Yang. Axial and instantaneous radii in videokeratography. *Invest. Ophthalmol. Vis. Sci*, 35(Suppl):2079, 1994.

[83] Marguerite McDonald. Corneal topography: A vital tool for refractive surgery. *Eyecare Technology*, pages 21–22, 24, 65, June 1996.

[84] M. Minnaert. *The nature of light & color in the open air.* Dover Publications, Inc., New York, NY, 1954.

[85] Parry Moon and Domina Eberle Spencer. On the stiles-crawford effect. *J. Opt. Soc. Am.*, 34(6):319–329, 1944.

[86] Hans C. Ohanian. *Physics, vol. 1.* W. W. Norton and Co., New York, NY, 1985.

[87] Donald C. O'Shea. *Elements of Modern Optical Design.* John Wiley & Sons, New York, NY, 1985.

[88] Sudi Patel, John Marshall, and Frederick W. Fitzke. Model for predicting the optical performance of the eye in refractive surgery. *Refract Corneal Surg*, 9:366–375, September / October 1993.

[89] B. Platt and R. V. Shack. Lenticular hartmann-screen. Newsletter 5, 15, Optical Science Center, University of Arizona, 1971.

[90] Ronald B. Rabbetts. *Clinical Visual Optics, third edition.* Butterworth Heinemann Ltd., Oxford, UK, 1998.

[91] Jeff Rabin and James Wicks. Measuring resolution in the contrast domain: the small letter contrast test. *Optom. Vis. Sci*, 73(6):398–403, 1996.

[92] R. H. Rand, S. R. Lubkin, and H. C. Howland. Analytical model of corneal surgery. *Journal of Biomechanical Engineering*, 113:239–241, May 1991.

[93] Cynthia Roberts. The accuracy of power maps to display curvature data in corneal topography systems. *Invest. Ophthalmol. Vis. Sci*, 35:3525–3532, 1994.

[94] Jyrki Rovamo, Juvi Mustonen, and Risto Näsänen. Two simple psychophysical meth-

ods for determining the optical modulation transfer function of the human eye. *Vision Res.*, 34(19):2493–2502, 1994.

[95] Thomas O. Salmon and Douglas G. Horner. Comparison of elevation, curvature, and power descriptors for corneal topographic mapping. *Optom. Vis. Sci*, 72(11):800–808, 1995.

[96] Jim Schwiegerling and John E. Greivenkamp. Using corneal height maps and polynomial decomposition to determine corneal aberrations. *Optom. Vis. Sci*, 74(11):906–916, 1997.

[97] Jim Schwiegerling, John E. Greivenkamp, Joseph M. Miller, Robert W. Snyder, and Millicent L. Palmer. Optical modeling of radial keratotomy incision patterns. *American Journal of Ophthalmology*, 122(6):808–817, December 1996.

[98] T. Seiler, W. Reckmann, , and R. K. Maloney. Effective spherical aberration of the cornea as a quantitative descriptor in corneal topography. *Journal of Cataract and Refractive Surgery*, 19(Supplement):155–165, 1993.

[99] Greg Spencer, Peter Shirley, Kurt Zimmerman, and Donald P. Greenberg. Physically-based glare effects for digital images. In *Proceedings of ACM SIGGRAPH 1995*, pages 325–334, Los Angeles, CA, August 6–11 1995. SIGGRAPH, Association of Computer Machinery, Inc.

[100] Orestes N. Stavroudis. Simpler derivation of the formulas for generalized ray tracing. *J. Opt. Soc. Amer.*, 66(12):1330–1333, 1976.

[101] George B. Thomas Jr. and Ross L. Finney. *Calculus and Analytical Geometry.* Addison-Wesley, Reading, MA, 1980.

[102] S. L. Trokel, R. Rrinivasan, and B. Braren. Excimer laser surgery of the cornea. *Am. J. Ophthalmol.*, 96:710–715, 1983.

[103] Edward R. Tufte. *The Visual Display of Quantitative Information.* Graphics Press, Cherhire, CT, 1983.

[104] Edward R. Tufte. *Envisioning Information.* Graphics Press, Cherhire, CT, 1991.

[105] Edward R. Tufte. *Visual Explanations : Images and Quantities, Evidence and Narrative.* Graphics Press, Cherhire, CT, 1997.

[106] Rasik B. Vajpayee, Catherine A. McCarty, Geoffrey F. Aldred, Hugh R. Taylor, and The Excimer Laser Group. Undercorrection after excimer laser refractive surgery. *American Journal of Ophthalmology*, 122(6):801–807, 1996.

[107] Corina van de Pol. *Corneal Shape and Visual Performance after Keratorefractive Surgery.* PhD thesis, Department of Vision Science, University of California at Berkeley, Berkeley, CA, Fall 1999.

[108] Corina van de Pol, Henry H. Tran, Daniel D. Garcia, and Stanley A. Klein. Three-dimensional analysis of corneal image forming properties: A monocular diplopia example. In *Presented at Vision Science and Its Applications Meeting*, Santa Fe, NM, Februrary 6–9 1998.

[109] A. van Meeteren. Calculations on the optical modulation transfer function of the human eye. *Opt. Acta*, 21:395–412, 1974.

[110] Paul P. van Saarloos and Peter R. Keller. Comparing methods to view corneal topography data. *Clin. Exp. Optom*, 79(3):106–111, 1996.

[111] Wayne Verdon, Mark Bullimore, and Robert K. Maloney. Visual performance after photorefractive keratectomy. *Arch. Ophthalmol.*, 114:1465–1472, 1996.

[112] F. M. Vos and H. J. W. Spoelder. Visualization in corneal topography. In *Proceedings of IEEE Visualization*, Research Triangle Park, NC, October 18–23 1998. IEEE, IEEE Computer Society.

[113] G. Walsh, W. N. Charman, and Howard C. Howland. Objective technique for the determination of monochromatic aberrations of the human eye. *J. Opt. Soc. Amer.*, 1(9):987–992, 1984.

[114] Jianyi Wang, David A. Rice, and Stephen D. Klyce. A new reconstruction algorithm for improvement of corneal topographical analysis. *Refract. Corneal Surg.*, 5:379–387, 1989.

[115] W. T. Welford. *Aberrations of Optical Systems.* Adam Hilger, Ltd., Bristol, England, 1986.

[116] Gerald Westheimer and Fergus W. Campbell. Light distribution in the image formed by the living human eye. *J. Opt. Soc. Am.*, 52(9):1040–1045, 1962.

[117] Charles S. Williams and Orville A. Becklund. *Introduction to the Optical Transfer Function.* John Wiley & Sons, New York, NY, 1989.

[118] Steven E. Wilson and Stephen D. Klyce. Advances in the analysis of corneal topography. *Surv. Ophthalmol.*, 35:269–277, 1991.

[119] Steven E. Wilson and Stephen D. Klyce. Quantitative descriptors of corneal topography. a clinical study. *Arch. Ophthalmol.*, 109(3):349–353, 1991.

[120] Patrick Henry Winston. *Artificial Intelligence.* Addison-Wesley, Reading, MA, 1984.

[121] Robert S. Wolff and Larry Yaeger. *Visualization of Natural Phenomena.* The Electronic Library of Science, Santa Clara, CA, 1993.